

©2015

Matthew J. Niznik

ALL RIGHTS RESERVED

SYNOPTIC TIMESCALE VARIABILITY AND TROPICAL-EXTRATROPICAL  
INTERACTION ALONG THE SOUTH PACIFIC CONVERGENCE ZONE IN  
CLIMATE MODEL SIMULATIONS

By

MATTHEW J. NIZNIK

A dissertation submitted to the  
Graduate School-New Brunswick  
Rutgers, The State University of New Jersey

In partial fulfillment of the requirements

For the degree of

Doctor of Philosophy

Graduate Program in Atmospheric Science

Written under the direction of

Benjamin R. Lintner

And approved by

---

---

---

---

New Brunswick, New Jersey

May 2015

## ABSTRACT OF THE DISSERTATION

### Synoptic Timescale Variability and Tropical-Extratropical Interaction along the South Pacific Convergence Zone in Climate Model Simulations

By MATTHEW J. NIZNIK

Dissertation Director:

Benjamin R. Lintner

The South Pacific Convergence Zone (SPCZ) is simulated as too zonal a feature in current generation climate models, including those in Phase 5 of the Coupled Model Intercomparison Project (CMIP5). On synoptic timescales, the SPCZ structure is controlled both by the amount of low-level inflow from the relatively dry southeastern Pacific as well as the tropical-extratropical interaction between transient synoptic systems and the mean background state. However, the fidelity with which CMIP5 models are capable of simulating these interactions has not been previously examined. Building on the analysis of observed SPCZ-region synoptic scale variability by Lintner and Neelin (2008), composite analysis of two reanalyses and 17 CMIP5 models reveals both individual models and their ensemble mean capture patterns of wind, specific humidity, and precipitation anomalies consistent with reanalysis and observational results. To further explore the difference between weak- and strong-inflow conditions, both are instantaneously imposed in an ensemble of experiments using the Quasi-equilibrium Tropical Circulation Model 2 (QTCM2). While imposed circulation anomalies lead to observed moisture and precipitation anomalies, imposed moisture anomalies manifest a

weak circulation anomaly. Thus, it appears more likely that the initiation of SPCZ shifts is dynamic in nature.

Analysis of synoptic variability in the simulated subtropical SPCZ reveals that the basic mechanism of tropical-extratropical interaction is generally well simulated, with storms approaching the SPCZ along comparable trajectories to observations. However, there is a broad spread in mean precipitation and its variability across the CMIP5 ensemble. The region of mean negative zonal stretching deformation or “storm graveyard” in the upper troposphere is displaced in CMIP5 models to the northeast of its position in reanalysis data, albeit with pronounced ( $\approx 25^\circ$ ) inter-model longitudinal spread; SPCZ precipitation is similarly displaced and models with stronger storm graveyards show higher precipitation variability. Overall, these results further confirm that SPCZ errors are primarily related to a biased background state. Additionally, SPCZs simulated by CMIP5 models are not simply too zonal; rather, in models the subtropical SPCZ manifests a diagonal tilt similar to observations while SST biases force an overly zonal tropical SPCZ, resulting in a more discontinuous SPCZ than observed.



## **Acknowledgements**

I have chosen to list my acknowledgements in (semi-) chronological order because any attempt to list names based on some contrived value of each's contribution to this work is a fool's errand; everyone listed in this section has left an indelible mark on both my work and myself. Thus, I would first like to thank my parents, Joseph and Patricia, for their love and encouragement and for placing a high value on my education throughout my life. I also would like to thank my brother, Josh, as well as Sean Kinney, Jerry Mrozinski, and Nick Attanasio for being great friends and giving me welcome breaks from my work.

Moving on to my career training, I would first like to thank Dr. Brian Mapes for being my undergraduate research advisor and exciting my interest in scientific research. Perhaps most obviously, I thank Dr. Benjamin Lintner, my advisor. He made the choice to pursue graduate study at Rutgers University relatively simple; in addition to introducing a research topic that I will continue to explore beyond this dissertation, he allowed me the freedom to explore other tangential topics and incorporate those ideas into my work. His mentorship, advice, and support during the last four and a half years have helped me immensely. I also thank the other members of my committee: Dr. Anthony Broccoli, Dr. James Miller, Dr. Adrian Matthews, and Dr. Matthew Widlansky. Tony referred me to Ben when I first visited Rutgers as a prospective graduate student and has given me excellent feedback and career advice. Jim has served as an advisor to a tangential study and has always been friendly, helpful, and encouraging. Both Adrian and Matthew have served as excellent collaborators since I first met them in New Caledonia in 2012 and their previous work has served as both an inspiration and the foundation for

many of my analyses. While not a member of my committee, Dr. Bryan Raney has been a great mentor and friend since his arrival at Rutgers two years ago and has always been available for help with coding and computers. Additionally, I'd like to thank the administrative staff in the Environmental Sciences Department for their assistance throughout my time at Rutgers.

I've also met many students at Rutgers who deserve acknowledgement as well; all were and remain some of my best friends and helped me keep my work and social lives in proper balance. Brian Marmo began graduate study at the same time as me and served as a great officemate throughout our time together. Dr. Anthony DeAngelis deserves a lot of credit for pushing me to work hard, explain my research clearly, and helping me to laugh and not take things *too* seriously. He was also invaluable in helping to process all of the CMIP5 data used in this dissertation. Dr. Michael Erb was always available when I needed someone to bounce ideas off of and he, along with his fictional protagonist Kelvin McCloud, serve as a reminder of the "magic" of scientific curiosity. Dr. Stephen Nicholls was a great resource when I had general questions in meteorology and numerical modeling. Other students I'd like to acknowledge here are (in alphabetical order): Dr. Ross Alter, Allison Collow, Dr. Thomas Collow, Max Pike, and Dr. Jessica Sagona.

Finally, I'd like to acknowledge and sincerely thank my fiancée, Kathleen Warrell, for all of her love, laughs, patience, and encouragement throughout my final year of study. I certainly hope I can match her level of support as she finishes her Ph.D. work in the coming years.

Financial support for this work was provided by New Jersey Agricultural Experiment Station Hatch grant NJ07102 and National Science Foundation grant NSF-

AGS-1312865. Parts of this thesis (mainly Chapter 2) have been published in the Journal of Climate, in the article “Circulation, Moisture, and Precipitation Relationships along the South Pacific Convergence Zone in Reanalyses and CMIP5 Models” by Matthew J. Niznik and Benjamin R. Lintner. Additionally, parts of this thesis (mainly Chapter 3) have been accepted for publication in the Journal of Climate, in the article “The Role of Tropical-Extratropical Interaction and Synoptic Variability in Maintaining the South Pacific Convergence Zone in CMIP5 Models” by Matthew J. Niznik, Benjamin R. Lintner, Adrian J. Matthews, and Matthew J. Widlansky. The American Meteorological Society holds copyright to both works.

## Table of Contents

ABSTRACT OF THE DISSERTATION .....	ii
Acknowledgements .....	iv
Table of Contents .....	vii
List of Tables .....	ix
List of Illustrations .....	xi
1. Introduction .....	1
1.1 The South Pacific Convergence Zone: Introduction and Societal Relevance .....	1
1.2 Low- and High-Frequency SPCZ Variability .....	2
1.3 The SPCZ in Climate Models .....	7
1.4 Motivation for Further Work .....	10
2. SPCZ Response to Varying Low-Level Inflow .....	11
2.1 Introduction .....	11
2.2 Data and methodology .....	11
2.3 Low-level inflow composites .....	17
2.3.a Reanalyses .....	17
2.3.b CMIP5 models .....	18
2.3.c Vertical structure .....	19
2.4 Lead-lag composites .....	20
2.4.a Reanalysis .....	20
2.4.b CMIP5 models .....	23
2.4.c Vertical structure .....	24
2.5 Summary .....	25

3. Extratropical-Tropical Interactions and Synoptic Variability in the SPCZ .....	26
3.1 Introduction.....	26
3.2 Data and methodology .....	26
3.3 Precipitation variability in the SPCZ .....	32
3.3.a Model precipitation biases .....	32
3.3.b Power spectra analyses .....	36
3.4 Storm graveyard statistics .....	38
3.5 Composite analysis of synoptic disturbances interacting with the SPCZ.....	40
3.6 Summary .....	44
4. Forcing low-level inflow shifts east of the SPCZ.....	45
4.1 Introduction.....	45
4.2 Data and methodology .....	45
4.3 QTCM2 biases .....	49
4.4 Barotropic vorticity experiments .....	52
4.5 Barotropic moisture experiments.....	58
4.6 Summary .....	59
5. Summary, conclusions, and future research directions.....	61
5.1 SPCZ response to varying low-level inflow .....	61
5.2 Synoptic variability along the SPCZ in CMIP5 models .....	64
5.3 Forcing low-level inflow shifts east of the SPCZ.....	68
Tables.....	71
Figures.....	77
References.....	128

## List of Tables

**Table 2.1.** CMIP5 models used in Chapter 2 of this dissertation. All models had daily data available from CMIP5 historical experiment runs and are used in the contemporary period (1960-1999) analysis. Those models marked with 0 are not used in the future period (2060-2100) analysis; those unmarked are members of the model subset. Except for FGOALS-g2 and CCSM4 (for which the third and sixth ensemble members, respectively, were used due to availability), the first ensemble member of the historical and RCP8.5 experiment was chosen. All models were regridded to 2.5° in both latitude and longitude using area averaging (if in subset) or linear interpolation (if not in subset) for purposes of comparison and the calculation of an model ensemble mean. (Note: MIROC4h lacked RCP8.5 model output and was excluded from the subset despite being regridded using area averaging.) Longitude and latitude columns (Lon. And Lat., respectively) list the resolution of the model output available from PCMDI's CMIP5 database. Further information can be found at [http://cmip-pcmdi.llnl.gov/cmip5/docs/CMIP5\\_modeling\\_groups.pdf](http://cmip-pcmdi.llnl.gov/cmip5/docs/CMIP5_modeling_groups.pdf) ..... 72

**Table 3.1.** CMIP5 models used in Chapter 3. Longitude and latitude columns (Lon. And Lat., respectively) list the resolution of the model output available from PCMDI's CMIP5 database. Further information can be found at [http://cmip-pcmdi.llnl.gov/cmip5/docs/CMIP5\\_modeling\\_groups.pdf](http://cmip-pcmdi.llnl.gov/cmip5/docs/CMIP5_modeling_groups.pdf) (Note: HadGEM2-CC is called HadGEM2-A in the AMIP output. For consistency, we will refer to the model as HadGEM2-CC for both the historical and AMIP experiments.) ..... 73

**Table 3.2.** DJF climatological precipitation ( $\text{mm day}^{-1}$ ) over the subtropical SPCZ region ( $135^{\circ}\text{W}$ – $165^{\circ}\text{W}$ ,  $20^{\circ}\text{S}$ – $35^{\circ}\text{S}$ ). Models with mean precipitation greater than 1 standard deviation from the median of models are shown in bold..... 74

**Table 3.3.** Grouping of models based on two criteria for proper simulation of precipitation variability using both the full precipitation record as well as a reconstructed synoptic precipitation signal. a) The ratio of model precipitation standard deviation ( $\sigma$ ) to TRMM precipitation standard deviation in the subtropical SPCZ ( $135^{\circ}\text{W}$ – $165^{\circ}\text{W}$ ,  $20^{\circ}\text{S}$ – $35^{\circ}\text{S}$ ). Ratios that exceed the threshold value of 0.8 are shown in bold. b) The principal component of the first principal uncertainty pattern (PUP) for model precipitation standard deviation. Negative PUP values are shown in bold. (c) Models that meet all criteria ( $\sigma$  ratios  $> 0.8$  and  $\text{PC} < 0$ ) belong to the high-variability group (HVG); models that meet none belong to the low-variability group (LVG); the remaining models belong to the intermediate-variability group (IVG). Meeting any individual criterion for inclusion in the HVG group denoted by boldface. .... 75

**Table 4.1.** List of experiments performed. Similar groups of experiments are grouped together, using a “y” to denote the part of the name that changes among members of that group. Unless individual values are noted for different y’s, all experiments in the same group maintain the same value for all experiments (e.g. everything except anomaly magnitude is the same in the Wy group of experiments)..... 76

## List of Illustrations

<b>Figure 1.1.</b> Climatological DJF precipitation (shading, mm day <sup>-1</sup> ) over the Pacific for the CPC Merged Analysis of Precipitation (CMAP), with the Tropical Rainfall Measuring Mission (TRMM) 4 mm day <sup>-1</sup> contour (in black) included for reference.....	77
<b>Figure 2.1.</b> January precipitation climatology in the SPCZ region, 1998-2010, for three products: a) TRMM 3B42 precipitation estimates (shading) and 4 mm/day contour (in white), b) R1 precipitation 4 mm/day contour (in grey), c) CFSR precipitation 4 mm/day contour (in pink). .....	78
<b>Figure 2.2.</b> Composite analysis applied to January daily averages. (a) Composite differences (weak-inflow minus strong-inflow) of R1 (left) and CFSR (right) 850 hPa winds (vectors, in m/s) and specific humidity (shading, in g/kg) for a composite index of zonal wind at 850 hPa averaged over 140°W-120°W and 20°S-10°S. Significance for wind and moisture (at the 99 <sup>th</sup> percentile) is denoted by black vector color and dark grey striping, respectively. Included for reference is the January SPCZ climatology (green contour, 4 mm/day) as well as the region in which the composite index was calculated (black box). (b) Composite difference of R1 (left) and CFSR (right) precipitation (shading, in mm/day) and the weak-inflow and strong-inflow phase 4 mm/day contours (green and brown lines, respectively). Significance for precipitation (at the 99 <sup>th</sup> percentile) is denoted by dark grey striping. Included for reference is the region in which the composite index was calculated (black box).....	79
<b>Figure 2.3.</b> Same as Figure 2.2, but during the period 1998-2010 and replacing CFSR precipitation with TRMM 3B42 precipitation estimates. ....	80



**Figure 2.4.** Composite analysis applied to model output from the CMIP5 historical experiment. Shown are composite differences (weak-inflow minus strong-inflow) of 850 hPa zonal and meridional wind (vectors, in m/s) and 850 hPa specific humidity (shading, in g/kg) for a composite index of zonal wind at 850 hPa averaged over 140°W-120°W and 20°S-10°S. Data appears only if it is significant at the 99<sup>th</sup> percentile except for the model ensemble mean, which considers a value at a particular spatial point significant if a majority of the models (nine) agree on significance there. Included for reference are the January SPCZ climatology (green contour, 4 mm/day) as well as the region in which the composite index was calculated (black box). ..... 81

**Figure 2.5.** Composite analysis applied to model output from the CMIP5 historical experiment. Shown are composite differences (weak-inflow minus strong-inflow) of precipitation (shading, in mm/day) for a composite index of zonal wind at 850 hPa averaged over 140°W-120°W and 20°S-10°S. Significance for precipitation (at the 99<sup>th</sup> percentile) is denoted by dark grey striping. Included for reference are the 4 mm/day precipitation contours for the weak-inflow phase (in green) and strong-inflow phase (in brown) as well as the region in which the composite index was calculated (black box). 83

**Figure 2.6.** Results of the composite analysis at 850 hPa shown at multiple vertical levels. CFSR (d) is the same as Figure 2.2a for CFSR. MEM (d) is the same result as Figure 2.4, though now the significance conventions of Figure 2.2 are used (i.e. non-significant wind and moisture anomalies are still plotted). (a), (b), and (c) show results at 250 hPa, 500 hPa, and 700 hPa, respectively, with significance associated with each plots' respective level (i.e. moisture in CFSR (c) is significant if it exceeds the 99<sup>th</sup> percentile of random composites generated at 700 hPa, etc.). Also included for reference

is the mean 4 mm/day precipitation contour (in green) as well as the region in which the composite index was calculated (black box). ..... 84

**Figure 2.7.** Lead-lag composite differences using CFSR data. Each panel shows the difference in wind (vectors, in m/s) and specific humidity (shading, in g/kg) between the weak-inflow/strong-inflow phase composite at a given number of days before or after a maximum or minimum (i.e. -2, the top row, shows composites 2 days before a maximum or minimum) and the mean 27 December – 4 February (40 day period) state. Significance for wind and moisture (at the 99<sup>th</sup> percentile) is denoted by black vector color and dark grey striping, respectively. Also included for reference are the composite 4 mm/day precipitation contour (weak-inflow phase, in green; strong-inflow phase, in brown), the mean 27 December – 4 February (40 day period) 4 mm/day precipitation contour (in light yellow), and the region in which the composite index was calculated (black box). ..... 85

**Figure 2.8.** Lead-lag composites using CFSR (left) and CMIP5 MEM (right) data. For CFSR, sea level pressure anomalies from the January mean are plotted every 1 hPa (positive values solid, negative dashed) for the weak-inflow phase (in red) and strong-inflow phase (in blue). Similar for MEM, but using a smaller contour interval of 0.5 hPa. 0 hPa line is omitted. Included for reference is the region in which the composite index was calculated (black box). ..... 86

**Figure 2.9.** Composites of 250 hPa wind (shading and vectors, m/s) averaged between day -5 and day -3 of the weak-inflow (top) and strong-inflow (middle) phases as well as their difference (weak-inflow – strong-inflow, bottom). Significance for wind (at the 99<sup>th</sup> percentile) is denoted by black vector color and dark grey striping. .... 87

**Figure 2.10.** Same as Figure 2.7, but using MEM data. .... 88

**Figure 2.11.** Lead-lag composites using CFSR (left) and CMIP5 MEM (right data. For CFSR, specific humidity anomalies at 850 hPa (in red) and 500 hPa (in blue) are plotted every  $0.5 \text{ g kg}^{-1}$  (positive values solid, negative dashed) for weak-inflow phase minus strong-inflow phase. Similar for MEM, but using a smaller contour interval of  $0.25 \text{ g kg}^{-1}$ .  $0 \text{ g kg}^{-1}$  line is omitted. .... 89

**Figure 3.1.** Climatological DJF precipitation (shading,  $\text{mm day}^{-1}$ ) over the Pacific for the (a) TRMM estimated data set, (b) Climate Forecast System Reanalysis (CFSR), (c) Coupled Model Intercomparison Project Phase 5 (CMIP5) coupled model ensemble mean (MEM), (d)-(o) individual CMIP5 coupled model means. The thick black line in all panels is the TRMM  $4 \text{ mm day}^{-1}$  contour, for reference..... 90

**Figure 3.2.** As Figure 3.1, but for the (c) model ensemble mean, and (d)-(o) individual means of the atmosphere-only models..... 91

**Figure 3.3.** Climatological DJF precipitation standard deviation (shading,  $\text{mm day}^{-1}$ ) over the Pacific for the (a) TRMM estimated data set, (b) CFSR, (c) CMIP5 atmosphere-only model ensemble mean (MEM), (d)-(o) individual CMIP5 atmosphere-only model means. The thick black line in all panels is the TRMM  $4 \text{ mm day}^{-1}$  climatological precipitation contour, for reference..... 92

**Figure 3.4.** As Figure 3.3, but for standard deviation of 14-day high-pass filtered precipitation. .... 93

**Figure 3.5.** Normalized, logarithmic DJF precipitation histograms in the region  $165^{\circ}\text{W}$ – $135^{\circ}\text{W}$ ,  $20^{\circ}\text{S}$ – $35^{\circ}\text{S}$  from (a) coupled and (b) atmosphere-only models as well as their differences. The first bin measures  $0$ – $0.5 \text{ mm day}^{-1}$  counts, followed by  $0.5$ – $2.5 \text{ mm day}^{-1}$ , with each subsequent bin having size  $2.5 \text{ mm day}^{-1}$  (e.g.  $2.5$ – $5.0 \text{ mm day}^{-1}$ ). The final

bin measures precipitation values exceeding  $100 \text{ mm day}^{-1}$ . (a) TRMM (green boxes) and coupled models (lines); error (see Section 3.2 for details) shown in the legend for each model. (b) TRMM (green boxes) and atmosphere-only models (lines); error from TRMM shown in the legend for each model. (c) Difference between atmosphere-only and coupled model histograms for each model (lines); difference and increase/decrease in error, respectively, between atmosphere-only and coupled histograms shown in the legend for each model. .... 94

**Figure 3.6.** Normalized power spectra in coupled (top row) and atmosphere-only (bottom row) models. For OLR spectra (left column), models are compared to CFSR and a NOAA OLR observational dataset. For precipitation spectra (right column), models are compared to CFSR and TRMM precipitation estimates. Solid/dashed line indicates variability above/below the significance threshold (explained in Section 3.2). .... 96

**Figure 3.7.** Meridional average ( $20^{\circ}\text{S}$ – $35^{\circ}\text{S}$ ) of zonal stretching deformation (ZSD) in CFSR and models across the South Pacific ( $120^{\circ}\text{E}$ – $60^{\circ}\text{W}$ ), for (a) coupled, (b) atmosphere-only, and (c) difference between atmosphere-only and coupled models. MEM denotes the model ensemble mean in each panel. .... 97

**Figure 3.8.** Coupled model negative zonal stretching deformation (ZSD) at 250 hPa (blue shading,  $\text{s}^{-1}$ ) as compared to CFSR negative ZSD (black contours) at the same level in the storm graveyard region, as well as the coupled model ensemble mean (MEM). The location of the CFSR (black dot) and individual model or MEM (purple dot) ZSD minimum are shown for reference. The relative strength of the minimum value of ZSD in each model compared to CFSR is shown in parentheses after each model name. .... 98

**Figure 3.9.** As Figure 3.8, but using data from the atmosphere-only models and their MEM. The locations of the individual model or MEM ZSD minima are now denoted by a green dot..... 99

**Figure 3.10.** Composite analysis using 250 hPa vorticity in the region 140°W–127.5°W, 27.5°S–30°S CFSR (left column), atmosphere-only MEM (middle column), and coupled MEM (right column). Each row denotes the days before/after the low vorticity event (i.e. -2 is 2 days before, etc.). Shown in each panel are precipitation anomalies (shading, mm day<sup>-1</sup>), negative vorticity anomalies (red contours, starting at 0 s<sup>-1</sup>; each subsequent contour is -1 x 10<sup>-5</sup> s<sup>-1</sup>), and the data source’s climatological 4 mm day<sup>-1</sup> precipitation (black contour). For CFSR, anomalies are only shown if they are greater than 99% of randomly generated composite differences. For the coupled and atmosphere-only MEMs, anomalies are shown if 8 or more of the models agree on both the sign and significance (same as for CFSR) of the anomaly at any given location. .... 100

**Figure 3.11.** Linear trajectories of storms entering the SPCZ included in the composites shown in Figure 10 for (a) CFSR, (b) coupled model ensemble mean, (c)-(n) individual coupled models. Listed after the data sources name are the number of storms plotted (in parentheses) as well as the angle and speed of the red trajectory, which connects the mean starting and ending position for each data source. For angles, 0° is toward due north, 90° is toward due east, etc. .... 101

**Figure 3.12.** As Figure 3.11, but for atmosphere-only models. .... 102

**Figure 3.13.** As Figure 3.10, but replacing vorticity anomalies with moisture anomalies at two levels. Positive moisture anomalies are contoured at 850 hPa (light green) and 500 hPa (dark green) every 0.25 g kg<sup>-1</sup>; similarly, negative moisture anomalies are contoured

at 850 hPa (light brown) and 500 hPa (dark brown) every  $0.25 \text{ g kg}^{-1}$ . The same significance criteria are used for moisture that were used for precipitation and vorticity in Figure 3.10. .... 103

**Figure 3.14.** As Figure 3.13, but showing four individual atmosphere-only models. Significance criteria for showing precipitation/moisture anomalies is the same that was used for CFSR in Figures 3.10 and 3.13. .... 104

**Figure 4.1.** Climatological DJF 250 hPa wind (vectors, in  $\text{m s}^{-1}$ ), 850 hPa specific humidity (green contours, every  $2 \text{ g kg}^{-1}$ ), and precipitation (shading, in  $\text{mm day}^{-1}$ ) in a) CFSR, b) QTCM2 (CON32 experiment), and c) QTCM2 (CON32\_NOAUST experiment). .... 105

**Figure 4.2.** DJF biases in 250 hPa wind (vectors, in  $\text{m s}^{-1}$ ), 850 hPa specific humidity (green contours, every  $1 \text{ g kg}^{-1}$ ), and precipitation (shading, in  $\text{mm day}^{-1}$ ) compared to CFSR for a) QTCM2 (CON32 experiment) and b) QTCM2 (CON32\_NOAUST experiment). .... 107

**Figure 4.3.** Climatological DJF negative zonal stretching deformation (shaded, in  $\text{s}^{-1}$ ) in a) QTCM2 (CON32 experiment) and b) QTCM2 (CON32\_NOAUST experiment). CFSR DJF negative zonal stretching deformation (grey contours, every  $1 \times 10^{-6} \text{ s}^{-1}$ ) included in each plot for comparison. .... 108

**Figure 4.4.** Composite difference (weak-inflow minus strong-inflow phase) of wind (vectors, in  $\text{m s}^{-1}$ ), specific humidity (green contours, every  $0.5 \text{ g kg}^{-1}$ ), and precipitation (shading, in  $\text{mm day}^{-1}$ ) in a) CFSR, b) QTCM2 (CON32 experiment), and c) QTCM2 (CON32\_NOAUST experiment). Composite analysis based on anomalous 850 hPa zonal

wind in the box 140°W–120°W, 10°S–20°S, with the monthly mean subtracted from each value..... 110

**Figure 4.5.** Results from the W100 and S100 experiments. Each row shows a 2-hour mean (x-2 through x hours after imposed anomaly) from W100 (mean values in leftmost column, anomalies in right-center column) and S100 (mean values in left-center column, anomalies in rightmost column). Fields shown are derived 850 hPa wind (vectors, in  $\text{m s}^{-1}$ ), derived 850 hPa specific humidity (green contours, in  $\text{g kg}^{-1}$ ; every 2  $\text{g kg}^{-1}$  for mean values, every 0.25  $\text{g kg}^{-1}$  for anomalies), and precipitation (shaded, in  $\text{mm day}^{-1}$ )...... 112

**Figure 4.6.** As Figure 4.5, but with different times (48-120 hours)..... 114

**Figure 4.7.** As Figure 4.5, but showing results from the boundary layer instead of at 850 hPa for both wind and moisture. .... 116

**Figure 4.8.** As Figure 4.6, but showing results from the boundary layer instead of at 850 hPa for both wind and moisture. .... 118

**Figure 4.9.** As Figure 4.5, but showing results from W150/S150 instead of W100/S100. .... 120

**Figure 4.10.** Anomalous 850 hPa zonal wind (in  $\text{m s}^{-1}$ ), 850 hPa specific humidity (in  $\text{g kg}^{-1}$ ), and precipitation (in  $\text{mm day}^{-1}$ ) averaged in the indicated regions for each of the Wy and Sy experiments throughout the 240 hours following the imposed vorticity anomalies. .... 121

**Figure 4.11.** Anomalous 850 hPa zonal wind (in  $\text{m s}^{-1}$ ), 850 hPa specific humidity (in  $\text{g kg}^{-1}$ ), and precipitation (in  $\text{mm day}^{-1}$ ) averaged in the indicated regions using results from the composite analysis of Niznik and Lintner (2013) throughout their lead-lag analysis (5

days before a weak- or strong-inflow event through 5 days after a weak- or strong-inflow event).....	122
<b>Figure 4.12.</b> As Figure 4.5, except using the results of W100Q/S100Q instead of W100/S100. ....	124
<b>Figure 4.13.</b> As Figure 4.10, but showing the results of W100Q/S100Q instead of all Wy/Sy experiments.....	125
<b>Figure 5.1.</b> A schematic showing the key features associated with the weak-inflow (top) and strong-inflow (bottom) phases of the composite index. The weak-inflow phase is characterized by anomalous cyclonic circulation in the southeastern SPCZ and an associated increase in precipitation, anomalous cyclonic circulation south of Australia, and anomalous anticyclonic circulation south of the SPCZ. The strong-inflow phase is characterized by anomalous anticyclonic circulation in the southeastern SPCZ and an associated slight decrease in precipitation, anomalous anticyclonic circulation south of Australia, and anomalous cyclonic circulation south of the SPCZ. There is evidence to suggest that the storm track during the weak-inflow phase is further north than during the strong-inflow phase.....	126
<b>Figure 5.2.</b> Same as Figure 2.10, but using data from the RCP8.5 experiment. ....	127



## 1. Introduction

### 1.1 The South Pacific Convergence Zone: Introduction and Societal Relevance

The South Pacific Convergence Zone (SPCZ) is the largest area of climatologically contiguous convective precipitation spanning beyond the tropics. It consists of a zonal band of precipitation beginning near New Guinea ( $140^{\circ}\text{E}$ ,  $5^{\circ}\text{S}$ ) in the equatorial western Pacific and a diagonal band of storminess that extends southeastward into the Southern Hemisphere midlatitudes near  $120^{\circ}\text{W}$ ,  $30^{\circ}\text{S}$  (Figure 1-1). The convection is distinct from the Intertropical Convergence Zone (ITCZ) that lies north of the equator over the Pacific (along  $8^{\circ}\text{N}$ ; Figure 1-1). On a historical note, Bergeron (1930) and Hubert (1961) were the first to identify the SPCZ in surface observations and early satellite cloud imagery, respectively, while the term “SPCZ” itself is credited to Trenberth (1976) (Kiladis et al. 1989; Vincent 1994; Brown et al. 2011b). The SPCZ is responsible for a large fraction of the precipitation occurring across the South Pacific, particularly in austral summer (December-January-February, hereafter DJF), while intense convective heating in the SPCZ generates and modifies Rossby waves, giving the SPCZ a global influence (Brown et al. 2011b; Matthews 2012).

The properties of the SPCZ can be split into two regions: tropical and subtropical. Similar to the ITCZ, the tropical portion of the SPCZ, defined by Widlansky et al. (2011) as spanning  $165^{\circ}\text{E}$ – $165^{\circ}\text{W}$ ,  $20^{\circ}\text{S}$ – $5^{\circ}\text{S}$ , has a distinct zonal orientation with areas of maximum precipitation correlating well with the highest sea surface temperatures (SSTs) in the region. The subtropical portion, spanning  $165^{\circ}\text{W}$ – $135^{\circ}\text{W}$ ,  $35^{\circ}\text{S}$ – $20^{\circ}\text{S}$ , manifests a distinct off-zonal tilt and lies south of the highest SSTs in the region (Kiladis et al. 1989; Vincent 1994; Widlansky et al. 2011). [Widlansky et al. (2011) also highlight an

equatorial region, though it is essentially a blend of the western Pacific warm pool and a westward extension of the tropical portion and will not be considered as distinct within this work.]

From a societal perspective, the inhabitants of South Pacific island nations are dependent on SPCZ rainfall. Fiji, Kiribati, Nauru, Samoa, Solomon Islands, Tuvalu, and Vanuatu are all within the reach of tropical SPCZ precipitation, while Cook Islands, Niue, and Tonga lie closer to the transition between the tropical and subtropical SPCZ (Australia Bureau of Meteorology and CSIRO 2011a). Deviations from a typical year can result in substantial drought or flooding throughout the region (Brown et al. 2013a; Murphy et al. 2014). Additionally, the SPCZ is a region of tropical cyclogenesis with large interannual variability in the locations of cyclogenesis and numbers of cyclones (Vincent et al. 2011), as well as extreme sea level variability (Widlansky et al. 2014). Given the inherent societal impacts associated with the SPCZ and its variability, there is strong interest in better understanding the SPCZ in both present-day climate [e.g. Southwest Pacific Ocean Circulation and Climate Experiment (SPICE), see Ganachaud et al. (2007, 2014)] and projected future climate [e.g. the Pacific-Australia Climate Change Science and Adaptation Planning (PACCSAP) program, see Australia Bureau of Meteorology and CSIRO (2011a,b)].

## **1.2 Low- and High-Frequency SPCZ Variability**

The timescales on which each SPCZ region varies are quite different; the subtropical portion varies on timescales of one week or less, while the tropical portion varies primarily at two timescales: two weeks and 30-60 days (Widlansky et al. 2011).

Both portions of the SPCZ show signatures of synoptic variability, with the subtropical portion having more frequent interaction by a factor of two (Widlansky et al. 2011). SPCZ interaction with the Madden Julian Oscillation (MJO), highlighted in prior work, explains the 30-60 day variability of the tropical SPCZ (Matthews et al. 1996; Widlansky et al. 2011; Matthews 2012). The location and intensity of both tropical and subtropical SPCZ precipitation vary with the El Nino-Southern Oscillation (ENSO, Trenberth 1976; Folland et al. 2002; Vincent et al. 2011) on interannual timescales and the Interdecadal Pacific Oscillation (IPO, Folland et al. 2002; Linsley et al. 2008) on interdecadal timescales. Each of these modulators of SPCZ position is discussed hereafter, beginning with high-frequency (synoptic) variability and continuing to progressively lower frequency variability.

The earliest recognition that the subtropical SPCZ interacts with synoptic disturbances coincided with examination of the first full-disk satellite images of outgoing longwave radiation (OLR), summarized by Stretten (1973). Trenberth (1976) was first to suggest the SPCZ acts as a so-called “storm graveyard” region, while Trenberth (1991) noted that enhanced storm track activity near the exit region of the midlatitude jet ( $\sim 120^\circ\text{W}$ ) related to convection in the eastern SPCZ. Corroborating with these early observations, Berry et al. (2011) show the SPCZ to be a region of high annual mean quasistationary front frequency. Extensive work by Widlansky et al. (2011) and Matthews (2012) outlined the mechanisms associated with this interaction. Building on the theoretical results of Webster and Holton (1982) and Webster and Chang (1997), Widlansky et al. (2011) proposed the subtropical SPCZ is driven by eastward propagating synoptic disturbances (i.e. midlatitude storms), which travel along the subtropical jet over

the Indian Ocean and south of Australia. They soon encounter the “storm graveyard,” defined as a region where upper-level zonal stretching deformation ( $ZSD, \partial \bar{U} / \partial x$ ) is negative, slowing the group speed of those waves as they approach the central Pacific (Widlansky et al. 2011). This results in an increase in both wavenumber and wave energy density (Webster and Chang 1997), ultimately triggering deep convection due to the high SSTs and conditional instability in the SPCZ region (Widlansky et al. 2011; Matthews 2012). Additionally, the westerly duct in the upper troposphere over the equatorial Pacific refracts synoptic waves propagating across the South Pacific toward itself through Rossby wave dynamics (Webster and Holton 1982; Hoskins and Ambrizzi 1993; Matthews 2012). More succinctly, waves experience a combination of slowing and equatorward refraction as they propagate across the South Pacific and are ultimately steered into the SPCZ region where precipitating deep convection is triggered in the destabilized, rising air ahead of each cyclonic vorticity anomaly, consistent with quasi-geostrophic dynamics (Hoskins et al. 1985).

This relationship is further explored in Matthews (2012) initially through the framework of empirical orthogonal function (EOF) analysis of OLR. The first two modes of variability in a smaller region ( $175^{\circ}\text{E}$ - $180^{\circ}\text{E}$ ,  $10^{\circ}\text{S}$ - $15^{\circ}\text{S}$ ) within the tropical SPCZ are: (1) a southwestward shift of the SPCZ and an associated region of inhibited convection to the northeast; and (2) lower OLR along the main SPCZ axis with weakly inhibited convection to both the northeast and southwest (Matthews 2012). Both modes are associated with the eastward-propagating vorticity anomalies turning equatorward due to the equatorial Pacific westerly duct. The strength of the westerly duct varies based on the phase of both the MJO and ENSO (Matthews and Kiladis 1999a; Matthews and Kiladis

1999b), adding further complexity to the frequency of interactions. These anomalies do not persist; the associated diabatic heating from condensation of water vapor results in upper-level divergence that ultimately “spins down” the initial cyclonic anomaly (Matthews 2012). The second mode can be thought of as a “pulse” of energy in the SPCZ region; accordingly, the climatological SPCZ can be viewed as the sum of these pulse events (Matthews 2012).

The position of the eastern margin of the SPCZ is also sensitive to the amount of low-level (near 850 hPa) dry air inflow from the relatively dry southeastern Pacific basin on synoptic timescales. The extent of the Andes-forced subsidence zone, or “dry zone”, over the southeastern tropical Pacific is thought to limit the eastward extent of the SPCZ (Takahashi and Battisti 2007). Inhibition of precipitating deep convection within the dry zone establishes a climatological background state upon which the SPCZ varies and helps to explain the SPCZ’s characteristic northwest-to-southeast axis (or “diagonal”). High temporal frequency (~synoptic) changes in low-level inflow from the dry zone are related to shifts in the convective margin on the eastern flank of the SPCZ, with increased low-level inflow (e.g. stronger tradewinds) shifting the convective margin to the west (Lintner and Neelin 2008, hereafter LN08). The aforementioned interactions between the SPCZ and synoptic disturbances, as well as the sea surface temperature distribution in the south Pacific, also influence the shape of the SPCZ (Widlansky et al. 2011; Matthews 2012).

Early research focusing on both the SPCZ and MJO was based on the observation that some convective anomalies associated with the MJO propagate poleward and eastward along the SPCZ instead of strictly eastward (Wang and Rui 1990; Matthews et al. 1996). Matthews et al. (1996) developed a hypothesis explaining this tendency; in

summary, latent heating associated with MJO-enhanced warm pool convection results in deep ascent near the SPCZ, triggering convection. This connection was also proposed at the time as a potential explanation for the existence and orientation of the SPCZ (Matthews et al. 1996). Building on this, Matthews (2012) calculated the percentage of time each phase of the MJO resulted in a shifted SPCZ (EOF 1) and an enhanced SPCZ (EOF 2). Compared to the results from all days in the examined period, MJO Phases 3–6 result in increased probability of a shifted SPCZ while Phases 7–8 and 1 result in decreased probability, both significant at the 95% level. This difference is due to the expansion of the westerly duct in the central Pacific, leading synoptic disturbances to turn equatorward further west than usual (Matthews 2012). Phases 5–7 have an increased probability of an enhanced SPCZ while Phases 8 and 2–4 have a decreased probability, both again significant at the 95% level (Matthews 2012).

Trenberth (1976) was first to suggest a relationship between ENSO and SPCZ position: a northeastward displacement during El Niño and a southwestward displacement during La Niña (Folland et al. 2002). There is some non-linearity to this response during El Niño; Vincent et al. (2011) first highlighted this in classifying some particularly zonal SPCZs as “asymmetric.” This distinction is important when considering tropical cyclone activity in the South Pacific, as the seasonal position of the SPCZ affects source regions of tropical cyclogenesis (Vincent et al. 2011). More recently, Cai et al. (2012) have further highlighted the need to distinguish between individual El Niño events, as El Niños with strong eastern Pacific warming (Borlace et al. 2014) can effectively collapse the SPCZ onto the equator, merging it with the ITCZ in so-called “zonal SPCZ” events, thereby altering hydroclimate and its extremes across the

South Pacific. Folland et al. (2002) elucidated the connection between the SPCZ and the IPO: a positive/negative IPO has a similar influence on SPCZ position to El Niño/La Niña. Combinations of ENSO and IPO events with similar sign (i.e. +IPO and El Niño) tend to create more pronounced shifts in SPCZ position (Folland et al. 2002). Additionally, ENSO is a more significant factor in influencing SPCZ latitude east of 140°W (Folland et al. 2002).

### **1.3 The SPCZ in Climate Models**

Observational understanding aside, General Circulation Models (GCMs) show limited success in simulating the SPCZ region. A thorough analysis of models included in the Coupled Model Intercomparison Project Phase 3 (CMIP3, Meehl et al. 2007) reveals four that are unable to simulate an SPCZ (Brown et al. 2011b). Those that do tend to produce an SPCZ that is too zonal in orientation; applying a linear fit to precipitation maxima across the South Pacific to an observational dataset, the Climate Prediction Center's Merged Analysis of Precipitation (CMAP) yields an SPCZ slope of -0.29 degrees latitude per degree longitude whereas the CMIP3 multi-model mean slope is only -0.05 for non-flux adjusted models and -0.21 for flux adjusted models, with only two models simulating a slope less than -0.2 (Brown et al. 2011b). Some models simulate one ITCZ in each hemisphere, i.e. the well-known double ITCZ bias (Zhang 2001; Lin 2007; de Szoeke and Xie 2008; Bellucci et al. 2010; Brown et al. 2011b). The double ITCZ bias may not persist throughout the year; some models simulate an ITCZ that shifts toward the summer hemisphere, thus leaving the appearance of two ITCZs in the annual mean, while others confine this bias to the eastern Pacific; these biases in essence connect an

otherwise separate SPCZ to a spurious ITCZ (de Szoeke and Xie 2008; Bellucci et al. 2010; Brown et al. 2011b). Both the double ITCZ bias and “zonal” bias have been tied to errors in sea surface temperature (SST) across the South Pacific with cooler than observed equatorial SSTs, i.e. the “cold tongue,” playing a key role (Ashfaq et al. 2010; Widlansky et al. 2013). In turn, these biases alter the climatological position of the storm graveyard (Widlansky et al. 2011; explored further in Chapter 3).

Models included in the Coupled Model Intercomparison Project Phase 5 (CMIP5, Taylor et al. 2012) show little alleviation of the CMIP3 biases in the climatological mean sense, though fewer (two) are unable to simulate an SPCZ altogether (Brown et al. 2013b). Once again applying a linear fit to precipitation maxima across the South Pacific, Brown et al. (2013b) noted slopes of -0.25 and -0.28 degrees latitude per degree longitude in two separate observational datasets, whereas the CMIP5 multi-model mean slope is only -0.09 degrees latitude per degree longitude. As with the CMIP3 models, none of the CMIP5 models have a slope steeper than the observations. SPCZ shifts in accordance with El Niño and La Niña do improve in CMIP5 compared to CMIP3; while multiple CMIP3 models do not show skill in simulating a shift in SPCZ position related to the phase of ENSO, all but one CMIP5 model produced a correlation between SPCZ latitude and Niño3.4 SST significant at the 95% level (Brown et al. 2011b, 2013b). However, simulation of zonal SPCZs in CMIP3 and CMIP5 models is problematic; Cai et al. (2012) determined that 9 of 17 CMIP3 models and 12 of 20 CMIP5 models are incapable of capturing zonal SPCZ events. MJO simulation also appears slightly improved in CMIP5 models in terms of variance peaks, but propagation in most models remains too slow (Lin et al. 2006; Hung et al. 2013). It is likely that these biases will



affect SPCZ variability on MJO timescales, though no study has yet explicitly examined MJO-SPCZ interactions in CMIP5 models.

These pathological errors in SPCZ simulation lead to lowered confidence in projected anthropogenic warming-induced changes across the South Pacific as simulated by these models. A robust result from one analysis of CMIP5 models in the RCP8.5 experiment (the strongest forcing scenario included in CMIP5) is an increase in mean DJF precipitation within the SPCZ (Brown et al. 2013b). Subdividing the feature into an eastern ( $150^{\circ}\text{W}$ - $120^{\circ}\text{W}$ ,  $30^{\circ}\text{S}$ - $10^{\circ}\text{S}$ ) and western ( $160^{\circ}\text{E}$ - $150^{\circ}\text{W}$ ,  $30^{\circ}\text{S}$ - $0^{\circ}\text{S}$ ) portion shows the precipitation increase is primarily in the western portion, with most models simulating a drying in the eastern portion (Brown et al. 2013b). However, it is much less clear if there will be a shift in the axis of maximum precipitation – only half of the models simulate a significant shift in average DJF latitude: six northward and five southward (Brown et al. 2013b). A similar analysis using atmospheric models forced with bias-corrected Pacific SSTs suggests that the tendency for an increase in precipitation exists beyond a threshold of tropical warming (more than  $3^{\circ}\text{C}$ ) as a  $1\text{-}2^{\circ}\text{C}$  increase results in a 6% decrease in SPCZ rainfall, though it does not exceed the multi-model uncertainty of  $\pm 20\%$  (Widlansky et al. 2013). Beyond changes to the mean state, the frequency of zonal SPCZ events nearly doubles in response to anthropogenic warming in a subset of CMIP5 models capable of reproducing the first two modes of variability of an EOF analysis based on satellite-derived rainfall (Cai et al. 2012).

## **1.4 Motivation for Further Work**

Despite the research outlined above, current understanding of the SPCZ remains incomplete: Power (2011) identified the need for additional effort “to increase understanding [of the SPCZ] on many fronts, including the reasons why the SPCZ exists.” Recent advances in SPCZ theory (e.g. Lintner and Neelin 2008, Widlansky et al. 2011, Matthews 2012) suggest that the synoptic timescales may be particularly important, yet there has been no comprehensive assessment of the fidelity with which individual GCMs capture any of these interactions. One overarching theme of this dissertation is the elucidation of how well current generation climate models, specifically a subset of those included in CMIP5, can simulate SPCZ responses to various synoptic timescale influences. Chapter 2 focuses primarily on shifts in low-level inflow along the eastern margin of the SPCZ. Chapter 3 explores precipitation variability as well as storm graveyard biases in the South Pacific before focusing on storm interactions near the SPCZ. Another goal is to learn more about the time evolution of strong- and weak-inflow events along the eastern margin of the SPCZ; Chapter 4 explores the results of numerous experiments using an intermediate complexity climate model to force both wind and moisture anomalies near the SPCZ.

## **2. SPCZ Response to Varying Low-Level Inflow**

### **2.1 Introduction**

This chapter, drawn primarily from the Journal of Climate article “Circulation, Moisture, and Precipitation Relationships along the South Pacific Convergence Zone in Reanalyses and CMIP5 Models” by Matthew J. Niznik and Benjamin R. Lintner, examines one source of synoptic-scale SPCZ variability, changes to low-level inflow east of the SPCZ, as simulated by CMIP5 models. Comparing such variability to available reanalysis products may help to elucidate why current generation GCMs have difficulties simulating the SPCZ and, more broadly, the climate of the South Pacific. The rest of this chapter is organized as follows. Section 2.2 outlines the data and analysis methodology used in this paper. Section 2.3 is primarily concerned with the examination of the new daily composite analysis using reanalysis products (R1 and CFSR, Section 2.3.a) and GCMs (Section 2.3.b) at the compositing level, as well as the vertical extent and consistency of these anomalies in both the reanalysis products and the GCMs (Section 2.3.c). Section 2.4 contains a description of the results of the lead-lag analysis (composite plots of multiple variables in the days preceding and following the extrema of the composite index) for both the reanalysis and models. Finally, a summary of these findings is provided in Section 2.5.

### **2.2 Data and methodology**

LN08 used 5-day- (pentadal-) averaged 925-hPa zonal and meridional winds and 850-hPa specific humidity data at  $2.5^{\circ} \times 2.5^{\circ}$  resolution derived from daily average output from the R1 reanalysis (Kalnay et al. 1996) in their composite plots of the

difference in wind, moisture, and precipitation across the South Pacific between the positive and negative phase of their composite index. These phases were defined by the strength of zonal wind in the box 20°S–10°S, 140°W–120°W: the positive and negative phases contained all events for which the value was  $+1\sigma$  and  $-1\sigma$ , respectively (see LN08 for a more detailed description). Although the use of pentadal data suppresses noise, it precludes exploration of the growth and decay of observed anomalies on daily time scales. Based on preliminary analysis of model and reanalysis data showing little sensitivity to the choice of daily data over pentadal data (further confirmed by the similarity between pentadal and daily products in LN08), all analyses in this paper are performed using daily averages. R1 data is used as a starting point, but daily averages in the same fields and resolution from the CFSR (Saha et al. 2010) during the 32-yr period spanning 1979–2010 (available for both reanalyses) are examined as well. In addition to having approximately six times the resolution in the horizontal and double the number of vertical levels, the CFSR also improves upon R1 by including a coupled ocean model and updating many of the physical parameterizations in the atmospheric model (see Saha et al. 2010 for a detailed discussion). Figure 2.1 illustrates R1 and CFSR January (chosen for consistency with LN08 and computational efficiency) precipitation climatologies across the South Pacific for 1998–2010, the subset of years for which Tropical Rainfall Measuring Mission (TRMM) precipitation estimates (specifically, the 3B42 dataset) are available (Kummerow et al. 2000). While CFSR output matches TRMM estimates fairly well, R1 precipitation is too zonal, consistent with model biases evident in both CMIP3 and CMIP5 model suites (Brown et al. 2011b; Brown et al. 2013b). While there are potentially significant issues regarding the reliability of reanalyzed specific humidity and

precipitation (e.g., model biases in regions with sparse observations), the more realistic SPCZ in CFSR is a better reference moving forward until an appropriate observational dataset of equal length is available at daily time scale. Table 2.1 lists the 26 models for which output is examined in this work; all are included in CMIP5 (Taylor et al. 2012). These models were selected based on the availability of daily precipitation as well as pressure-level zonal wind, meridional wind, and specific humidity for at least one ensemble member included in the CMIP5 historical experiment (spanning 1850–2005). This experiment includes both observed anthropogenic and natural forcings during that period (Taylor et al. 2012).

The output of these models (with one exception) is further examined from the high emissions RCP8.5 projection spanning 2006–2300 (Taylor et al. 2012). This scenario, the strongest of the forcing scenarios in CMIP5, is similar to the choice of the A2 scenario in Brown et al. (2011a) for diagnosing future SPCZ change in CMIP3 models, though it should be noted that Widlansky et al. (2013) show the SPCZ response to warming is likely nonlinear. With a few exceptions (see Table 2.1), the first ensemble member for the CMIP5 historical and RCP8.5 experiments at daily resolution was obtained and regridded from the resolutions shown in Table 2.1 onto a  $2.5^\circ \times 2.5^\circ$  common grid, which is chosen because it matches the resolution of the data used in LN08. Models in which the product of native grid latitude and longitude is less than  $6.25^\circ$  squared were regridded to the analysis domain via area averaging; the remainder were regridded using linear interpolation.

The analysis intervals are 1960–99 and 2060–99 for the historical experiment and RCP8.5 experiment, respectively. Selection of these intervals was motivated by the

greater availability of model output in these periods and the desire to have two periods of equal duration. The first 30 days of January were isolated in each year, yielding a total of 1200 days for both the historical data and RCP8.5 data. Any models lacking zonal wind, meridional wind, specific humidity, and/or precipitation in the 1960–99 period for the historical experiment have been excluded from this study.

For visual clarity, only a subset of analyzed models are displayed. The criteria used to generate this subset are (i) the use of area averaging in the regridding process and (ii) the availability of RCP8.5 model output. The first criterion excludes eight models (BCC-CSM1.1, BNU-ESM, CanESM2, CMCC-CESM, FGOALS-g2, IPSL-CM5A-LR, MIROC-ESM-CHEM, and MIROC-ESM) and the second criterion excludes one (MIROC-4h), though with the exception of the first three, there are other models from the same groups represented in the panel plots. The model ensemble mean (MEM) also excludes the aforementioned models.

An important difference from the LN08 analysis is the definition of low-level inflow. While LN08 based their composites on zonal wind at 925 hPa, here 850 hPa is selected as the composite level as well as the lowest plotting level for wind since the PCMDI-archived CMIP5 output does not include the 925-hPa level at daily resolution. In prior analyses with CMIP3 data, which have zonal and meridional winds at both 925 and 850 hPa at daily resolution, an examination of the sensitivity of these results to the use of either 925 or 850 hPa revealed negligible change. This is consistent with the findings of LN08. In fact, this vertical consistency is not limited to these two levels and will be discussed further in Section 2.3.c.

For each day, the areal-mean zonal wind at 850 hPa (mean u850) was calculated within the region 20°S–10°S, 140°W–120°W. The position of the region is unadjusted relative to the location of the SPCZ in each model, as the results are relatively insensitive to the exact longitude of the box. These values were first normalized by subtracting from the daily values the January-mean u850 for each year in order to remove any biases due to low frequency variability such as the El Niño–Southern Oscillation (ENSO). Thus, the composite index is centered around zero and measures mean u850 departures from the yearly (January) mean. Previously, LN08 had excluded those Januaries in which a strong El Niño or La Niña occurred; this work does not since the results are insensitive to this exclusion. The weak-inflow phase (occurring when low-level inflow is weak, previously “positive phase” in LN08) and strong-inflow phase (occurring when low-level inflow is strong, previously “negative phase” in LN08) composites of zonal and meridional wind, specific humidity, and precipitation are then calculated by averaging all days for which the composite index exceeds a threshold relative to the standard deviation of the composite index ( $\sigma$ ); that is, for inclusion in the weak-inflow composite, the index must exceed  $+1 \sigma$  while for the strong-inflow composite, it must be less than  $-1 \sigma$ . Composite difference plots are then generated by subtracting the strong-inflow composite from the weak-inflow composite.

To quantify the significance of the wind, moisture, and precipitation anomalies, 1000 random weak-inflow and strong-inflow phases were generated for each reanalysis product and model, each containing approximately 16% of available days ( $\approx 153$  days for the reanalysis periods,  $\approx 192$  days for the model periods), consistent with the percentage of data expected to lie in either the positive or negative tail of a normal distribution with

magnitudes above  $1 \sigma$ . Moisture and precipitation anomalies are considered significant if they are greater than 99% of these random anomalies; wind vectors are considered significant if either the zonal or meridional wind anomaly exceeds 99% of the random anomalies in the same direction. Similarly, for plots that show anomalies in the weak- and strong-inflow phases compared to the mean state, anomalies are considered significant if they are greater than 99% of these random differences from the mean state.

Lead-lag composites at “day 0” were generated using the same composite index, but restricted to only those days defined as the local maxima and minima during weak-inflow and strong-inflow phase events, respectively. Here, maxima or minima are defined such that a given day meets the standard deviation threshold for inclusion in the previous weak-inflow (strong inflow) composite plots and has an index value greater than (less than) the two preceding and two following days. (Since the index is only calculated in January, the first two days of each month lack two preceding days and are thus never considered as peaks; likewise, the last two days of each month lack two following days and are also excluded.) This methodology was chosen to ensure that certain anomalies, such as synoptic disturbances, are not completely lost in averaging since weak-inflow and strong-inflow phase events can occur across successive days. The included composite plots, which subtract the mean January state of the reanalysis/model from the weak-inflow or strong-inflow composite, allow adequate determination of those features associated with the rise and decay of each phase of the composite index. To facilitate identification of anomalous cyclones and anticyclones, sea level pressure (SLP) is also analyzed here.



## 2.3 Low-level inflow composites

### 2.3.a Reanalyses

Figure 2.2 depicts composite differences for (a) 850-hPa winds and moisture and (b) precipitation for R1 (left) and CFSR (right). Note that the R1 results are quite similar to those in LN08 using pentadal data for wind and moisture (cf. their Figs. 1a and 1b). In addition, application of a significance test confirms that the wind and moisture anomalies near the compositing region, that is, the northern side of the anomalous cyclonic circulation centered at 30°S, 130°W, are significant. The R1 precipitation field reveals an interesting, albeit not completely unexpected, divergence from the previously used CMAP fields of LN08: instead of showing a shift in convection along the southeastern edge of the SPCZ associated with weakened easterlies in the compositing region, R1 indicates a simple expansion of precipitation farther to the southeast, thereby (partially) overcoming its tendency to simulate an overly zonal and tropical SPCZ. This result is consistent with many of the CMIP5 models that exhibit a similar climatological SPCZ orientation (see Section 2.3.b). Additionally, the significance of the precipitation expansion is now confirmed.

The CFSR results compare well with R1 in terms of wind anomalies and their significance. However, the distribution of moisture anomalies in CFSR is notably different. In particular, the moisture anomalies associated with the cyclonic circulation manifest a more distinct tilt, that is, a clockwise rotation of  $\sim 45^\circ$ , compared to the more zonal orientation evident in R1. The CFSR moisture anomaly orientations both at 850hPa and throughout the entire depth of the troposphere (see Section 2.3.c) are consistent with the LN08 results using Special Sensor Microwave Imager (SSM/I) total-column water

vapor, suggesting that the CFSR fields are more realistic. Additionally, the CFSR data reflect a more pronounced significant shift in precipitation, with a much stronger zonal gradient of anomalous precipitation along the southeastern extent of the SPCZ. Like Figure 2.2, Figure 2.3 illustrates results for CFSR wind and moisture, but for the shorter period 1998–2010 so as to take advantage of available TRMM 3B42 precipitation for comparison. Despite the shorter period considered, the wind and moisture composites are quite similar. The precipitation results do not cleanly match R1 or CFSR; like R1, precipitation shows a significant southeastward expansion during the weak-inflow phase, though the spatial orientation of the precipitation is much more similar to CFSR.

### *2.3.b CMIP5 models*

Composite analysis was also performed on the selected subset of 17 CMIP5 models (Figures 2.4 and 2.5). For visual clarity, wind and moisture anomalies are only plotted where they exceed 99% significance. Note that the wind vectors plotted for the MEM in Figure 2.4 are significant at that grid cell in at least one direction in a simple majority (nine) of the models. The same criterion is applied to specific humidity, although this condition is more restrictive since the wind composites need only be significant in one direction. In any case, the cyclonic circulation evident in the reanalyses is robust across all models, though the precise location of the center of circulation varies ( $\sim \pm 5^\circ$ ). The moisture anomalies are more varied in location, although the general “tilt” of the  $0 \text{ g kg}^{-1}$  line through the center of the circulation is in good agreement with CFSR and is thus insensitive to the spread in climatological slopes of the SPCZ diagonal in the models. A more realistic CMIP5 simulation of the January precipitation climatology does

not correspond strongly to the fidelity with which the models reproduce the observed high-frequency wind and moisture composite anomalies.

The precipitation composites in Figure 2.5 reveal less consistency in response than those for either wind or moisture. While the  $4 \text{ mm day}^{-1}$  contours suggest many models have a similar response to R1 in terms of a simple significant southeastern expansion of precipitation during the weak-inflow phase, the shaded differences in precipitation confirm that many models do have a zonal gradient in anomalous precipitation south of the compositing region, consistent with the idea of a precipitation “shift” between phases. This complexity is perhaps most evident in the model ensemble mean. Thus, despite the models simulating very similar circulation and, to a lesser extent, moisture anomalies, their precipitation responses are highly variable, potentially related to equally variable convection schemes and SST patterns.

### *2.3.c Vertical structure*

Since the models appear to capture the observed wind and moisture anomalies, it is of interest to examine the vertical structure of these anomalies. This is especially important considering the potential for interactions between upper- and lower-level influences acting in the SPCZ region, for example, to SPCZ–synoptic disturbance interactions, previously explored in upper-level vorticity fields (Widlansky et al. 2011; Matthews 2012). Figure 2.6 highlights the vertical structure of the wind and moisture anomalies at four levels in both of the CFSR as well as the CMIP5 MEM (R1 is omitted, though it has a similar vertical structure) using the previously discussed significance metrics. The vertical structure in CFSR is remarkably consistent through 500 hPa (wind

through 250 hPa), with an increase in the magnitude and area of significance of the moisture anomalies at 700 and 500 hPa compared to 850 hPa. This result is consistent with vertical moisture profiles obtained from radiosondes at Nauru, which suggest that moisture in the free troposphere increases more than the boundary layer moisture in transition from a tropical, nonconvective environment toward a convective environment (Holloway and Neelin 2009). The models are similarly consistent, with at least half agreeing on the significance of the moisture anomalies to the northeast and southwest of the cyclonic anomaly. The deep-layer equivalent barotropic structure seen here confirms that the effects of varying low-level inflow in the SPCZ are not confined to the lower atmosphere, consistent with the vertical extent of deep convection. This result is also consistent with earlier work showing a similar structure associated with the South Atlantic Convergence Zone (Robertson and Mechoso 2000).

## **2.4 Lead-lag composites**

### *2.4.a Reanalysis*

Figure 2.7 illustrates the development and decay of both weak-inflow and strong-inflow phases of the composite index in CFSR in terms of wind, moisture, and precipitation on three specific days; each of these days is referred to based on its timing before or after the peak of a phase; for example, two days before a peak is denoted as day -2, while two days after is day 2. Aside from the cyclonic anomaly associated with an eastward SPCZ shift, two other particularly broad regions of anomalous circulation are evident throughout the weak-inflow phase: an anomalous cyclone south of Australia and an anomalous anticyclone in the south-central Pacific ( $\sim 60^\circ\text{S}$ ,  $140^\circ\text{W}$ ). Similar anomalies

exist during the strong-inflow phase in the same regions, though they are of opposite sign and are most evident on day  $-2$ . Figure 2.8 (left panel) shows SLP anomalies from day  $-5$  through day 0 for both phases. The two broad regions of anomalous circulation are confirmed in the SLP fields on day  $-2$  and day 0. Of greater interest, however, is the difference in propagation of negative SLP anomalies between the two phases. During the weak-inflow phase, a negative SLP anomaly centered around  $35^{\circ}\text{S}$ ,  $150^{\circ}\text{W}$  slowly propagates eastward from day  $-5$  to day  $-2$ . From there, it drifts toward the northwest and, ultimately, becomes recognized as the cyclonic circulation south of the composite region. In contrast, a similar negative SLP anomaly exists at  $40^{\circ}\text{S}$ ,  $165^{\circ}\text{W}$  on day  $-5$  during the strong-inflow phase, but it drifts toward the southeast instead and effectively avoids interaction with the composite region.

The SLP composites hint at differences in the interactions of midlatitude transients with the SPCZ, suggesting the following hypothesis: the Southern Hemisphere storm track [collocated with the westerly jet axis, see Nakamura and Shimpf (2004)] preceding a weak-inflow peak is oriented in such a way that it increases SPCZ–storm interaction near the compositing region. Figure 2.9 shows the composite 250-hPa wind fields for the weak-inflow and strong-inflow phases averaged between day  $-5$  and day  $-3$ . Three regions of interest stand out in the difference between the two phases and are significant at the 99th percentile: 1) the subpolar jet (SPJ) south of Australia, 2) the reconnection of the SPJ and subtropical jet (STJ) in the central Pacific ( $\sim 145^{\circ}\text{W}$ ), and 3) the westerly duct in the eastern equatorial Pacific ( $\sim 100^{\circ}\text{W}$ ). The SPJ region of increased strength ( $\sim 40^{\circ}\text{S}$ ,  $120^{\circ}\text{E}$ – $180^{\circ}$ ), or alternately its northward displacement, during the weak-inflow phase is collocated with the anomalous circulations south of Australia

shown in Figures 2.7, indicating another equivalent barotropic response. Beyond 160°E the weak-inflow phase shows two jets of similar magnitude while the strong-inflow phase has a stronger SPJ. Additionally, the STJ streak in the weak-inflow phase does not turn poleward until nearly 160°W, or ~30° farther to the east than in the strong-inflow phase. Both features hint at a northerly displaced storm track during the weak-inflow phase consistent with the SLP results, particularly if more storms follow the STJ. While the STJ is weak and not the dominant SH jet in austral summer, synoptic disturbances still propagate along it (Nakamura and Shimpo 2004). The presence of a westerly duct in the equatorial Pacific eliminates an interhemispheric barrier and allows eddies to propagate across the equator (Webster and Holton 1982; Hoskins and Ambrizzi 1993; Matthews 2012).

Additional composite analyses based on the 250-hPa zonal wind at a lead time between 3 and 5 days in each of the regions of interest outlined above were performed (not shown). Most composites show a circulation anomaly similar to that seen in Figures 2.2 for CFSR, although the areal mean anomalous winds in the region bounded by 20°S–10°S, 140°W–120°W are consistently weaker (~20% of the original composite value) and the characteristic anomalous circulation is broader and less organized. The moisture and precipitation responses are similarly weak. Though some of the wind and moisture anomalies are significant at the 99th percentile, few if any of these anomalies are in the vicinity of the original circulation and moisture anomalies (those seen in Figures 2.2–2.4). As a result, direct confirmation that differences in the storm track and position of the eastern equatorial Pacific westerly duct are responsible for the original composite analysis's hallmark circulation, moisture, and precipitation anomalies is weak.

#### 2.4.b CMIP5 models

Analogous to Figure 2.7, Figure 2.10 depicts the CMIP5 MEM (calculated by averaging day -2 results across all models, etc.) wind and moisture composites. There is remarkable agreement on the existence of the anomalous anticyclone in the central Pacific during the weak-inflow phase leading up to day 0 and beyond, despite the moisture anomalies showing broad disagreement. The individual models (not shown) behave similarly to Figure 2.4 in that they exhibit moisture anomalies of similar magnitude to CFSR but disagree substantially on the location of these anomalies. Similarly, the strong-inflow phase shows agreement on the existence of an anomalous cyclone in the central Pacific. On day -2, there are hints of an anomalous cyclone (anticyclone) in the weak-inflow (strong-inflow) phases south of Australia, though they are displaced to the east compared to CFSR, and neither shows much coherence beyond day -2. Though the hallmark circulation and moisture anomalies associated with the weak- and strong-inflow phases (see Figure 2.4) are significant at the 99th percentile in a majority of models, particularly on day 0, neither the anomalous circulations south of Australia nor those in the south-central Pacific meet the significance threshold (not shown).

Based on the connection between the anomalous circulations both south of Australia and in the south central Pacific and the strength and northward displacement of the South Pacific jet, it appears that the orientation of the feature is dissimilar enough from CFSR in many models to produce a different response or none at all. Figure 2.8 (right panel) confirms the central Pacific anomalies as well as the existence and eventual

decay of the anomalies near Australia. Unlike CFSR, there is less of a sense that the negative SLP anomaly propagates and stalls near the SPCZ in the weak-inflow phase; instead, it appears that the negative SLP anomaly associated with the anomalous circulation south of the composite region simply grows in magnitude by day 0. Analysis of individual models (not shown) confirms that the MEM results are not a product of averaging; each model exhibits a similar response.

The three areas of anomalous winds outlined for CFSR at 250 hPa between the weak-inflow and strong- inflow phases related to storm tracks appear in the CMIP5 models though they are consistently weaker and displaced (not shown). Additionally, all three are rarely recognizable in an individual model. Confirming this lack of coherence, the model ensemble mean shows very weak anomalies related to the SPJ south of Australia and the westerly duct in the equatorial eastern Pacific and no anomaly in the central Pacific associated with the STJ. That the models in fact simulate varying low-level inflow further confirms that the variation of the storm track or westerly duct position is not the sole influence.

#### *2.4.c Vertical structure*

In both CFSR and the MEM, the day 0 circulation anomaly tends to form and decay nearly simultaneously at all vertical levels. Specific humidity fields, shown in Figure 2.11 as composite differences, do show some spatial and temporal differences. On day -2, both CFSR and the MEM manifest positive moisture anomalies forming in the compositing region at 500 hPa, while the response at 850 hPa is somewhat muted. By day 0, positive moisture anomalies have formed at both levels, though the anomaly at 850 hPa



extends farther southeast. In contrast, the negative moisture anomaly southwest of the compositing region forms by day –1 and persists through day 2 at 850 hPa, though there is a more subtle response at 500 hPa. The difference in moisture response could be from differences in the anomalous source (e.g., deep convection at 500 hPa versus advection at 850 hPa), though additional work is needed to separate the components of the response.

## **2.5 Summary**

Both reanalysis products and CMIP5 models are capable of simulating shifts in the eastern margin of the SPCZ associated with synoptic time scale changes to low-level inflow along the eastern side of the SPCZ; during the weak-inflow phase, SPCZ precipitation expands toward the east and south while during the strong-inflow phase it is constrained further west. Characteristic wind and moisture anomalies associated with SPCZ shifts are equivalent barotropic and extend to the top of the troposphere. A lead-lag analysis suggests that atmospheric conditions during the weak-inflow phase are more favorable for SPCZ-storm interactions. While individual model results show biases particularly in their precipitation responses, these results overall suggest that CMIP5 SPCZ model biases are not due to poor simulation of synoptic low-level inflow variability.

### **3. Extratropical-Tropical Interactions and Synoptic Variability in the SPCZ**

#### **3.1 Introduction**

This chapter, drawn primarily from the Journal of Climate article “The Role of Tropical-Extratropical Interaction and Synoptic Variability in Maintaining the South Pacific Convergence Zone in CMIP5 Models” by Matthew J. Niznik, Benjamin R. Lintner, Adrian J. Matthews, and Matthew J. Widlansky, shows the application of several metrics to quantify the extent to which CMIP5 models simulate key interactions on synoptic timescales, particularly between synoptic disturbances and the SPCZ. Section 3.2 outlines the data and analysis methodology used in this paper. Section 3.3 provides an overview of climatological precipitation biases in the models analyzed and examines model variability on synoptic timescales. Section 3.4 outlines model biases in the intensity and position of the storm graveyard. Section 3.5 shows the results of composite analyses constructed to examine SPCZ-storm interactions. Finally, a summary of these results is given in Section 3.6.

#### **3.2 Data and methodology**

Twelve CMIP5 models were examined in this work (Table 3.1); all had output from the following four variables available at daily resolution in both the CMIP5 "historical" and "AMIP" (Atmospheric Model Intercomparison Project) experiments: zonal wind, meridional wind, specific humidity, and precipitation. With the exception of CCSM4, the models also had top of atmosphere (TOA) outgoing longwave radiation (OLR) output available at the same temporal resolution in both experiments. The two

experiments differ principally in ocean and sea ice; the historical experiment (1850–2005) is a full ocean-atmosphere coupled integration (Taylor et al. 2012), whereas the AMIP experiment (1979–2008) is an atmosphere-only configuration forced by observed SST and sea ice. For clarity, the CMIP5 model output from the historical and AMIP experiments will be referred to as coming from coupled models and atmosphere-only, respectively. Both model sets include observed anthropogenic and natural radiative forcing in their respective time spans.

All available output was regridded to a common  $2.5^\circ \times 2.5^\circ$  latitude-longitude grid via area averaging. For those analyses requiring annual data, all available days in each experiment, 46 years for coupled (1960–2005) and 30 years for atmosphere-only (1979–2008), were used to ensure a representative distribution of variability in each model and experiment is captured. (For completeness, select analyses were repeated using a shorter time period for coupled models matching the atmosphere-only time period length, though the results were qualitatively similar and are not shown here.) For those analyses requiring DJF data, all days in those months were included with the exception of days from the first January, first February, and last December of the time span since none are part of a fully contiguous DJF; thus, DJF analyses contain one less “year” (45 for coupled, 29 for atmosphere-only).

As a basis for comparison in the relatively data sparse South Pacific, the National Center for Environmental Prediction (NCEP) Climate Forecast System Reanalysis (CFSR; Saha et al. 2010) is used in all analyses during the 32-year period spanning 1979–2010 (variables examined in the CMIP5 models are also available for CFSR during this period). Niznik and Lintner (2013) showed that CFSR captures the climatological

position of the SPCZ well (c.f. Figure 3.2). Precipitation estimates from the Tropical Rainfall Measuring Mission (TRMM) 3B42 dataset (Kummerow et al. 2000) are used to develop estimated precipitation intensity histograms, with the caveat that the record used is comparatively short (December 1998–February 2013). Additionally, data from the Climate Prediction Center (CPC) Merged Analysis of Precipitation (CMAP, Xie and Arkin 1997) spanning December 1979–February 2011 is used to supplement TRMM estimates for climatological precipitation values in the subtropical ( $135^{\circ}\text{W}$ – $165^{\circ}\text{W}$ ,  $20^{\circ}\text{S}$ – $35^{\circ}\text{S}$ ) portion of the SPCZ. It is worth noting that precipitation (and specific humidity) values across the South Pacific remain somewhat uncertain; while these products (TRMM, CMAP, CFSR) do have some notable disagreement (e.g. 1 mm day<sup>-1</sup> difference in precipitation in the subtropical SPCZ between TRMM and CFSR, see Table 3.2), the range of values among these data sources as well as their qualitative aspects are still useful for comparison to model output.

As a measure of the spread of convective activity, precipitation standard deviations are calculated both for the entire record as well as on synoptic timescales, defined here as 14 days or less. In order to isolate synoptic precipitation variability, a fast Fourier Transform (FFT) was calculated and a time series was then reconstructed from only those signals with periods of 14 days or less; the synoptic precipitation variability corresponds to the standard deviation of this time series. Additionally, principal uncertainty patterns (PUPs) are generated by performing empirical orthogonal function analysis replacing the time dimension with  $N$  model realizations of a given field (see Anderson et al. submitted); in this way, key inter-model differences between simulated variables can be isolated and quantified. Here, PUPs are calculated for both total and

synoptic precipitation variability to aid in grouping models based on precipitation variability magnitude. Precipitation histograms at the daily timescale in DJF are generated in the subtropical region of the SPCZ as well as for TRMM and model output. All precipitation counts from grid cells within an individual region are used to construct the histograms with bin spacings of  $2.5 \text{ mm day}^{-1}$  (with three exceptions: the first bin of each histogram spans  $0\text{--}0.5 \text{ mm day}^{-1}$ , thus grouping zero and trace precipitation together, the second bin spans  $0.5\text{--}2.5 \text{ mm day}^{-1}$ , and the final bin captures all events greater than  $100 \text{ mm day}^{-1}$ ). This methodology was repeated using only those grid cells in each region that have climatological precipitation values greater than  $4 \text{ mm day}^{-1}$ , though the results are robust to this change. Biases with respect to TRMM for each model are obtained for the daily timescale by calculating the difference between each model's counts and the TRMM counts and then normalizing by the TRMM counts in each bin (e.g. 0.3 represents 30% higher counts on average in a particular model, while -0.3 represents 30% lower counts).

The timescale dependence of the SPCZ variability is diagnosed from power spectra calculations. Daily values of TOA OLR from interpolated observed values in the period 1979–2012 (see Liebmann and Smith 1996), CFSR, and model output in a  $5^\circ \times 5^\circ$  subset ( $147.5^\circ\text{W}\text{--}152.5^\circ\text{W}$ ,  $25^\circ\text{S}\text{--}30^\circ\text{S}$ ) of the subtropical SPCZ were analyzed, following the precedent of spectral analyses performed by Widlansky et al. (2011) and Matthews (2012). While the observational dataset should not be used for direct quantitative comparison with the model output because observations cannot truly capture total TOA OLR, the means and variances of both products are qualitatively similar (George Kiladis, personal communication). For each data source, the time series of OLR

at each grid cell in the subtropical SPCZ was converted to anomalous OLR by subtracting the day-specific climatological OLR value obtained by combining the mean OLR and the first three harmonics of the unsmoothed annual cycle in observations (i.e., anomalies on 1 January 1980 were calculated by subtracting an idealized climatological value of OLR specific to that day of year from the raw value). OLR values were then averaged spatially, resulting in one time series for the subtropical SPCZ, and a power spectrum was then calculated (frequency range  $1/n$  through 0.5 with interval spacing  $1/n$ , where  $n$  is the total number of days in the time series). The power spectra was smoothed by a 181-point running mean (represents approximately 2% of all points for the coupled model data and 3% of all points for CFSR and atmosphere-only models) to remove noise due to a high density of frequencies on short timescales; e.g., 33% of the calculated points are between a period of 2 and 3 days. In addition, a theoretical background red-noise spectrum was calculated by assuming that the time series reflects a first-order Markov process and using the lag-1 autocorrelation coefficient, with 95% confidence intervals obtained from a chi-squared test assuming 362 ( $2 \times 181$ ) degrees of freedom. The procedure for precipitation power spectra calculations is identical. In order to normalize the spectra for comparison, all power spectra are multiplied by the number of years in the source time series and then divided by the smallest number of years in any given comparison (32 for coupled model TOA OLR, 30 years for atmosphere-only TOA OLR, and 15 years for coupled and atmosphere-only precipitation).

For the storm graveyard calculations, the zonal derivative of zonal wind ( $\partial \bar{U} / \partial x$ ), i.e. the zonal stretching deformation ZSD, was calculated via a simple centered difference scheme for CFSR and model output. Though Widlansky et al. (2011) analyzed

data at the 200 hPa level, the 250 hPa level is chosen here to match the standard archived CMIP5 model output. Comparison of the storm graveyard shape and intensity at these two levels in the CFSR (e.g., Saha et al. 2010) shows minimal difference. For inter-model comparison, as well as comparison with CFSR, the magnitude and location of the minimum in ZSD in both the reanalysis as well as the CMIP5 models is calculated in the region  $180^{\circ}\text{W}$ – $110^{\circ}\text{W}$ ,  $40^{\circ}\text{S}$ – $15^{\circ}\text{S}$ , chosen primarily to capture the storm graveyard while excluding an area of strong negative ZSD located in the eastern equatorial Pacific.

To diagnose the synoptic characteristics of the SPCZ variability, composite analyses were performed based on an index created by averaging daily 250-hPa vorticity anomalies from monthly means over the region centered on CFSR's climatological ZSD minimum ( $140^{\circ}\text{W}$ – $127.5^{\circ}\text{W}$ ,  $30^{\circ}\text{S}$ – $27.5^{\circ}\text{S}$ ). All days with a vorticity index less than 1.5 standard deviations below the mean, i.e., strongly negative, cyclonic vorticity, that are also the minima in centered five-day periods are included in the composite. Additionally, a lead-lag analysis is performed by considering composites for the six-day period before and after the composite days. Note that separate compositing indices were created for the CFSR data set and for each of the model data sets. To check the robustness of the methodology, an alternative index was created by averaging the vorticity anomaly over a similarly sized region centered on the climatological ZSD minimum for each model rather than using the same CFSR-defined region for each model; the results were qualitatively similar.

The mean speed and linear trajectory of each storm contributing to the composites were also calculated, using a simple vorticity back-tracking algorithm. For each event in the composite analysis, the algorithm searches a circle with a radius of 5 grid cells and

centered on the day 0 vorticity anomaly (i.e. between due west and due south of the anomaly) for a negative vorticity anomaly on the previous day (day -1). If an anomaly is found, the same process is repeated, but moving the starting location to the anomaly at day -1 in order to find the anomaly on day -2. If no negative anomaly is found on day -1 or day -2, that particular anomaly is excluded from the trajectory plots. Additionally, all vorticity anomalies that do not propagate toward the SPCZ between due east and due north from day -2 through day 0 are excluded from the analysis. The chosen range of approach trajectories is consistent with current SPCZ-storm interaction theory; upper-level vorticity anomalies approach the SPCZ along the Southern Hemisphere subtropical jet and are steered equatorward near the storm graveyard (Widlansky et al. 2011; Matthews 2012). The excluded approach angles could be associated with equatorial waves (especially those propagating toward the west) or the algorithm erroneously associating unrelated convection with the day 0 event. Using this algorithm, a mean speed and trajectory is calculated as the trajectory from the mean position of anomalies on day -2 to the mean position of all anomalies on day 0.

### **3.3 Precipitation variability in the SPCZ**

#### *3.3.a Model precipitation biases*

Before presenting the synoptic analysis, it is necessary to first summarize the climatological model biases across the South Pacific. Precipitation climatologies across the South Pacific in both coupled and atmosphere-only models are depicted in Figures 3.1 and 3.2, respectively, for the 12 models examined in this work in addition to TRMM, CFSR, and the model ensemble mean (MEM); for comparison, the CMAP precipitation



climatology is shown in Figure 1.1. Coupled model biases in the region include a poleward displacement of and enhanced convection in the Northern Hemisphere ITCZ, unrealistically intense precipitation along 10°S in the eastern Pacific, and a dry bias in the western equatorial Pacific (150°E–180°) associated with the cold tongue bias. Stronger than observed precipitation in the southeastern Pacific, as shown in the MEM, stems from a combination of models simulating an SPCZ that extends farther east as well as the generation of a spurious Southern Hemisphere ITCZ (de Szoeke and Xie 2008; Belluci et al. 2010; Brown et al. 2011). Individual models do not necessarily exhibit both of these biases, e.g., CMCC-CM shows a bias solely due to the eastward-extended SPCZ, IPSL-CM5A-MR shows a bias solely due to the Southern Hemisphere ITCZ, and MRI-CGCM3 shows evidence of both. Additionally, the dry bias in the western equatorial Pacific manifests considerable spread. Whereas CSIRO-Mk3.6.0 and MPI-ESM-LR/MR both have a strong dry bias, CNRM-CM5 has notable precipitation on the equator in the region 150°E–180°. Averaging precipitation over the subtropical SPCZ (Table 3.2) reveals that despite an approximate 1 mm day<sup>-1</sup> difference between TRMM and both of CFSR and CMAP, many individual coupled models, in addition to the MEM, simulate lower values than both estimates and reanalysis.

In the climatological sense, forcing a model with realistic SSTs in the region alleviates most precipitation biases (the atmosphere-only models in Figure 3.2 and mean precipitation values in Table 3.2), as suggested in previous studies (e.g., Widlansky et al. 2013). However, there remains a tendency for models to simulate an SPCZ farther northeast than observed. As a first step in determining how well the models simulate synoptic-scale variability, and how errors in synoptic-scale simulation may impact biases

in the SPCZ, the standard deviation of precipitation across the South Pacific in atmosphere-only models both for all timescales (Figure 3.3) and for synoptic timescales only (14-day high-pass filtered, Figure 3.4) is shown. It is immediately apparent that the models differ considerably in the magnitude of variability within the  $4 \text{ mm day}^{-1}$  contour of the SPCZ. Additionally, those models that tend to simulate smaller precipitation standard deviations overall also show substantially less precipitation variability on the northern margin of the SPCZ compared to the southern edge. These magnitudes are consistent with those obtained using the coupled models (not shown); regardless of where the SPCZ is located in coupled models, precipitation variability is enhanced relative to surrounding regions but with sizeable spread across the ensemble. However, fewer coupled models show a low bias on the northern edge of the SPCZ.

For a more rigorous confirmation of the relative importance of the precipitation variability differences among atmosphere-only models, a PUP is performed based on empirical orthogonal function (EOF) analysis of the standard deviations of precipitation across those models. This shows a very strong signal in the SPCZ and not elsewhere; the leading PUP, which explains greater than 60% of the variance using both the full precipitation signal as well as the synoptic-only precipitation signal, exhibits its strongest spatial loading in the SPCZ. Table 3.3 summarizes the quantitative grouping of models based on the ratio of precipitation standard deviation within the subtropical SPCZ in each model compared to TRMM, as well as the sign of the principal component of the first PUP using both the full precipitation signal and the synoptic-only precipitation signal. Those models that both exceed 0.8 for a standard deviation ratio and have a negative loading for the first PUP (consistent with higher precipitation standard deviations) using

both signals are considered high-variability group (HVG) models. Those that meet none of the aforementioned criteria are considered low-variability group (LVG) models. The remaining models are considered intermediate-variability group (IVG) models.

The relevance of this precipitation variability to precipitation on daily time scales is shown in the precipitation histograms for TRMM, coupled models, and atmosphere-only models (Figure 3.5). Those models in the HVG (mean error -0.16) tend to simulate histograms comparable to TRMM. Conversely, LVG histograms tend to disagree more with respect to TRMM (mean error -0.43), especially INM-CM4 and NorESM1-M, which very noticeably diverge from the other model histograms beyond 35–40 mm day<sup>-1</sup> regardless of coupling. A majority of the models simulate too much light precipitation at the expense of both heavy precipitation and dry days, which is a well-known bias in climate models, although somewhat alleviated in CMIP5 compared to CMIP3 (DeAngelis et al. 2013, Sillmann et al. 2013). Among coupled models, CMCC-CM and MRI-CGCM3 actually show positive errors; however, both CMCC-CM and MRI-CGCM3 simulate too low a climatological precipitation value (see Table 3.2) in the subtropical SPCZ (more than one standard deviation below the model mean). Both models are capturing light precipitation accurately, underestimating precipitation in the range 15-50 mm day<sup>-1</sup>, and overestimating precipitation heavier than 50 mm day<sup>-1</sup>. CNRM-CM5 perhaps best illustrates the point that even with reasonable precipitation climatology and variability, a model may still display some subtle biases on the synoptic timescale; in addition to underestimating dry days and overestimating light precipitation, it underestimates precipitation in the range 15-50 mm day<sup>-1</sup> but performs well toward the tail of the distribution (high precipitation).

In the case of atmosphere-only models, four out of five HVG models now have large positive errors (mean error 0.63), with most of the error evident at precipitation values greater than 50 mm day<sup>-1</sup>. The most extreme case of this is MRI-CGCM3 (error 1.53), the only model capable of simulating mean subtropical SPCZ precipitation greater than CFSR. Conversely, the LVG models show little alleviation of error (mean error 0.44) despite improved climatological representation of the SPCZ. Thus, it is not immediately obvious that atmosphere-only models are simulating more realistic histograms than coupled models — only five models show a decrease in error, and arguably only GFDL-CM3 shows notable improvement of those five. However, many models do show an increase in precipitation values between 15-50 mm day<sup>-1</sup>, consistent with an increase in storms entering the subtropical SPCZ. This could be due to an alleviation of the storm graveyard position bias in coupled models, discussed further in Section 3.4.

The class of convective parameterization scheme (e.g., closure on moisture convergence or buoyancy) has been shown to have an impact on the simulation of tropical variability in climate models (e.g., the MJO; Slingo et al., 1996; Lin et al., 2006). However, no such dependence was found here for the SPCZ.

### *3.3.b Power spectra analyses*

An alternative way to establish how well models are simulating variability on synoptic timescales is through the use of power spectra analysis. A power spectra analysis of TOA OLR is calculated for both coupled (Figure 3.6a) and atmosphere-only (Figure 3.6b) models in the subtropical SPCZ. Consistent with observations and CFSR,

the variability in both sets of models is significant between one and two weeks, with many models showing at least one distinct spectral peak in that range. In the case of the atmosphere-only models, many have too strong a magnitude for synoptic variability compared to CFSR, perhaps at the expense of power at other timescales (such as MJO, see Hung et al. 2013). CNRM-CM5 and GFDL-CM3 show less variability than the other models at synoptic timescales in the atmosphere-only experiment, with the former being notable since it is the only CMIP5 model capable of simulating an eastward-propagating MJO and displaying realistic MJO variability on the 30-70 day timescale (Hung et al. 2013). There is no obvious relationship between the TOA OLR power spectra magnitudes and the previous model groupings.

Figures 3.6c and 3.6d show the results of a similar spectral analysis but using precipitation instead of TOA OLR. However, the correlation between the TRMM and CFSR power spectra is less than the correlation between the NOAA OLR product and CFSR OLR, although this departure could be partly due to the difference in time series length between TRMM and CFSR. Again consistent with precipitation estimates and CFSR, the variability is significant between one and two weeks with at least one distinct peak. Though CFSR has a higher climatological precipitation value in the subtropical SPCZ than TRMM, CFSR precipitation variability has lower magnitude than TRMM. Despite the differences between precipitation estimates and reanalysis and consistent with the precipitation standard deviation results in Section 3.3.a, many coupled and atmosphere-only models are underestimating precipitation variability, particularly at timescales longer than 1 week. HVG models perform notably better than IVG and LVG models at matching TRMM variability magnitudes, though beyond two weeks all models

are underestimating precipitation variability. Among the more interesting results here is INM-CM4, which performs poorly on timescales less than 7 days but then performs better than many LVG models on longer periods.

In summary, the results of spectral analysis are mixed; the variability of TOA OLR in these models, and hence clouds, is too high on synoptic timescales whereas the synoptic variability of precipitation is too low.

### 3.4 Storm graveyard statistics

Both the coupled model and atmosphere-only model precipitation histograms and TOA OLR/precipitation power spectra suggest a potential deficit of storm interactions in the subtropical SPCZ. Low precipitation variability on synoptic timescales could be explained in part by a decreased frequency of synoptic disturbances propagating into the subtropical SPCZ, or by differing characteristics of these disturbances (e.g. lower rainfall rates). Previous work (Widlansky et al. 2011, Matthews 2012) outlined the importance of the “storm graveyard” region in explaining both the diagonal tilt and variability of rainfall in the SPCZ; thus, how the storm graveyard is simulated in CMIP5 models is explored, as errors could have not only a profound impact on both the synoptic variability of the region but also previously highlighted climatological biases (see Figure 3.1).

Figure 3.7 shows the zonal stretching deformation (ZSD, i.e.  $\partial \bar{U} / \partial x$ ) metric previously used to demarcate the boundaries of the storm graveyard, though it has been simplified by showing the zonal mean across 35°S–20°S. The region in which ZSD is negative in the central Pacific denotes the storm graveyard. Clearly, coupled models show a wide range ( $\sim 180^\circ \pm 30^\circ$ ) of western boundaries, whereas atmosphere-only models

have a much more condensed range ( $\sim 180^\circ \pm 10^\circ$ ). The eastern boundaries show less improvement moving from coupled to atmosphere-only; in fact, the MEM shows a consistent eastward bias in the eastern edge of the graveyard consistent with models simulating increased precipitation farther east than climatologically observed. Looking strictly at the MEM for both cases, it is apparent that the coupled model storm graveyards are weaker in magnitude by nearly half and have minimum ZSD values farther east ( $125^\circ\text{W}$ ) than observed ( $135^\circ\text{W}$ ). The atmosphere-only graveyards show a notably reduced bias both in terms of magnitude and position of minimum ZSD, which can also be seen in the difference plots between the two experiments. These improvements are perhaps unsurprising considering regions of negative ZSD are closely tied to atmospheric circulation, which will be more similar to observations when models are forced with climatological SSTs instead of allowing SST errors to perturb the atmospheric circulation.

A two-dimensional view of storm graveyard biases is presented for coupled models in Figure 3.8. In the model ensemble mean, it is again evident that there is an eastward displacement in the graveyard, though a slight northward bias is also apparent. Despite a slight eastward bias in the MEM, there is a large spread in the longitude of the ZSD minimum among models. This is also evident in the larger graveyard structure; IPSL-CM5A-MR has perhaps the largest westward bias, whereas MRI-CGCM3 has a very pronounced eastward bias. The spread in magnitude of ZSD minima is also noteworthy. However, this does not obviously correlate well with the previously-established model variability groupings. Though other than CNRM-CM5 the HVG models simulate graveyard with reasonably strong magnitudes compared to the IVG and

LVG models, IPSL-CM5A-MR (a LVG model) simulates a graveyard qualitatively similar to climatology.

Figure 3.9 is as Figure 3.8, but showing atmosphere-only model results in lieu of coupled models. Much of the model biases in terms of both magnitude and position are alleviated, though the longitudinal spread in ZSD minima is of comparable magnitude. Though it is not obvious if there are any positional differences between HVG and LVG model storm graveyards, there does appear to be a tendency for HVG models to simulate graveyards with stronger magnitudes of ZSD than the LVG models. In particular, MRI-CGCM3 and CMCC-CM, models that both show close-to-observed precipitation variability, have particularly strong ZSD minima – more than 30% stronger in magnitude. The correlation between subtropical SPCZ synoptic precipitation standard deviation and the magnitude of storm graveyard ZSD minimum in the atmosphere-only models is significant at the 5% level based on a two-tailed t-test with 10 degrees of freedom. This suggests that there is a possibility for increased storm interaction in models with stronger graveyards, which would in turn lead to higher precipitation variability.

### **3.5 Composite analysis of synoptic disturbances interacting with the SPCZ**

Because of the variety of storm graveyard solutions among coupled and atmosphere-only models, differences between the models and observational/reanalysis products in the propagation of vorticity anomalies as they enter the SPCZ are explored using composite analysis. Figure 3.10 shows the results of the composite of vorticity anomalies at 250 hPa (see Section 3.2 for further information) using CFSR as well as the MEM results for both coupled and atmosphere-only models. CFSR shows a propagation



of the vorticity anomalies toward the northeast, from approximately 140°W, 35°S on day -2 to 135°W, 30° on day 0. The atmosphere-only and coupled models show similar motion. During the same period, the precipitation anomalies in the eastern SPCZ in all data sources are located along a distinct axis oriented from northwest to southeast, with wet anomalies northeast of the axis and dry anomalies southeast. There is also a wet precipitation anomaly southwest of the dry anomaly in some cases, confirming the path of the wavetrain as northeastward or east-northeastward. During day 1 and day 2, both the vorticity and precipitation anomalies decay. While the vorticity anomalies drift toward the east, the precipitation anomalies drift toward the northwest, with faster motion in CFSR compared to the MEMs. In analysis of individual models (not shown), only a small subset of the coupled (CSIRO-Mk3.6.0, GFDL-CM3, and MPI-ESM-LR/MR) and atmosphere-only (CMCC-CM, MPI-ESM-MR, and NorESM1-M) models show precipitation anomalies that drift toward the northwest with similar speed to CFSR; the others tend to show relatively stationary anomalies as seen in the MEMs. Propagation biases could be due in part to the influence of equatorial Rossby waves in the region, which are not well-simulated in all models (George Kiladis, personal communication); thus, the composite analysis may not be solely picking up interactions between the SPCZ and midlatitude synoptic disturbances. Other than simulating precipitation anomalies without the observed northwestward drift following a storm interaction event, these composite results do not suggest either MEM is substantially biased in interactions between synoptic disturbances and the SPCZ.

To elucidate whether individual models exhibit a zonal bias to the trajectories of vorticity anomalies approaching the SPCZ, a vorticity backtracking algorithm is used to

recover the linear trajectory and speed of individual interactions in reanalysis data compared to coupled and atmosphere-only model output (Figures 3.11 and 3.12, respectively). There is no notable bias in modeled storm trajectory in terms of MEM results, with atmosphere-only and coupled models simulating tracks consistent with CFSR. However, a spread in approach angle of approximately  $\pm 10^\circ$  among individual coupled and atmosphere-only models does exist. There is a correlation between ZSD minimum values and storm approach angle in the atmosphere-only model results (significant at the 5% level), but the correlation sign is inconsistent with the expectation that a stronger graveyard would result in weaker eastward advection and increased equatorward diversion toward the westerly wind duct. Additionally, there is no such significant correlation in the coupled models. Thus, these variations in storm trajectory are not physically meaningful. On the other hand, consistent with a weaker graveyard in models, both the coupled and atmosphere-only MEM speed of the storms is 0.8 m/s and 0.6 m/s faster than CFSR, respectively. However, storm speeds calculated for individual models do not show any strong correlation with the ZSD minimum values (neither significant at the 10% level). No other significant correlations arose with storm trajectory and speed among individual coupled and atmosphere-only models. Thus, if the correlation between mean synoptic precipitation variability and storm graveyard ZSD minima has a physical basis, it is unlikely related to obvious differences in SPCZ-storm interaction among models.

Because of the difference in precipitation anomaly propagation, it is worth examining the development of specific humidity anomalies at lower- and mid-levels throughout the storm interactions. Like Figure 3.10, Figure 3.13 shows the results of the

static composite analysis, but vorticity has been replaced with lower- (850 hPa) and mid- (500 hPa) level specific humidity. In the CFSR results, there is a tendency for the mid-level positive moisture anomalies to appear more prominently leading up to day 0; conversely, the dry anomalies behind the storm are evident at both levels. Also worth noting are the precipitation anomalies in the storm track southwest of the SPCZ, as they are associated primarily with a low-level moisture anomaly. Because the SPCZ environment is already favorable for convection (e.g. warm SSTs, conditional instability), the lower-level is already close to saturation; thus, the main impact that the interacting storm has is encouraging deeper convection, resulting in the mid-level moisture anomaly observed. There is no evidence of a temporal offset between precipitation and moisture leading up to the storm interaction, though there does appear to be a tendency for the moisture anomaly to drift further north than the precipitation anomaly during days 1 and 2.

In terms of the models, both the coupled and atmosphere-only models manifest a mid-level moisture anomaly in the SPCZ, an equivalent barotropic dry anomaly southwest, and a low-level moisture anomaly associated with a separate storm farther southwest. In order to better understand if individual models are showing a similar drift in specific humidity, a representative subset of atmosphere-only models are shown in Figure 3.14. There appear to be four distinct moisture-precipitation relationships in the models. The most similar model to CFSR in terms of the magnitude and propagation of the primary moisture anomaly within the SPCZ is CCSM4, though it does not show a particularly strong secondary moisture anomaly farther southwest. MPI-ESM-MR also performs well, though it shows a more barotropic moisture anomaly in the SPCZ, less

obvious propagation signatures, and a strong barotropic moist anomaly farther southwest. In the case of MRI-CGCM3, results compare with MPI-ESM-MR, though the mid-level moisture anomaly in the SPCZ is more stationary. Finally, INM-CM4 lacks a particularly strong moisture anomaly associated with its precipitation enhancement in the SPCZ and manifests much stronger dry and wet barotropic anomalies toward the southwest. Thus, the lack of motion to both the precipitation and moisture anomalies as seen in the MEM for coupled and atmosphere-only models during and after storm interactions is representative of many, though not all, of the individual model results.

### **3.6 Summary**

Models included in CMIP5 show notable improvements in climatological precipitation simulation when forced with observed sea surface temperatures compared to a fully coupled ocean model; they do not show the same changes in simulated precipitation variance. These models generally underestimate light and heavy precipitation and overestimate moderate precipitation, with this bias increased as precipitation variance decreases. Outgoing longwave radiation variance, in contrast, is overestimated. The storm graveyard in coupled models is generally weaker in magnitude and displaced toward the northeast, but there is a wide range in the central longitude; though the range of longitudes does not decrease much in the atmosphere-only models, the other biases are decreased. Results from both a composite analysis and a storm tracking algorithm reveal that storms approach the SPCZ consistent with theory in CMIP5 models, suggesting that poor convective parameterizations and errors in sea surface temperatures are largely responsible for biases on synoptic timescales.

## **4. Forcing low-level inflow shifts east of the SPCZ**

### **4.1 Introduction**

The Quasi-equilibrium Tropical Circulation Model 2 (QTCM2, Lintner et al. 2012) is an ideal model in which to test questions of causality surrounding changes to low-level inflow on the eastern margin of the SPCZ due to its relatively simplicity compared to a GCM as well as its computational efficiency. Therefore, an assortment of simulations using QTCM2 are shown in this work that should help to clarify the connections between a) low-level and upper-level circulation anomalies east of the SPCZ and b) circulation and moisture anomaly timing. Section 4.2 outlines the model setup and presents a description of each experiment. Section 4.3 explores the suitability of QTCM2 to perform these experiments through an examination of its biases in the South Pacific region in both a default setup as well as one removing the landmasses of Australia and New Zealand. Section 4.4 discusses the results of the circulation anomaly experiments, while Section 4.5 examines moisture anomaly experiments. Finally, conclusions and avenues for future work are presented in Section 4.6.

### **4.2 Data and methodology**

For all experiments, QTCM2 is run at a zonal resolution of 256 grid cells ( $\approx 1.41^\circ$ ) and a meridional resolution of 150 grid cells ( $1^\circ$ , spanning  $75^\circ\text{S}$ - $75^\circ\text{N}$ ); this resolution is identical to the high-resolution runs performed by Lintner et al. (2012) to establish baseline climatology for the model. Ocean temperatures are fixed in these experiments to climatological monthly means obtained from Reynolds et al. (2007). Further analysis of QTCM2 baseline climatology in the South Pacific is performed to

determine its suitability for these experiments. As in previous SPCZ studies (Niznik and Lintner 2013; Niznik et al. in press), the National Center for Environmental Prediction (NCEP) Climate Forecast System Reanalysis (CFSR; Saha et al. 2010) is used as a reasonable proxy for observations in the poorly-observed South Pacific during the 32-year period spanning 1979-2010; specifically, zonal and meridional wind, specific humidity, and precipitation output are considered. Two baseline QTCM2 control experiments with modified convective adjustment timescales (8 hours for both shallow and deep convection) were run for a comparable 33-year period (1 year of model spinup without output followed by 32 years with output) starting in December for validation against CFSR: a default control run with no notable alterations (CON32) and a control run in which the land masses of Australia and New Zealand are removed and replaced with ocean (CON32\_NOAUST). Surface temperatures in these newly added ocean grid cells were unaltered from the default land surface temperatures. CON32\_NOAUST was run to examine how SPCZ biases change in QTCM2 when the overly strong Australian monsoon is suppressed. For the purposes of comparison between CFSR and QTCM2, the output from CFSR and the results of both control runs were regridded to a common  $2.5^{\circ} \times 2.5^{\circ}$  grid. For all comparisons, DJF mean data is shown in lieu of annual mean data due to the increased strength of the SPCZ during austral summer; as a result, the first January, first February, and final December are excluded from CFSR and the final DJF is excluded from the QTCM2 control runs, resulting in a total of 31 austral summers in all three sets of output.

In addition to calculating simple wind, moisture, and precipitation biases across the South Pacific in both CON32 and CON32\_NOAUST, upper-level zonal stretching

deformation (ZSD), i.e.  $\partial \bar{U} / \partial x < 0$ , is calculated and compared with CFSR to gain further insight into how well the storm graveyard is simulated in QTCM2. The composite analysis that Niznik and Lintner (2013) performed is also repeated for QTCM2, although this time using DJF data in lieu of January-only data, in order to confirm that precipitation and moisture in the model respond appropriately to variations in low-level inflow. The composite index in this analysis is the strength of zonal wind at 850 hPa in the box 140°W–120°W, 20°S–10°S with the annual mean removed to avoid biases due to low-frequency variability (e.g. ENSO, though QTCM's fixed SSTs do not allow for such variability). Taking the mean of all events during which the composite index is greater than one positive standard deviation or less than one negative standard deviation from the mean (by definition, 0) creates the weak- and strong-inflow phases, respectively.

In order to simulate weak and strong inflow conditions, instantaneous vorticity anomaly fields in the box 140°W–120°W, 35°S–15°S are imposed using the “vort0” variable in the model, which accounts for barotropic vorticity (and is approximately equal to the vorticity at 440 hPa), and replace values from the initial conditions; Table 4.1 lists the values used for each experiment. The number assigned to each experiment refers to the percentage (e.g. 50 = 50%, etc.) of vorticity anomaly magnitude from the mean compared to the mean weak and strong inflow vorticity values from the analysis of CFSR in Niznik and Lintner (2013). For example, the mean vorticity value in the region where vorticity is imposed is approximately  $0.4 \times 10^{-5} \text{ s}^{-1}$ . Thus, W100 uses the full anomaly from the mean,  $0.6 \times 10^{-5} \text{ s}^{-1}$ , to arrive at  $-0.2 \times 10^{-5} \text{ s}^{-1}$ , the mean vorticity associated with the weak inflow phase in CFSR. Likewise, S150 uses 150% of the full anomaly,  $0.9 \times 10^{-5} \text{ s}^{-1}$ , to arrive at  $1.3 \times 10^{-5} \text{ s}^{-1}$ , a stronger-than-observed case of strong inflow. Because

QTCM2 wind vertical profiles are prescribed, the anomaly is present in varying degrees throughout the free troposphere (similar to observed weak- and strong-inflow events) but not at all present in the boundary layer.

In addition to the vorticity experiments, two moisture experiments are performed in which the characteristic weak- and strong-inflow moisture anomalies along the eastern edge of the SPCZ (excluding the opposite sign anomalies further toward the southwest) are instantaneously imposed using the variable 'q1'; these experiments are named W100Q and S100Q, respectively. The approach is two-tiered, with a weak moisture anomaly imposed in the parallelogram bounded by the points (119°W 12°S, 143°W 12°S, 120°W 38°S, 96°W 38°S), and a stronger moisture anomaly imposed in the parallelogram bounded by the points (122°W 17°S, 134°W 17°S, 119°W 33°S, 107°W 33°S) in W100Q. In S100Q, the moisture anomalies are displaced toward the east by 5° compared to W100Q, consistent with the results of the CFSR and QTCM2 composite analysis results (i.e. the negative moisture anomaly during the strong-inflow phase is displaced toward the east consistent with the adjustments made here). The magnitude of both levels of moisture anomaly for W100Q and S100Q are listed in Table 4.1.

Each experiment was repeated using 20 different initial conditions, each extracted from a control run. The mean of these ensemble runs is used for analysis throughout this work in order to minimize noise in the response. Using the same initial conditions, an equal number of control runs are performed to allow for comparison to the mean state. The default implementation of QTCM2 outputs all variables with no greater a frequency than 1 day; a code modification allows for the hourly output used in this work.



### 4.3 QTCM2 biases

Figure 4.1 shows the DJF climatological wind at 250 hPa, specific humidity at 850 hPa, and precipitation in CFSR, CON32, and CON32\_NOAUST, while Figure 4.2 shows the difference between each control run and CFSR. Before discussing these biases in detail, it is worth noting that QTCM2 values plotted at a particular level are derived from a prescribed vertical profile and are unable to ever match CFSR realistically due to the limited degrees of freedom in QTCM2. As a result, this comparison between a fully 3D coupled reanalysis and QTCM2 needs a reasonable amount of nuance in its interpretation. The ultimate goal of this section is to show QTCM2 produces a reasonable enough climatology, particularly in the vicinity of the eastern margin of the SPCZ, to justify its use in the experiments that follow.

Both CON32 and CON32\_NOAUST suffer from a few notable moisture and precipitation biases. First, precipitation and moisture are too strong along the equator due to an on-equator ITCZ in the model; thus, the strong precipitation biases along and north of the equator in both control runs are indicative of a displaced ITCZ. The SPCZ itself is displaced toward the east due to an anomalous dry zone east of Australia in both control runs. Despite the elimination of the positive precipitation bias over northern Australia in CON32\_NOAUST, there is an enhanced dry anomaly off the coast of Australia compared to CON32. This is perhaps surprising; a natural conclusion to draw from CON32 would be that the dry region is simply a strong region of subsidence tied to the strong Australian monsoon. Since the ITCZ's greatest intensity is northwest of these dry anomalies, another interpretation of this bias is an anomalously strong subsidence zone associated with outflow from the ITCZ (and perhaps both in CON32). Despite some strong moisture and

precipitation biases across the South Pacific, the biases along the SPCZ in both control runs are comparably muted. In fact, CON32\_NOAUST is particularly encouraging with a slight positive bias in precipitation east of the negative anomaly in the region  $130^{\circ}\text{W}$ – $150^{\circ}\text{W}$ ,  $20^{\circ}\text{S}$ – $30^{\circ}\text{S}$ , indicating an eastward-shifted SPCZ. There are certainly caveats in using QTCM2, though for the purposes of examining changes in dry air inflow along the SPCZ, QTCM2 appears reasonable.

There are also notable biases in upper-level wind in both control runs. The Southern Hemisphere storm track is generally too weak from approximately  $45^{\circ}\text{S}$  southward. There is a strong cyclonic anomaly in CON32 south of the anomalous Australian monsoon, which is more muted in CON32\_NOAUST. The eastern equatorial Pacific westerly wind duct, which plays a role in SPCZ-storm interactions (see Matthews 2012), is more of a “calm” duct with very weak winds throughout. The removal of Australia introduces a positive anomaly in upper-level wind between  $20^{\circ}\text{S}$ – $30^{\circ}\text{S}$  from  $120^{\circ}\text{E}$  through about  $180^{\circ}\text{E}$ , where it weakens but persists even through  $120^{\circ}\text{W}$ . However, as is the case for precipitation and moisture, the wind fields are, in a broad sense, realistic enough for the purposes of these experiments.

Figure 4.3 show a comparison between the CFSR regions of negative ZSD, representing the storm graveyard in the Central Pacific in the region  $170^{\circ}\text{W}$ – $120^{\circ}\text{W}$ ,  $15^{\circ}\text{S}$ – $35^{\circ}\text{S}$ , and the negative ZSD in both control runs. Both runs capture the strong region of negative ZSD off the equatorial west coast of South America, but displace the region south of Australia to the northeast; this is perhaps consistent with the equatorward-displaced storm track in QTCM2. While both runs do simulate a region of negative ZSD within the bounds of CFSR’s storm graveyard, the region is weaker in magnitude and

smaller in zonal extent in CON32 while CON32\_NOAUST's region is displaced to the north. In addition, the northward displacement of the storm graveyard in CON32\_NOAUST may help to explain that model's smaller region of precipitation greater than 4 mm/day protruding into the subtropics. The magnitude and positional errors of the storm graveyard in QTCM2 are comparable to those of the CMIP5 models examined in Niznik et al. (in press).

Figure 4.4 shows the results of the composite analysis for CFSR and the QTCM2 control runs. Both CON32 and CON32\_NOAUST do display characteristic circulation, moisture, and precipitation anomalies consistent with CFSR, though the magnitude of the response, particularly in the circulation and precipitation, is muted. Furthermore, the center of the circulation anomalies is displaced  $10^{\circ}$  to  $15^{\circ}$  east of the CFSR location, though consistent with the eastward displacement of the SPCZ in QTCM2. CON32\_NOAUST shows a more zonal tilt to the moisture and precipitation anomalies, though the CFSR tilt appears to be at an angle somewhere between the CON32 and CON32\_NOAUST results. There is a much stronger equatorial signal in both CON32 and CON32\_NOAUST, with decreased equatorial ITCZ precipitation during the weak-inflow phase and vice versa. Overall, while QTCM2 appears less sensitive to changes in low-level inflow than CFSR, it still responds realistically and appears suitable for imposed circulation and moisture experiments.

Having examined the CON32 and CON32\_NOAUST results, it is not particularly straightforward to make a decision on which model implementation is most favorable for the following experiments. However, the limited improvement CON32\_NOAUST shows over CON32 in terms of precipitation biases along the SPCZ and storm graveyard

size/magnitude do not justify the removal of an entire continent from the region. Thus, despite biases in both QTCM2 control runs, the CON32 implementation will be used for the remainder of the experiments. [It should be noted here that some experiments were performed with CON32\_NOAUST and the results were qualitatively similar.]

#### **4.4 Barotropic vorticity experiments**

Two-hour ensemble mean snapshots ending at the indicated hour in each row of 850 hPa circulation, moisture, and precipitation, as well as anomalies from the control runs, are shown in Figure 4.5 for the W100 and S100 experiments. For the W100 experiment, there is a steady increase in precipitation and moisture along the eastern edge of the SPCZ from 12 hours onward, with a maximum precipitation anomaly of about  $+3.5 \text{ mm day}^{-1}$  by 24 hours and a maximum moisture anomaly of  $+1.25 \text{ g kg}^{-1}$ . In contrast, the S100 negative precipitation and moisture anomalies along the eastern edge of the SPCZ are notably weaker and slower to form, with a minimum precipitation anomaly of  $-1.5 \text{ mm day}^{-1}$  and a minimum moisture anomaly of about  $-0.75 \text{ g kg}^{-1}$  by 24 hours. Shifts in the SPCZ's position are subtler in the mean precipitation plots, though a careful examination of the composite region used to generate Figure 4.4, bounded by  $140^{\circ}\text{W}$ – $120^{\circ}\text{W}$ ,  $20^{\circ}\text{S}$ – $10^{\circ}\text{S}$ , shows an expansion of the  $2 \text{ mm day}^{-1}$  contour further east in W100 compared with S100. This response is less linear than observed by Niznik and Lintner (2013), who noted that the weak- and strong-inflow phases manifested similar circulation, moisture, and precipitation responses opposite in sign. However, careful examination of previous CFSR results reveals the magnitude of the maximum weak-inflow moisture anomaly is nearly double the magnitude of the minimum strong-inflow

moisture anomaly. The lack of linearity also holds true for the moisture and precipitation anomalies southwest of those along the eastern edge of the SPCZ; while the minimum moisture and precipitation responses in W100 are  $-0.5 \text{ g kg}^{-1}$  and  $-2.5 \text{ mm day}^{-1}$ , the maximum moisture and precipitation responses in S100 are  $+0.25 \text{ g kg}^{-1}$  and  $+1.5 \text{ mm day}^{-1}$ . The wind anomalies are fast to decay, with an anomalous 850 hPa circulation 2-3  $\text{m s}^{-1}$  in magnitude by 6 hours after initialization decaying to nearly 0 by the end of the first 24 hours.

Figure 4.6 shows more two-hour ensemble mean snapshots, this time with spacings of 24 hours. By 48 hours, both the positive moisture and precipitation anomalies have drifted toward the northeast, but only the precipitation anomaly has decayed. By 72 hours, the moisture anomaly has begun to decay and the signature of an altered storm track appears; this is consistent with anomalous easterlies introduced to the storm track at initialization, slowing the propagation of midlatitude storms compared to the control run. Through 120 hours, the positive moisture and precipitation anomaly drifts toward the southeast and seemingly merges with the northern edge of a midlatitude disturbance. S100 has a similar story, with a decaying negative precipitation anomaly by 48 hours, a decaying negative moisture anomaly by 72 hours, and an altered storm track (this time, anomalous westerlies speeding the propagation of midlatitude storms). It is worth noting that despite the movement of the positive and negative moisture anomalies on the eastern edge of the SPCZ in W100 and S100, respectively, they do persist near their region of initiation for up to five days.

Figure 4.7 shows results from W100 and S100, but now substituting boundary layer mean circulation and moisture in the place of those fields at 850 hPa. By 12 hours

after the initial free troposphere vorticity anomaly in the weak-inflow phase, anomalous boundary layer convergence in the vicinity of the positive precipitation anomaly along the eastern SPCZ is present, though by 18 hours the convergence appears to transform into primarily anomalous moisture advection from the northwest. In the strong-inflow phase, the flow appears weaker, less convergent, and more strictly meridional, with dry air advection from the south along the eastern margin of the SPCZ associated with a negative precipitation anomaly. The moisture anomalies in both cases are muted compared to the free troposphere, indicating reduced advection compared to the free troposphere; this is consistent with the weaker circulation anomalies and therefore weaker moisture advection in the boundary layer. The boundary layer moisture anomalies appear to reach their peak one day after the imposed vorticity anomaly, with a slow decline as in the free troposphere, shown in Figure 4.8. In terms of vertical consistency, the boundary layer and free troposphere anomalies align well, though there is a tendency for the boundary layer anomaly to propagate toward the east more slowly from 72 hours onward.

The moisture and precipitation anomalies may be nonlinear between the weak- and strong-inflow phases, but they are more linear as the magnitude of the vorticity anomalies changes. One example is displayed in Figure 4.9, which is similar to Figure 4.5 but now using data from W150 and S150. Despite a stronger wind anomaly, the first 6 hours are still relatively uneventful in terms of moisture and precipitation response in both W150 and S150, though the anomalous circulation has increased in magnitude to approximately  $5 \text{ m s}^{-1}$ . By 24 hours, however, stronger moisture and precipitation anomalies have formed than those seen in W100 and S100. Maximum moisture and

precipitation anomalies in W150 exceed  $1.5 \text{ g kg}^{-1}$  and  $4 \text{ mm day}^{-1}$ , respectively, while minimum moisture and precipitation anomalies in S150 exceed  $-1 \text{ g kg}^{-1}$  and  $1 \text{ mm day}^{-1}$ . The nonlinearity of the response is once again highlighted, though in S150 the strengthened low-level inflow along the eastern margin of the SPCZ has likely reached a point where close to 0 precipitation falls in the region whereas the weakened low-level inflow in W150 does not have an easily reached analogue (i.e. the upper bound on precipitation associated with anomalous westerly moisture advection is higher than the maximum values in W150).

A time series of mean wind, moisture, and precipitation anomalies throughout all experiments in selected regions is shown in Figure 4.10. For 850 hPa zonal wind, the selection region is simply the composite region from Figure 4.4. For 850 hPa specific humidity and precipitation, the bounding coordinates for the selected region are  $125^{\circ}\text{W}$ – $110^{\circ}\text{W}$ ,  $17.5^{\circ}\text{S}$ – $25^{\circ}\text{S}$ , which were chosen in order to capture the core region of the anomalies along the eastern edge of the SPCZ. It is evident that the wind anomalies peak just before 12 hours for each inflow phase, with a gradual return to the mean toward 48 hours. However, around 48 hours, the anomalies then persist in a weakened state for an additional 48 hours, at which point a very gradual decline toward the climatological value (approximately  $-2.5 \text{ m s}^{-1}$ ) by 192 hours (though the anomalies in both phases are negligible by 108 hours).

Moisture anomalies reach a maximum nearly one day after the wind anomalies around 36 hours, after which each phase shows a persistent anomaly through about 72 hours, at which point a gradual decay toward climatology (approximately  $5.9 \text{ g kg}^{-1}$ ) begins. Precipitation is faster to respond, with the peak response at around 18 hours in

each experiment. There is a much stronger dip in precipitation values around 48 hours in the precipitation field compared to the wind and moisture fields in the weak-inflow experiments, with a gradual increase in precipitation toward 72 hours in phase with the secondary peak of the moisture anomaly. After 96 hours, both sets of experiments converge toward climatology (just under  $2 \text{ mm day}^{-1}$ ).

There are three intriguing findings to note from the time series plots. First, these results show weak- (and to a lesser degree, strong-) inflow anomalies lasting longer than those in CFSR lead-lag composites (shown in Figure 4.11) of Niznik and Lintner (2013). The mean weak- and strong-inflow anomalies persist for at most 3 days after a peak in CFSR, which the QTCM2 results are broadly consistent with despite being artificially imposed. However, a notable moisture anomaly persists for 4-5 days after the peak of an anomalous inflow event in CFSR while QTCM2 anomalies last upwards of one week. In terms of anomaly magnitude, CFSR best matches W50 during the weak-inflow phase, and S50 during the strong-inflow phase. Precipitation anomalies persist for closer to 3 days in CFSR, while the QTCM2 experiments again suggest a longer 5-7 day timeframe. Here, CFSR best matches S150 during the strong-inflow phase, but all of the weak-inflow experiments have too low a precipitation increase (W150 is about  $0.5 \text{ mm day}^{-1}$  to weak in its response). This is perhaps not surprising considering the observed weak-inflow events experience an extra 2-3 days of anomalous moisture advection prior to their peak compared to the instantaneous vorticity experiments.

Second, there is a tiered response to the initial vorticity anomaly. That is, instead of a simple decay toward the mean after wind, moisture, and precipitation anomalies reach their greatest magnitude, there is a tiered structure to the response, with multiple



plateaus of minimal return to the mean (e.g. zonal wind in the weak-inflow events levels off at 24 hours, then oscillates between 48 and 60 hours, and then levels again from 60 through 96 hours). This could be attributable to nonlinearities in the response of each field. The ensemble mean of the control experiments did have a non-negligible signal throughout the 10-day duration, though the linear contribution of this signal has been removed in the calculation of anomalous fields. An examination of the ensemble mean of the control runs suggests that more often than not synoptic waves were present southeast, south, and southwest of the SPCZ, and their passing by the SPCZ could cause some of the variability. QTCM2 does appear to favor synoptic waves in those three positions, as evidenced by the broad  $2 \text{ mm day}^{-1}$  contour in the climatology shown in Figure 4.1. However, it is difficult to tell if the underlying signal shows the same sign in both the weak- and strong-inflow experiment; thus, further work is needed to clarify if there is any physical meaning to the variability imposed on top of the overall trend.

Finally, the relatively even spacing between each experiment's moisture anomaly time series points to a relatively linear response to linearly increasing vorticity anomalies. This is inconsistent with the previously discussed less linear response of moisture anomaly extrema. Part of this inconsistency can be resolved by considering the potential noise in the maximum signal compared to the smoother areal average shown in Figure 4.10. The linearity is not perfect; for example, the peak moisture anomaly in S150 is of about  $-1.2 \text{ g kg}^{-1}$  while it is  $-0.7 \text{ g kg}^{-1}$  in S75, not a precise doubling. However, it is more difficult to find deviations from linearity in the weak-inflow experiments; the maximum moisture anomaly in W150 is double W75 and triple W50. Overall, it is reasonable to conclude the response to changing low-level inflow on the eastern flank of the SPCZ,

especially during the weak-inflow phase, is more linear than not, though there are (unknown) points of saturation where further increases or decreases to low-level inflow should yield decreasing (and eventually negligible) moisture returns.

#### 4.5 Barotropic moisture experiments

Now that it is clear that QTCM2 exhibits a similar yet nonlinear response to imposed barotropic vorticity along the eastern edge of the SPCZ compared to CFSR, it is worth investigating the opposite relationship. That is, since changes to inflow along the eastern margin of the SPCZ clearly alter the moisture and precipitation fields in the immediate vicinity, it is likely that imposed moisture may lead to a characteristic circulation response. If not, or if the anomalies are much weaker, this lends credence to the hypothesis that circulation is the most important factor in instigating an SPCZ precipitation shift.

Figure 4.12 shows the results of W100Q and S100Q in a manner similar to Figure 4.5 for W100 and S100. After the initial moisture anomalies are imposed, they gradually decay throughout the first 24 hours and are essentially negligible at 48 hours (not shown). There is minimal propagation (or even shearing) of these anomalies throughout the first 24 hours. The precipitation anomalies are more or less collocated with the moisture anomalies and decay in a similar manner, though there does appear to be a northwestward propagation of the maximum precipitation anomaly toward the SPCZ core in the W100Q and no propagation in S100Q. Despite a substantial increase in moisture, the circulation response is very weak; the magnitude of the induced circulation is less than  $1 \text{ m s}^{-1}$ , seen more easily in the time evolution of these anomalies in Figure 4.13.

W100Q and S100Q show a peak circulation response around 36 hours, with the magnitude of the anomaly in W100Q approaching  $0.5 \text{ m s}^{-1}$  and S100Q approaching  $-0.25 \text{ m s}^{-1}$ , consistent with its weaker moisture anomaly. Afterwards, the anomaly gradually returns to climatological values after one week. The initial moisture anomalies decay at a rate relative to their initial magnitude, with each approaching climatology around one week later similar to the circulation response. At least part of the faster decay of the moisture anomaly in W100Q is attributable to the extra moisture being converted to precipitation, which declines more sharply than moisture over the first 24 hours at which point it transitions to a much slower decline. In these experiments, which use the same initial conditions, there are few if any signatures of the tiered decline of the anomalies seen in the Wy and Sy experiments, suggesting it may not be artificial.

#### 4.6 Summary

QTCM2, despite its notable climatological biases, is capable of simulating shifts in the SPCZ associated with synoptic variability in low-level inflow on its eastern flank. Imposing anomalous vorticity and moisture fields in a variety of initial conditions, the ensemble mean response suggests that moisture and precipitation anomalies are reproduced with fidelity during imposed weak- and strong-inflow conditions, but circulation anomalies are too weak in magnitude when moisture is imposed. This suggests that the weak- and strong-inflow phases are initiated primarily via dynamical forcing. Additionally, the precipitation and moisture anomalies peak 18 and 36 hours, respectively, after the initial inflow conditions are imposed. The anomalies scale linearly with increased or decreased dry air inflow, and all fields show a tiered decline toward

their climatological mean values. Compared to CFSR, the QTCM weak- and strong-inflow events persist longer, but require much stronger changes to inflow than observations and reanalyses to produce the same precipitation response.

## 5. Summary, conclusions, and future research directions

### 5.1 SPCZ response to varying low-level inflow

As in LN08, composite analysis of SPCZ-region wind, moisture, and precipitation data in both reanalyses and CMIP5 model output points to robust relationships between high-frequency low-level (trade wind) inflow and tropospheric moisture and precipitation fluctuations. One caveat, however, is the number of differences between R1 and CFSR; CFSR is a better reference for the region than R1 until an appropriate observational dataset of equal length is available at the daily time scale. The confirmation that CMIP5 models are able to reproduce the observed relationship between these variables, especially considering the diversity of climatological SPCZs across the models, suggests that biases in SPCZ simulation are not due to poor representation of this particular synoptic-scale response. However, key differences exist between the reanalysis products, specifically CFSR, and the CMIP5 models. In particular, the precipitation response is more complex in the CMIP5 models; while some models show a precipitation shift toward the east in the weak-inflow phase, others simulate an expansion of precipitation toward the southeast with little movement otherwise. In some models with overly zonal SPCZs, this expansion to the southeast gives the appearance of a more realistic SPCZ.

In terms of the vertical structure, the observed circulation and moisture anomalies in the vicinity of the compositing region manifest equivalent barotropic structure. This suggests that the influence of low-level inflow is not confined simply to the boundary layer but rather extends over a deep layer. In addition, the positive moisture anomalies in both CFSR and the CMIP5 model ensemble mean (MEM) above 850 hPa are stronger and, at 500 hPa in particular, may even lead the 850-hPa anomalies by 1 or 2 days. In

comparison, the negative anomaly appears to be more strongly confined to the lower levels. Interpretation of these results would benefit from a better understanding of the processes that contribute to vertical moisture distribution (e.g., Holloway and Neelin 2009; Lintner et al. 2011).

The lead–lag analysis applied to CFSR as well as the CMIP5 models, which is summarized schematically in Figure 5.1, suggests two prominent antecedent circulation features for weak inflow and strong inflow, namely a cyclone (anticyclone) south of Australia and an anticyclone (cyclone) in the south-central Pacific, respectively. Aloft, the strength and location of the SPJ south of Australia, the STJ streak in the central Pacific, and the westerly duct in the equatorial eastern Pacific vary with the composite index at a lead time of 3–5 days. These features together with an analysis of SLP anomalies suggest increased interaction between the SPCZ and synoptic disturbances during the weak-inflow phase. Further work is needed to understand the different mechanisms of low- and upper-level forcings at synoptic time scales, especially since the CMIP5 models differ drastically from CFSR particularly at 250hPa in this analysis.

Another direction for future work is to gain an understanding of how these anomalies may change owing to the effects of anthropogenic warming in the region. The results of a preliminary lead–lag analysis applied to data from the CMIP5 RCP8.5 scenario are shown in Figure 5.2, with the caveat that any changes shown are likely biased due to errors in precipitation and SST climatology across the South Pacific. One key difference in both weak-inflow and strong-inflow phases is the increased magnitude of the positive moisture anomalies. In addition, the zonal extent of the precipitation shift during the weak-inflow phase in the RCP8.5 MEM is approximately  $5^{\circ}$  longitude farther

than that in the historical MEM (135°W–115°W versus 125°W–110°W) despite a projected future westward displacement of the mean January SPCZ position by 10°; in contrast, the strong-inflow phase shows even less deviation from its climatological mean than in the historical results. This result is qualitatively consistent with expectations based on warming-induced moistening of the troposphere over the South Pacific. That is, during events of increased low-level inflow, the climatologically moister environment is less susceptible to dry air inflow shutting off deep convection; conversely, less moistening is needed during relaxed easterly events to trigger convection east of the climatological SPCZ position. Nearly all of the SLP anomalies in the RCP8.5 scenario are weakened (not shown), with the only possible exception being that associated with the weak-inflow phase anomalous cyclone south of the composite region. These weakened dynamic anomalies are consistent with a weaker Walker circulation and the resultant weaker SLP gradient across the Pacific (e.g., Vecchi and Soden 2007). An exploration of these potential changes in response using a future climate scenario with ocean SST bias adjustments akin to those discussed in Widlansky et al. (2013) would aid in verification and is planned. The changes outlined here highlight the importance of focusing on future changes beyond simple shifts in the mean state in the SPCZ region.

Though synoptic changes to low-level inflow east of the SPCZ do not appear to be a significant source of climatological SPCZ simulation biases, this does not exclude the possibility that other synoptic-scale processes, such as interactions between synoptic disturbances and the SPCZ, are poorly represented and contribute to biases. Though the results of Chapter 3 suggest synoptic disturbances are generally well-simulated in CMIP5 models, the results of forcing a GCM or regional model with a correctly positioned

region of negative zonal stretching deformation, as well as with a more realistic storm track, would be a significant step forward in terms of understanding the magnitude of influence these factors have on an accurately simulated SPCZ both at synoptic and seasonal time scales.

## **5.2 Synoptic variability along the SPCZ in CMIP5 models**

The ability of current-generation coupled climate and atmosphere-only models to simulate synoptic timescale variability in the SPCZ has been evaluated. The standard deviation of precipitation across the South Pacific varies substantially between models, particularly within the  $4 \text{ mm day}^{-1}$  contour of the climatological SPCZ. Extreme examples among atmosphere-only models include INM-CM4, which shows weak variability ( $4\text{--}6 \text{ mm day}^{-1}$ ), and MRI-CGCM3, which shows very strong variability ( $12\text{--}16 \text{ mm day}^{-1}$ ). Observed values from TRMM and reanalysis values from CFSR are near the model upper extreme ( $10\text{--}14 \text{ mm day}^{-1}$ ). The ratio of each model's precipitation standard deviation to TRMM does not change noticeably when limiting standard deviation to the synoptic timescale (defined here as less than 14 days).

The tendency for low precipitation variability in the SPCZ is consistent with CMIP5 model biases in precipitation shown previously (Sillmann et al. 2013); i.e., the coupled models tend to overestimate moderate precipitation at the expense of both light and heavy precipitation, which is evident in the precipitation histograms. However, the overestimate in moderate precipitation is only partially eliminated in the atmosphere-only models, suggesting that biases in simulated SST in the South Pacific are not the sole reason for this type of error. Model precipitation power spectra are consistent with the



histogram results, though OLR appears to vary too strongly. These results point toward problems in model cloud and precipitation parameterizations that still need to be addressed.

Prior work highlighted the importance of storm interactions in generating SPCZ convection (Widlansky et al. 2011; Matthews 2012); thus, it is plausible that inter-model differences in the frequency and characteristics of storm interactions in the subtropical SPCZ may account for differences in model precipitation variability. As a first attempt at examining these differences, an analysis of the storm graveyard in both coupled and atmosphere-only models was performed. Whereas considerable spread is evident across both the coupled and atmosphere-only models in terms of the magnitude and position of the storm graveyard, the latter show more consistency in the location of the western boundary of the feature. Whereas the coupled MEM graveyard is both weaker and further northeast than observed, both of these biases are alleviated in the atmosphere-only MEM. A significant correlation between graveyard intensity and precipitation variability is identified in the atmosphere-only models, consistent with the expectation that increased storm interactions lead to simulation of greater precipitation variability.

The static composite analysis based on upper-level vorticity within the storm graveyard region suggests no obvious bias in the storm trajectories as they approach the SPCZ. However, the models do not show as strong a propagation of precipitation anomalies toward the northwest into the tropical SPCZ following the interaction. To probe the storm interactions further, a vorticity backtracking algorithm was employed. Results of the backtracking indicate no notable bias in the simulated storm trajectories but a positive propagation speed bias stronger in the coupled models. Although these

results are consistent with expectations considering a weaker simulated storm graveyard, the correlation between graveyard intensity and either the approach angle or propagation speed in the individual models is not strong. Finally, lower- and mid-level moisture anomalies during the period of the static composite analysis were considered, as they may reveal more information about the differences in behavior between observed and modeled precipitation anomaly drift. Reanalysis moisture anomalies within the SPCZ are stronger at the mid-levels, consistent with storm interactions triggering deeper convection; in the models, this is generally true, but there is a greater tendency for lower-level anomalies as well. As with the precipitation anomalies, these moisture anomalies tend to be more stationary in the models than in CFSR. There is broad agreement on a barotropic dry anomaly southwest of the SPCZ during the interaction, consistent with the observed wavetrain pattern, and more limited agreement on a low-level secondary anomaly further west. The results show no evidence of a temporal lag between moisture increases and precipitation onset on the daily timescale.

Overall, current-generation coupled and atmosphere-only models show significant biases in precipitation variability on synoptic timescales, though it remains unclear how strong a role differences in storm interactions play in generating these biases. Because results of the composite analysis were relatively consistent (i.e., it was not a question of if storms interacted in an individual model, but how), it is plausible that differences in model parameterizations (specifically convective parameterizations), may explain the differences in precipitation variability, as suggested in Section 3. It is also worth noting that recent work by Li et al. (2014) suggests that the exclusion of the radiative effects of snow within clouds in CMIP3 and CMIP5 models leads to a positive zonal wind bias in

the vicinity of the storm graveyard; this model error is consistent with the northeastward bias in the position of the ZSD minimum of the coupled MEM as well as the positive rainfall bias on the northern side of the storm graveyard and warrants more study of the dynamic and thermodynamic properties of the subtropical SPCZ. As a starting point, a process-based examination of the differences in both dynamical and thermodynamical characteristics of the synoptic disturbances among models, and how they compare to reanalysis products, is planned; previous process-based diagnostics have proven to be critically important (e.g. Widlansky et al. 2011, Matthews 2012, van der Waal et al. 2015).

Given the significance of the SPCZ as a locus of extratropical-tropical interaction, field campaigns that could improve understanding of the dynamic and thermodynamic environment in which these interactions take place are warranted. A characterization of the vertical structure of circulation and moisture over the course of interaction events would be especially useful. Furthermore, campaigns could include an assessment of trace constituents like CO<sub>2</sub> or anthropogenic constituents, since the SPCZ appears to provide a preferential pathway along which transport to high latitudes occurs. For future model improvements, the following checklist of parameters which must be well-simulated in a model to improve the representation of the SPCZ is provided: a) correct SST gradients across the South Pacific, b) an accumulation zone for synoptic waves, and c) an eastern boundary between moist convection and dry subsidence. Modeling studies that allow for careful perturbation of any combination of these parameters would be useful to elucidate SPCZ sensitivity.

Considering that the models simulate storm interactions with some consistency leads us to posit the following regarding SPCZ simulation in CMIP5; namely, the simulated position of the subtropical portion of the SPCZ is less biased than the equatorial and tropical portions, which are strongly tied to the influence of erroneous SSTs in the equatorial region. Careful examination of the axis of maximum precipitation throughout the SPCZ in TRMM suggests an increased tilt of the subtropical SPCZ relative to the tropical SPCZ, consistent with the recent statistical work of Haffke and Magnusdottir (2013). In some coupled models (e.g. HadGEM2-CC) the change in tilt between the western and eastern SPCZ is drastic, but this bias is largely because the western, more tropical portion of the SPCZ is overly zonal. As a result, it is perhaps necessary to treat the equatorial/tropical SPCZ and subtropical SPCZ as separate features when undertaking multi-model analyses of SPCZ bias.

Another direction for future work is the effect that a well-simulated MJO has on the synoptic variability of the SPCZ. Although given that the MJO is simulated with varying success in current-generation models, it may not yet be feasible to examine this linkage. Future studies of the simulated SPCZ should nonetheless consider the MJO and associated biases in synoptic precipitation variability, though such interactions are likely focused in the tropics with only remote impacts on precipitation in the diagonal region.

### **5.3 Forcing low-level inflow shifts east of the SPCZ**

Despite climatological biases including an ITCZ along the equator, an overly strong Australian monsoon, a storm track too far north, a weaker storm graveyard, and a thinner SPCZ displaced toward the northeast, QTCM2 is capable of simulating a

reasonable response to synoptically varying low-level inflow along the SPCZ's eastern flank. In the future, these experiments should be repeated in an improved QTCM2 model with some or all of these biases alleviated. It is possible that the limited degrees of freedom a vertical profile allows for are the primary cause of biases; if this is the case, perhaps the results here are the best QTCM2 can simulate. However, in addition to removing Australia, additional changes to the model were tested, including changes to its convective adjustment time scales, to optimize the climatology of the South Pacific and showed limited success. Further testing of model parameters may yield an improved representation of the circulation, moisture, and precipitation fields in the South Pacific that would in turn increase confidence in the results of the series of experiments presented here.

When an instantaneous vorticity perturbation is imposed in the free troposphere consistent with the weak- and strong-inflow phases, QTCM2 simulates reasonable moisture and precipitation responses in response. The maximum precipitation response is simulated approximately 18 hours after the imposed inflow, while the maximum moisture response is simulated approximately 18 hours later at 36 hours after the imposed inflow. These results are broadly consistent with previous results examining weak- and strong-inflow in CFSR, although those are limited to daily averages compared to the hourly output of QTCM2. Additionally, the QTCM2 moisture and precipitation responses persist longer than the CFSR results. Part of this may simply be due to QTCM2 taking a much longer time to completely dissipate the initial circulation perturbation leading to weak moisture and precipitation anomalies persisting. Despite initial indications that the local extrema of moisture and precipitation anomalies did not scale linearly, coarser areal

means suggest there is a primarily linear relationship between altered low-level inflow and associated changes to moisture and precipitation anomalies.

While the precipitation response to instantaneously imposed specific humidity anomalies is consistent with the composite analysis results, the circulation response is much weaker (less than  $0.5 \text{ m s}^{-1}$ ) than observed. As a result, a reasonable hypothesis based on these experiments is that the weak- and strong-inflow events are primarily forced dynamically, with changes to circulation preceding changes to precipitation and moisture. The consistency between CFSR and QTCM2 lends support to this hypothesis. However, the vertical profiles used in QTCM2 preclude an exploration of whether upper-level or lower-level dynamics are more important in creating weak- and strong-inflow conditions. Repeating these experiments in a more complex model that resolves multiple vertical levels is warranted to explore the vertical circulation and moisture relationships in each of these phases.

Tables

Modeling Group	Model Name	Lon. (°)	Lat. (°)
Beijing Climate Center, China Meteorological Administration	BCC-CSM1.1 <sup>0</sup>	2.81	2.81
College of Global Change and Earth System Science, Beijing Normal University	BNU-ESM <sup>0</sup>	2.81	2.81
Canadian Centre for Climate Modelling and Analysis	CanESM2 <sup>0</sup>	2.81	2.81
	CCSM4 (r6)	1.25	0.94
Centro Euro-Mediterraneo per I Cambiamenti Climatici	CMCC-CESM <sup>0</sup>	3.75	3.75
	CMCC-CM	0.75	0.75
	CMCC-CMS	1.88	1.88
Centre National de Recherches Meteorologiques / Centre Europeen de Recherche et Formation Avancees en Calcul Scientifique	CNRM-CM5	1.41	1.41
Commonwealth Scientific and Industrial Research Organization in collaboration with Queensland Climate Change Centre of Excellence	CSIRO-Mk3.6.0	1.88	1.88
LASG, Institute of Atmospheric Physics, Chinese Academy of Sciences and CESS, Tsinghua University	FGOALS-g2 (r3) <sup>0</sup>	2.81	3.00
LASG, Institute of Atmospheric Physics, Chinese Academy of Sciences	FGOALS-s2	2.81	1.67
NOAA Geophysical Fluid Dynamics Laboratory	GFDL-CM3	2.50	2.00
	GFDL-ESM2G	2.50	2.00
	GFDL-ESM2M	2.50	2.00
Met Office Hadley Centre	HadGEM2-CC	1.88	1.25
Institute for Numerical Mathematics	INM-CM4	2.00	1.50
Institut Pierre-Simon Laplace	IPSL-CM5A-LR <sup>0</sup>	3.75	1.88
	IPSL-CM5A-MR	2.50	1.26
Atmosphere and Ocean Research Institute (The University of Tokyo), National Institute for Environmental Studies, and Japan Agency for Marine-Earth Science and Technology	MIROC4h <sup>01</sup>	0.56	0.56
	MIROC5	1.41	1.41
Japan Agency for Marine-Earth Science and Technology, Atmosphere and Ocean Research Institute (The University of Tokyo), and National Institute for Environmental Studies	MIROC-ESM-CHEM <sup>0</sup>	2.81	2.81
	MIROC-ESM <sup>0</sup>	2.81	2.81
Max Planck Institute for Meteorology	MPI-ESM-LR	1.88	1.88

	MPI-ESM-MR	1.88	1.88
Meteorological Research Institute	MRI-CGCM3	1.13	1.13
Norwegian Climate Centre	NorESM1-M	2.50	1.88

**Table 2.1.** CMIP5 models used in Chapter 2 of this dissertation. All models had daily data available from CMIP5 historical experiment runs and are used in the contemporary period (1960-1999) analysis. Those models marked with 0 are not used in the future period (2060-2100) analysis; those unmarked are members of the model subset. Except for FGOALS-g2 and CCSM4 (for which the third and sixth ensemble members, respectively, were used due to availability), the first ensemble member of the historical and RCP8.5 experiment was chosen. All models were regridded to 2.5° in both latitude and longitude using area averaging (if in subset) or linear interpolation (if not in subset) for purposes of comparison and the calculation of a model ensemble mean. (Note: MIROC4h lacked RCP8.5 model output and was excluded from the subset despite being regridded using area averaging.) Longitude and latitude columns (Lon. And Lat., respectively) list the resolution of the model output available from PCMDI's CMIP5 database. Further information can be found at [http://cmip-pcmdi.llnl.gov/cmip5/docs/CMIP5\\_modeling\\_groups.pdf](http://cmip-pcmdi.llnl.gov/cmip5/docs/CMIP5_modeling_groups.pdf)



Modeling Group	CMIP5 Model Name	Lon. (°)	Lat. (°)
National Center for Atmospheric Research (NCAR)	CCSM4 (r6)	1.25	0.94
Centro Euro-Mediterraneo per I Cambiamenti Climatici (CMCC)	CMCC-CM	0.75	0.75
Centre National de Recherches Meteorologiques / Centre Europeen de Recherche et Formation Avancees en Calcul Scientifique	CNRM-CM5	1.41	1.41
Commonwealth Scientific and Industrial Research Organization in collaboration with Queensland Climate Change Centre of Excellence	CSIRO-Mk3.6.0	1.88	1.88
NOAA Geophysical Fluid Dynamics Laboratory	GFDL-CM3	2.50	2.00
Met Office Hadley Centre	HadGEM2-CC	1.88	1.25
Institute for Numerical Mathematics	INM-CM4	2.00	1.50
Institute Pierre-Simon Laplace (IPSL)	IPSL-CM5A-MR	2.50	1.26
Max Planck Institute for Meteorology	MPI-ESM-LR	1.88	1.88
	MPI-ESM-MR	1.88	1.88
Meteorological Research Institute	MRI-CGCM3	1.13	1.13
Norwegian Climate Centre	NorESM1-M	2.50	1.88

**Table 3.1.** CMIP5 models used in Chapter 3. Longitude and latitude columns (Lon. And Lat., respectively) list the resolution of the model output available from PCMDI's CMIP5 database. Further information can be found at [http://cmip-pcmdi.llnl.gov/cmip5/docs/CMIP5\\_modeling\\_groups.pdf](http://cmip-pcmdi.llnl.gov/cmip5/docs/CMIP5_modeling_groups.pdf) (Note: HadGEM2-CC is called HadGEM2-A in the AMIP output. For consistency, we will refer to the model as HadGEM2-CC for both the historical and AMIP experiments.)

<b>Dataset</b>			
TRMM	4.11	-	-
CMAP	5.00	-	-
CFSR	5.27	-	-
	<b>Coupled Models</b>	<b>Atmosphere-Only Models</b>	<b>Difference</b>
CCSM4	3.74	3.43	-0.31
CMCC-CM	<b>3.28</b>	4.72	1.44
CNRM-CM5	3.79	4.37	0.58
CSIRO-Mk3.6.0	3.68	3.98	0.30
GFDL-CM3	3.90	3.99	0.09
HadGEM2-CC	<b>4.47</b>	<b>4.90</b>	0.43
INM-CM4	4.30	<b>5.21</b>	<b>0.91</b>
IPSL-CM5A-MR	3.85	4.21	0.36
MPI-ESM-LR	3.98	3.97	-0.01
MPI-ESM-MR	3.93	4.03	0.10
MRI-CGCM3	<b>2.55</b>	<b>5.98</b>	<b>3.43</b>
NorESM1-M	3.45	3.96	0.45
Median of Models	3.82	4.12	0.30
St. Dev. of Models	0.50	0.70	0.20

**Table 3.2.** DJF climatological precipitation ( $\text{mm day}^{-1}$ ) over the subtropical SPCZ region ( $135^{\circ}\text{W}$ – $165^{\circ}\text{W}$ ,  $20^{\circ}\text{S}$ – $35^{\circ}\text{S}$ ). Models with mean precipitation greater than 1 standard deviation from the median of models are shown in bold.

Dataset	(a)		(b)		(c)		
	$\sigma$ Ratio	$\sigma$ Ratio (Synoptic)	PUP 1 PC	PUP 1 PC (Synoptic)	HVG	IVG	LVG
<b>CFSR</b>	1.023	0.9824	-	-			
CCSM4	0.706	0.674	0.326	0.078			X
CMCC-CM	<b>1.164</b>	<b>1.161</b>	<b>-1.343</b>	<b>-1.275</b>	X		
CNRM-CM5	<b>1.182</b>	<b>1.177</b>	<b>-0.746</b>	<b>-1.056</b>	X		
CSIRO-Mk3.6.0	0.658	0.618	1.066	1.013			X
GFDL-CM3	<b>0.854</b>	<b>0.840</b>	0.753	0.644		X	
HadGEM2-CC	<b>1.045</b>	<b>1.027</b>	<b>-0.350</b>	<b>-0.171</b>	X		
INM-CM4	0.754	0.659	1.410	1.558			X
IPSL-CM5A-MR	0.777	0.762	1.145	1.058			X
MPI-ESM-LR	<b>0.843</b>	0.794	<b>-0.629</b>	<b>-0.319</b>		X	
MPI-ESM-MR	<b>0.868</b>	<b>0.818</b>	<b>-0.792</b>	<b>-0.441</b>	X		
MRI-CGCM3	<b>1.340</b>	<b>1.334</b>	<b>-1.651</b>	<b>-1.838</b>	X		
NorESM1-M	0.618	0.562	0.810	0.749			X

**Table 3.3.** Grouping of models based on two criteria for proper simulation of precipitation variability using both the full precipitation record as well as a reconstructed synoptic precipitation signal. a) The ratio of model precipitation standard deviation ( $\sigma$ ) to TRMM precipitation standard deviation in the subtropical SPCZ (135°W–165°W, 20°S–35°S). Ratios that exceed the threshold value of 0.8 are shown in bold. b) The principal component of the first principal uncertainty pattern (PUP) for model precipitation standard deviation. Negative PUP values are shown in bold. (c) Models that meet all criteria ( $\sigma$  ratios  $> 0.8$  and PC  $< 0$ ) belong to the high-variability group (HVG); models that meet none belong to the low-variability group (LVG); the remaining models belong to the intermediate-variability group (IVG). Meeting any individual criterion for inclusion in the HVG group denoted by boldface.

Experiment Name	Duration (in days)	Anomaly Field	Anomaly Variable	Anomaly Location	Anomaly Magnitude	Anomaly Duration
CON32	11880	-	-	-	-	-
CON32_NOAUST	11880	Land Type	stype	111°E–180°E, 48°S–10°S	stype = 0 (ocean)	Permanent
Wy	10	Barotropic vorticity	vort0	140°W–120°W, 35°S–15°S	y = 50; 0.10 x 10 <sup>-5</sup> s <sup>-1</sup> y = 75; -0.05 x 10 <sup>-5</sup> s <sup>-1</sup> y = 100; -0.20 x 10 <sup>-5</sup> s <sup>-1</sup> y = 125; -0.35 x 10 <sup>-5</sup> s <sup>-1</sup> y = 150; -0.50 x 10 <sup>-5</sup> s <sup>-1</sup>	120 s (1 timestep)
Sy	10	Barotropic vorticity	vort0	140°W–120°W, 35°S–15°S	y = 50; 0.70 x 10 <sup>-5</sup> s <sup>-1</sup> y = 75; 0.85 x 10 <sup>-5</sup> s <sup>-1</sup> y = 100; 1.00 x 10 <sup>-5</sup> s <sup>-1</sup> y = 125; 1.15 x 10 <sup>-5</sup> s <sup>-1</sup> y = 150; 1.30 x 10 <sup>-5</sup> s <sup>-1</sup>	120 s (1 timestep)
W100Q	10	Free troposphere specific humidity	q1	Complex parallelogram (see Chapter 4.2)	Outer anomaly: 0.6 g kg <sup>-1</sup> Inner anomaly: 1.2 g kg <sup>-1</sup>	120 s (1 timestep)
S100Q	10	Free troposphere specific humidity	q1	Complex parallelogram (see Chapter 4.2)	Outer anomaly: 0.3 g kg <sup>-1</sup> Inner anomaly: 0.6 g kg <sup>-1</sup>	120 s (1 timestep)

**Table 4.1.** List of experiments performed. Similar groups of experiments are grouped together, using a “y” to denote the part of the name that changes among members of that group. Unless individual values are noted for different y’s, all experiments in the same group maintain the same value for all experiments (e.g. everything except anomaly magnitude is the same in the Wy group of experiments).

## Figures

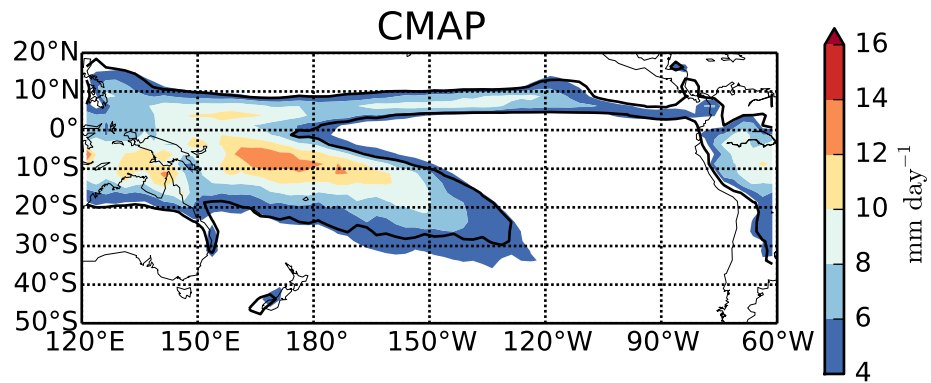


**Figure 1.1.** Climatological DJF precipitation (shading, mm day<sup>-1</sup>) over the Pacific for the CPC Merged Analysis of Precipitation (CMAP), with the Tropical Rainfall Measuring Mission (TRMM) 4 mm day<sup>-1</sup> contour (in black) included for reference.

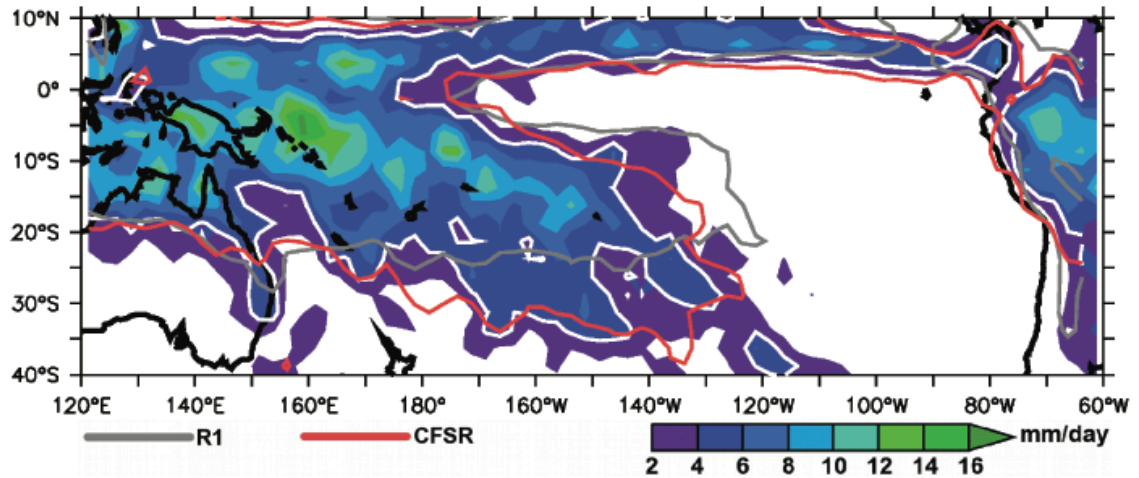


**Figure 2.1.** January precipitation climatology in the SPCZ region, 1998-2010, for three products: a) TRMM 3B42 precipitation estimates (shading) and 4 mm/day contour (in white), b) R1 precipitation 4 mm/day contour (in grey), c) CFSR precipitation 4 mm/day contour (in pink).

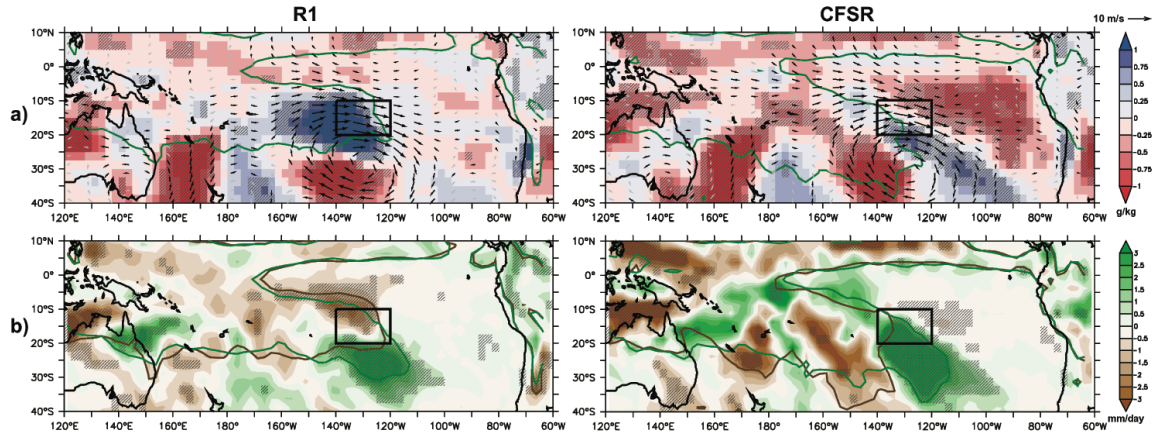


**Figure 2.2.** Composite analysis applied to January daily averages. (a) Composite differences (weak-inflow minus strong-inflow) of R1 (left) and CFSR (right) 850 hPa winds (vectors, in m/s) and specific humidity (shading, in g/kg) for a composite index of zonal wind at 850 hPa averaged over 140°W-120°W and 20°S-10°S. Significance for wind and moisture (at the 99<sup>th</sup> percentile) is denoted by black vector color and dark grey striping, respectively. Included for reference is the January SPCZ climatology (green contour, 4 mm/day) as well as the region in which the composite index was calculated (black box). (b) Composite difference of R1 (left) and CFSR (right) precipitation (shading, in mm/day) and the weak-inflow and strong-inflow phase 4 mm/day contours (green and brown lines, respectively). Significance for precipitation (at the 99<sup>th</sup> percentile) is denoted by dark grey striping. Included for reference is the region in which the composite index was calculated (black box).

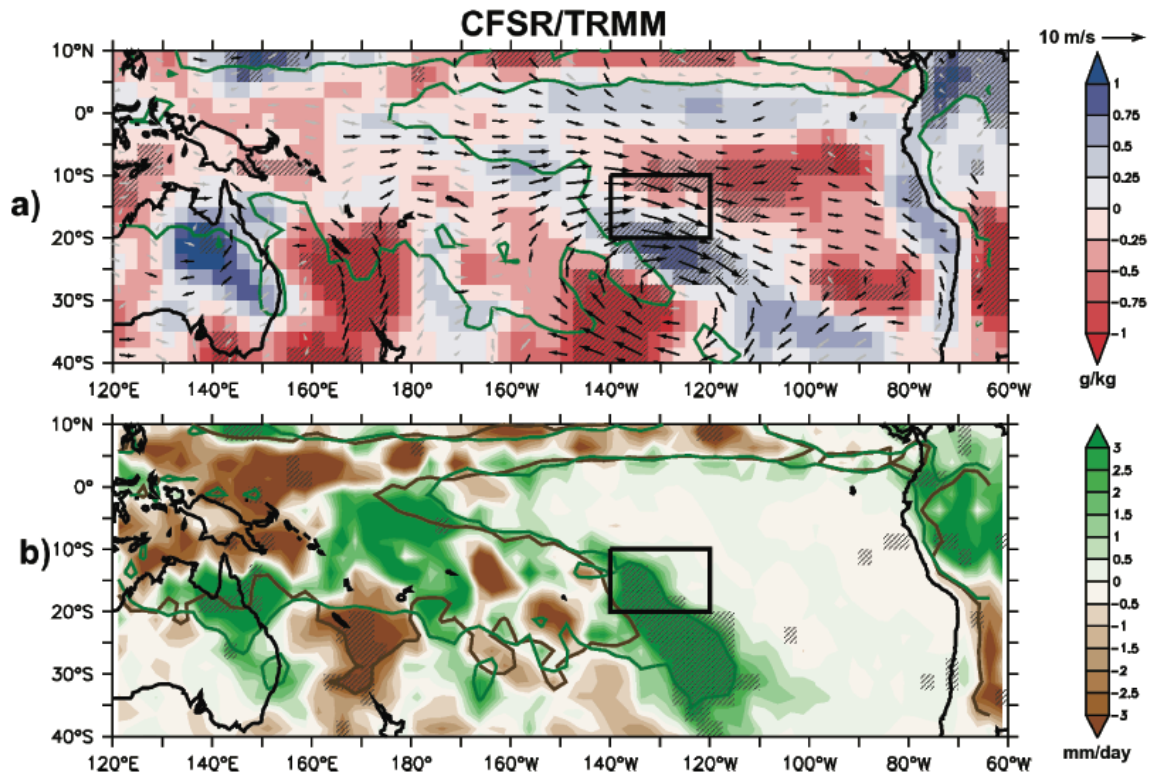


**Figure 2.3.** Same as Figure 2.2, but during the period 1998-2010 and replacing CFSR precipitation with TRMM 3B42 precipitation estimates.



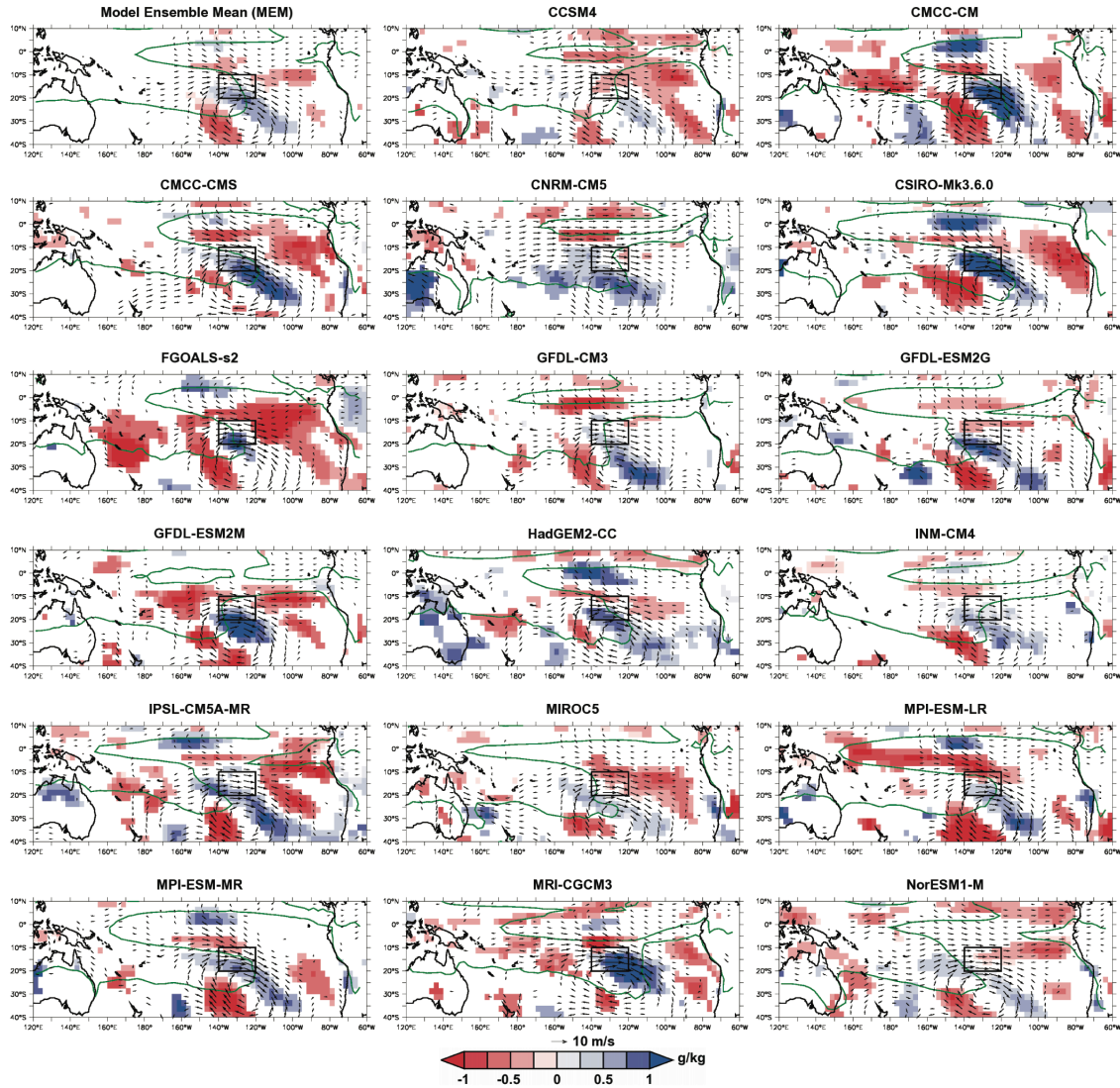


**Figure 2.4.** Composite analysis applied to model output from the CMIP5 historical experiment. Shown are composite differences (weak-inflow minus strong-inflow) of 850 hPa zonal and meridional wind (vectors, in m/s) and 850 hPa specific humidity (shading, in g/kg) for a composite index of zonal wind at 850 hPa averaged over 140°W-120°W and 20°S-10°S. Data appears only if it is significant at the 99<sup>th</sup> percentile except for the model ensemble mean, which considers a value at a particular spatial point significant if a majority of the models (nine) agree on significance there. Included for reference are the January SPCZ climatology (green contour, 4 mm/day) as well as the region in which the

composite index was calculated (black box).

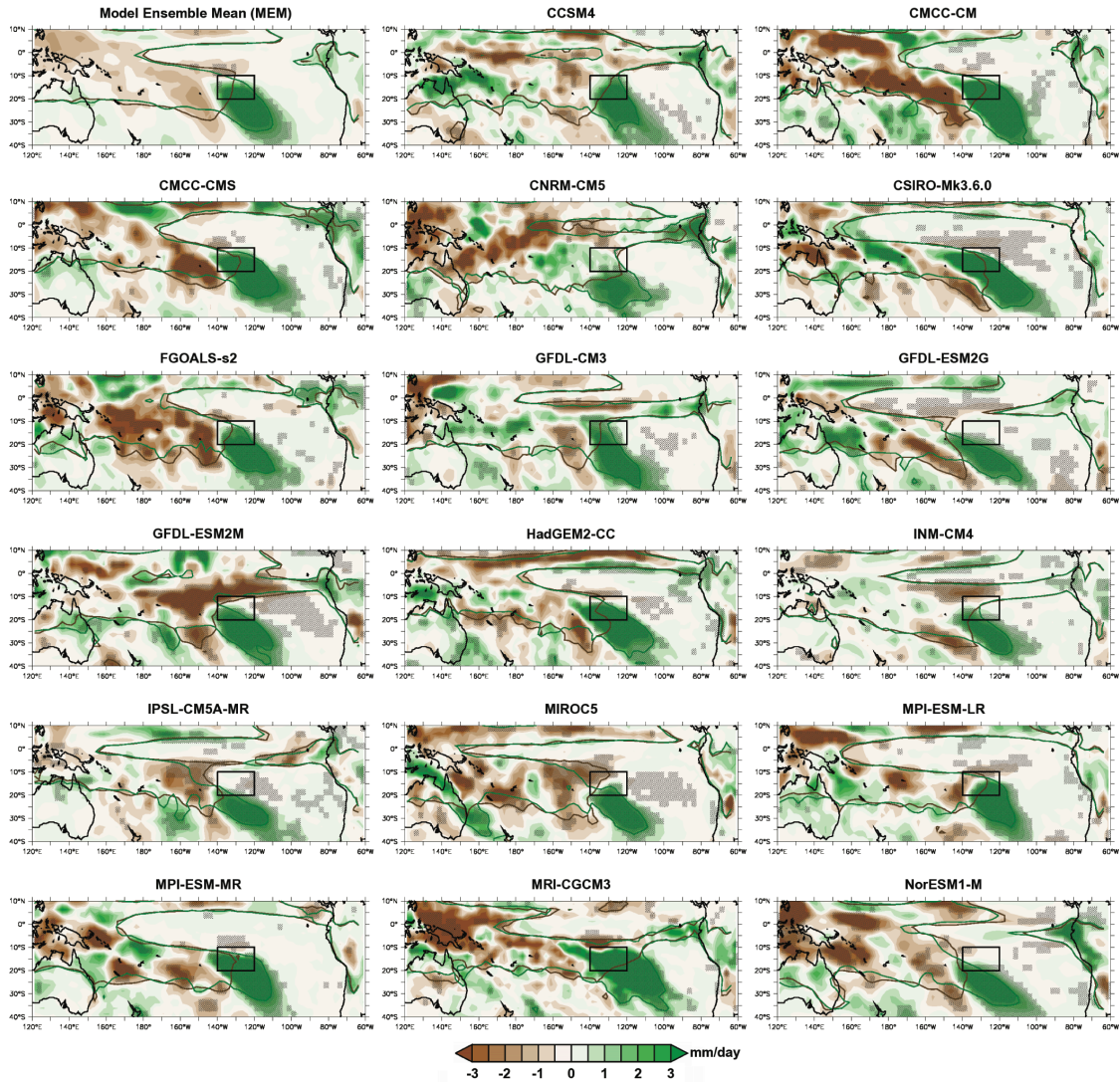


**Figure 2.5.** Composite analysis applied to model output from the CMIP5 historical experiment. Shown are composite differences (weak-inflow minus strong-inflow) of precipitation (shading, in mm/day) for a composite index of zonal wind at 850 hPa averaged over 140°W-120°W and 20°S-10°S. Significance for precipitation (at the 99<sup>th</sup> percentile) is denoted by dark grey striping. Included for reference are the 4 mm/day precipitation contours for the weak-inflow phase (in green) and strong-inflow phase (in brown) as well as the region in which the composite index was calculated (black box).

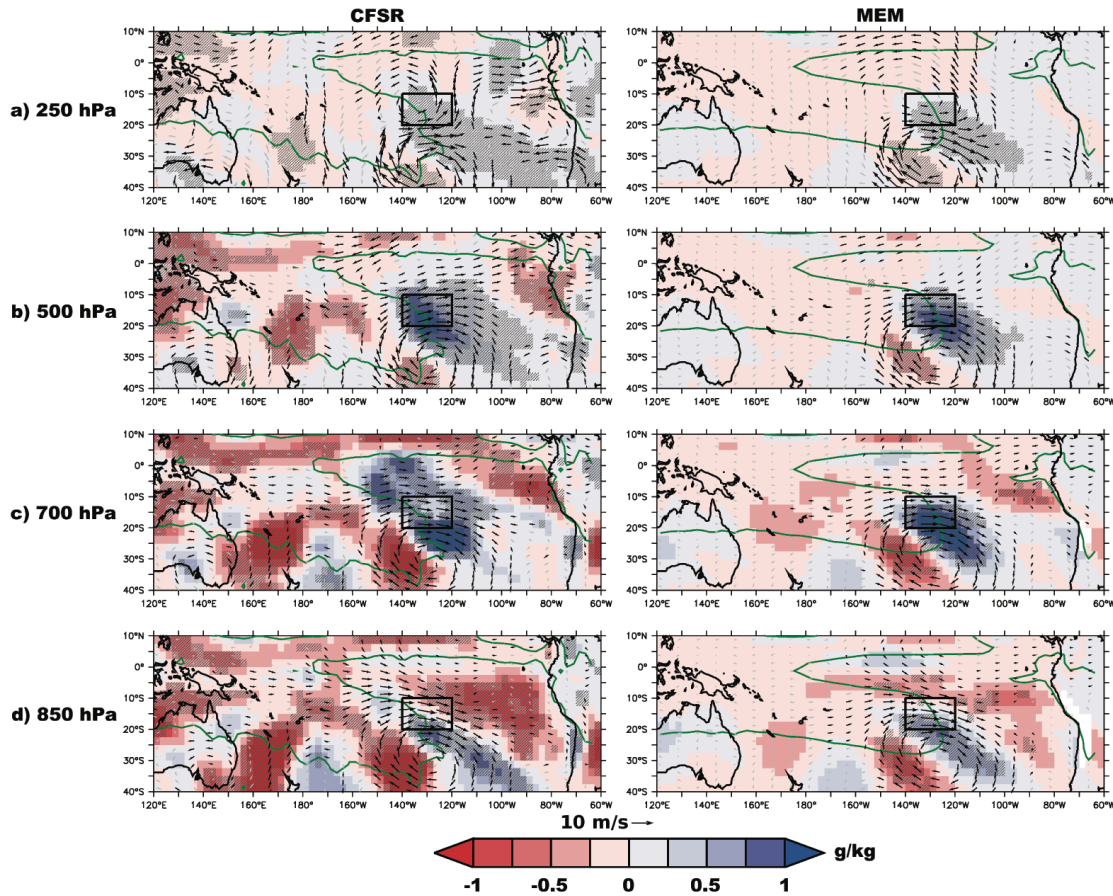


**Figure 2.6.** Results of the composite analysis at 850 hPa shown at multiple vertical levels. CFSR (d) is the same as Figure 2.2a for CFSR. MEM (d) is the same result as Figure 2.4, though now the significance conventions of Figure 2.2 are used (i.e. non-significant wind and moisture anomalies are still plotted). (a), (b), and (c) show results at 250 hPa, 500 hPa, and 700 hPa, respectively, with significance associated with each plots' respective level (i.e. moisture in CFSR (c) is significant if it exceeds the 99<sup>th</sup> percentile of random composites generated at 700 hPa, etc.). Also included for reference is the mean 4 mm/day precipitation contour (in green) as well as the region in which the composite index was calculated (black box).



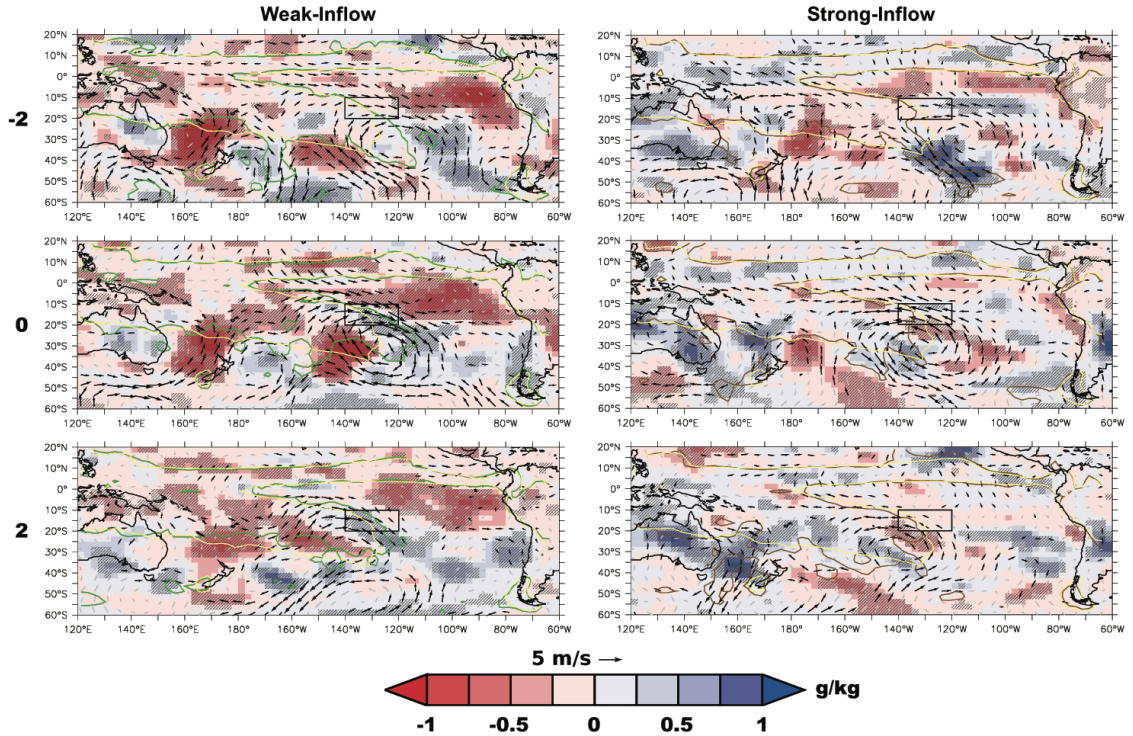


**Figure 2.7.** Lead-lag composite differences using CFSR data. Each panel shows the difference in wind (vectors, in m/s) and specific humidity (shading, in g/kg) between the weak-inflow/strong-inflow phase composite at a given number of days before or after a maximum or minimum (i.e. -2, the top row, shows composites 2 days before a maximum or minimum) and the mean 27 December – 4 February (40 day period) state. Significance for wind and moisture (at the 99<sup>th</sup> percentile) is denoted by black vector color and dark grey striping, respectively. Also included for reference are the composite 4 mm/day precipitation contour (weak-inflow phase, in green; strong-inflow phase, in brown), the mean 27 December – 4 February (40 day period) 4 mm/day precipitation contour (in light yellow), and the region in which the composite index was calculated (black box).

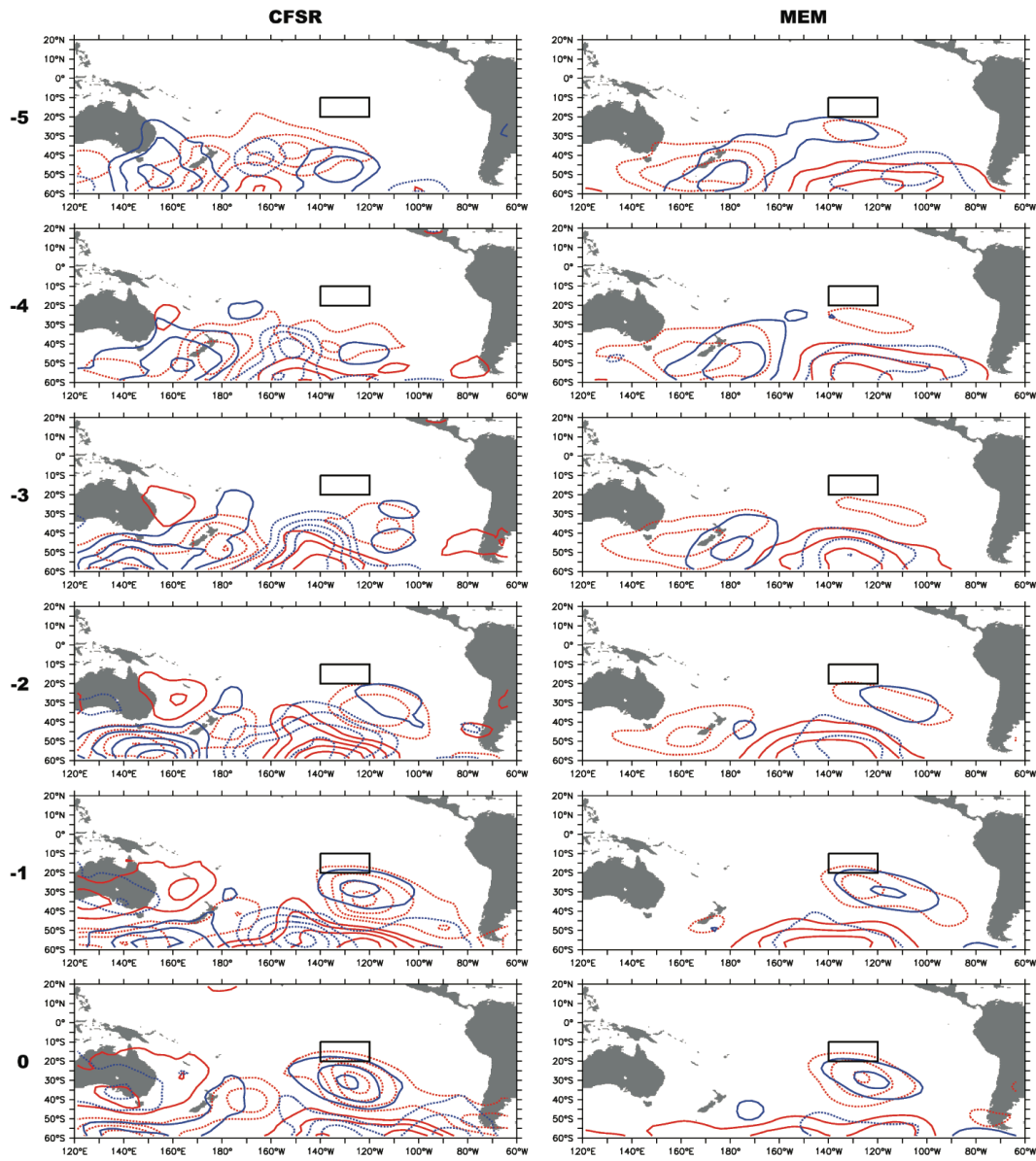


**Figure 2.8.** Lead-lag composites using CFSR (left) and CMIP5 MEM (right) data. For CFSR, sea level pressure anomalies from the January mean are plotted every 1 hPa (positive values solid, negative dashed) for the weak-inflow phase (in red) and strong-inflow phase (in blue). Similar for MEM, but using a smaller contour interval of 0.5 hPa. 0 hPa line is omitted. Included for reference is the region in which the composite index was calculated (black box).

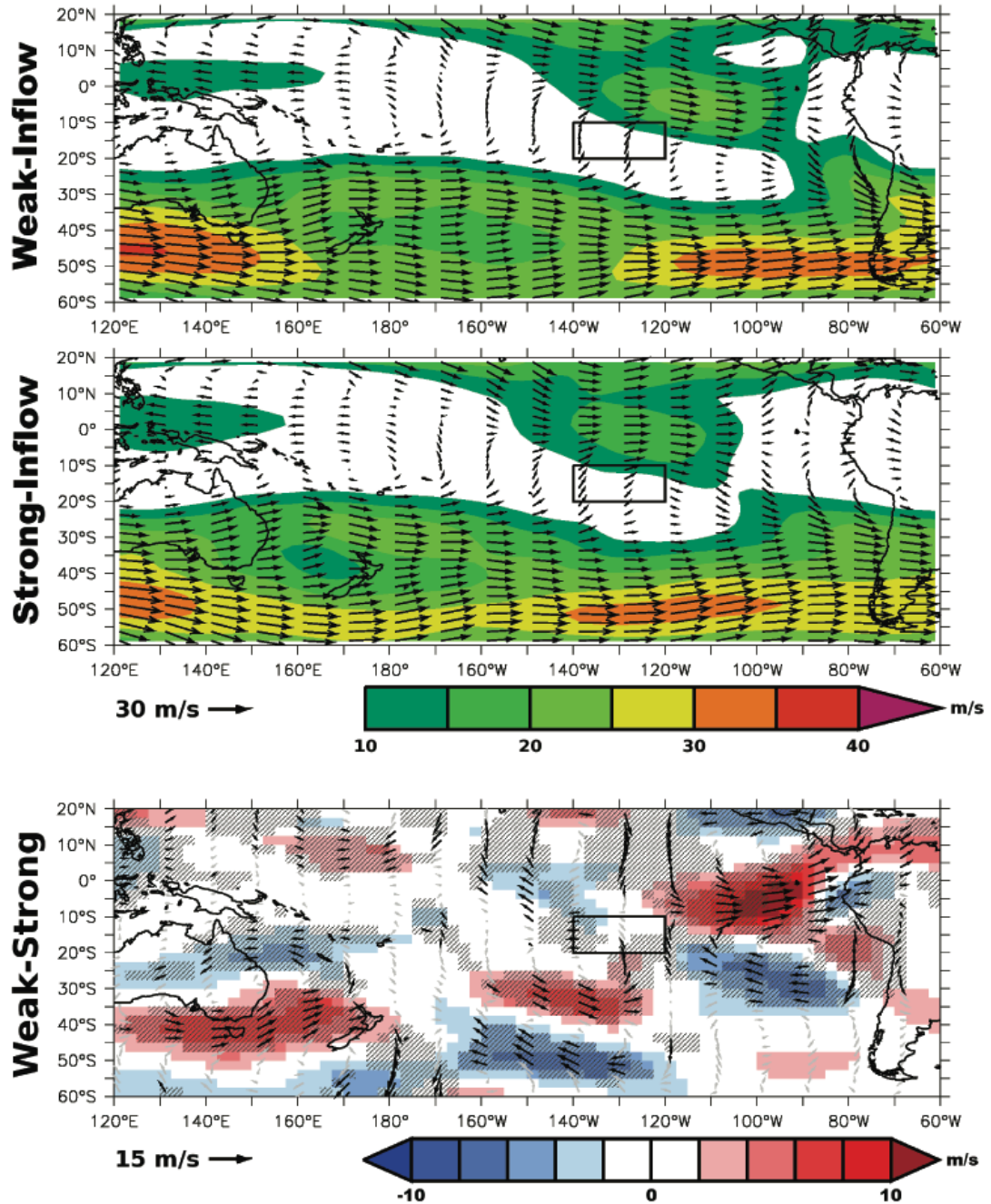


**Figure 2.9.** Composites of 250 hPa wind (shading and vectors, m/s) averaged between day -5 and day -3 of the weak-inflow (top) and strong-inflow (middle) phases as well as their difference (weak-inflow – strong-inflow, bottom). Significance for wind (at the 99<sup>th</sup>) percentile is denoted by black vector color and dark grey striping.

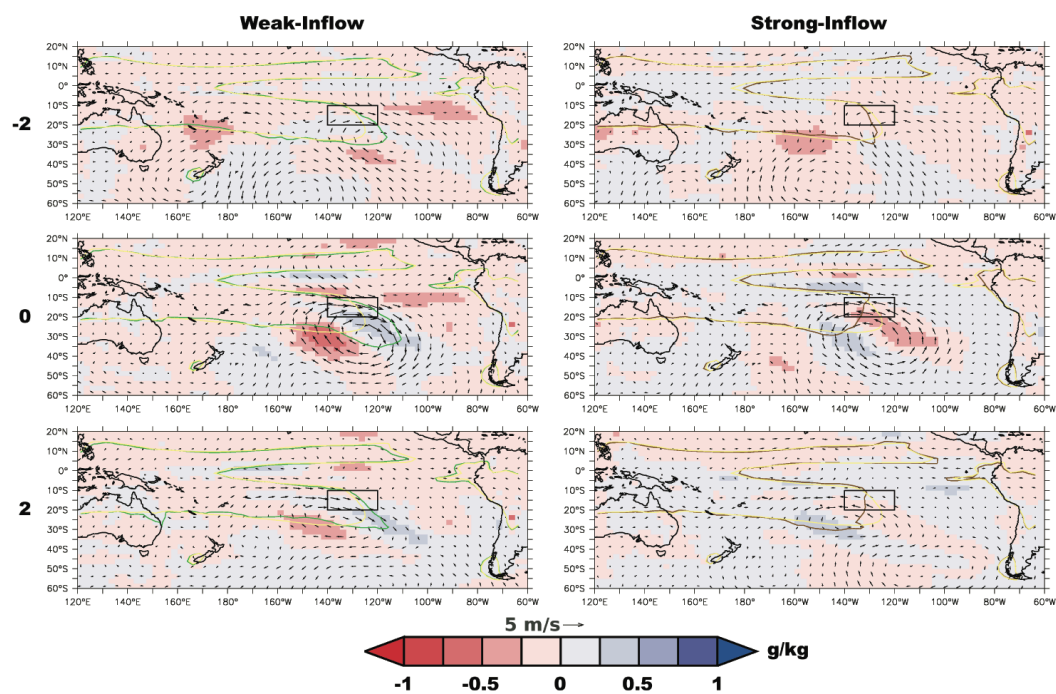


**Figure 2.10.** Same as Figure 2.7, but using MEM data.



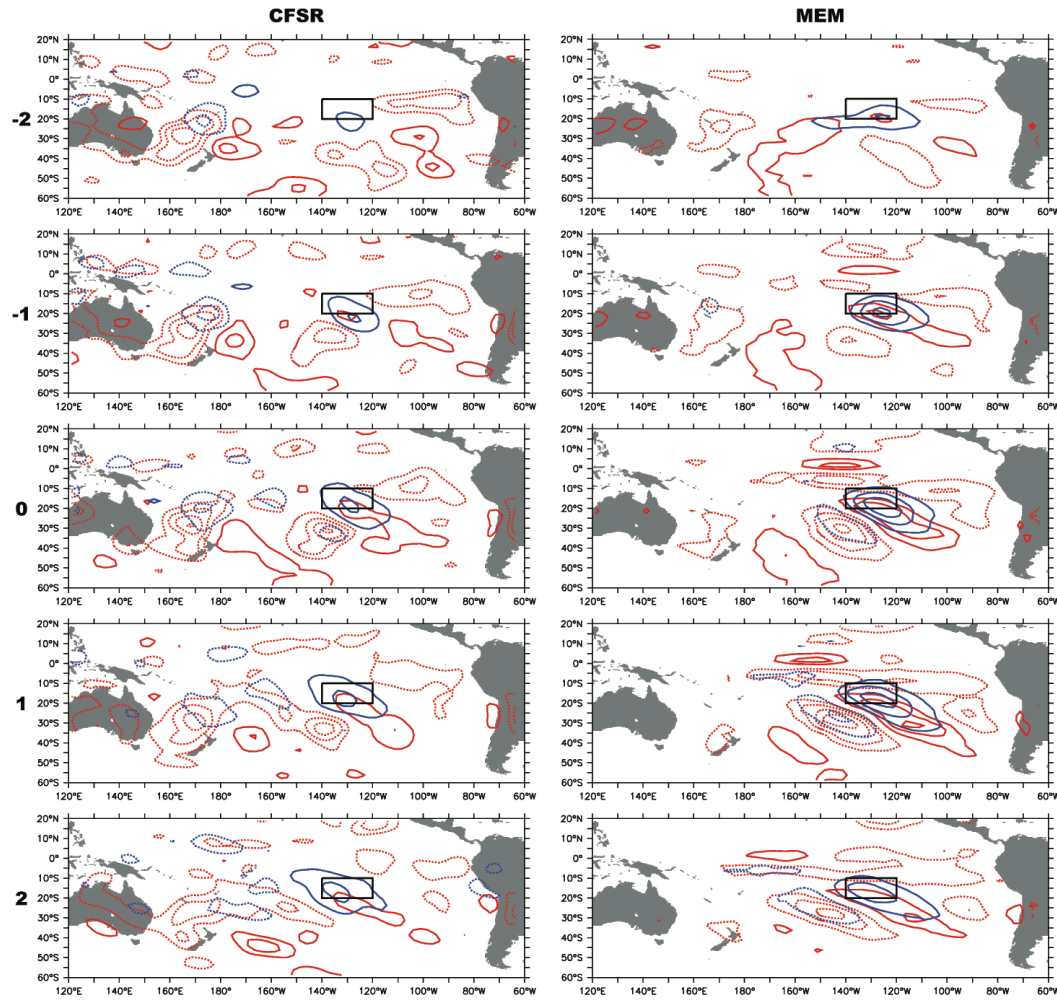


**Figure 2.11.** Lead-lag composites using CFSR (left) and CMIP5 MEM (right) data. For CFSR, specific humidity anomalies at 850 hPa (in red) and 500 hPa (in blue) are plotted every  $0.5 \text{ g kg}^{-1}$  (positive values solid, negative dashed) for weak-inflow phase minus strong-inflow phase. Similar for MEM, but using a smaller contour interval of  $0.25 \text{ g kg}^{-1}$ .  $0 \text{ g kg}^{-1}$  line is omitted.

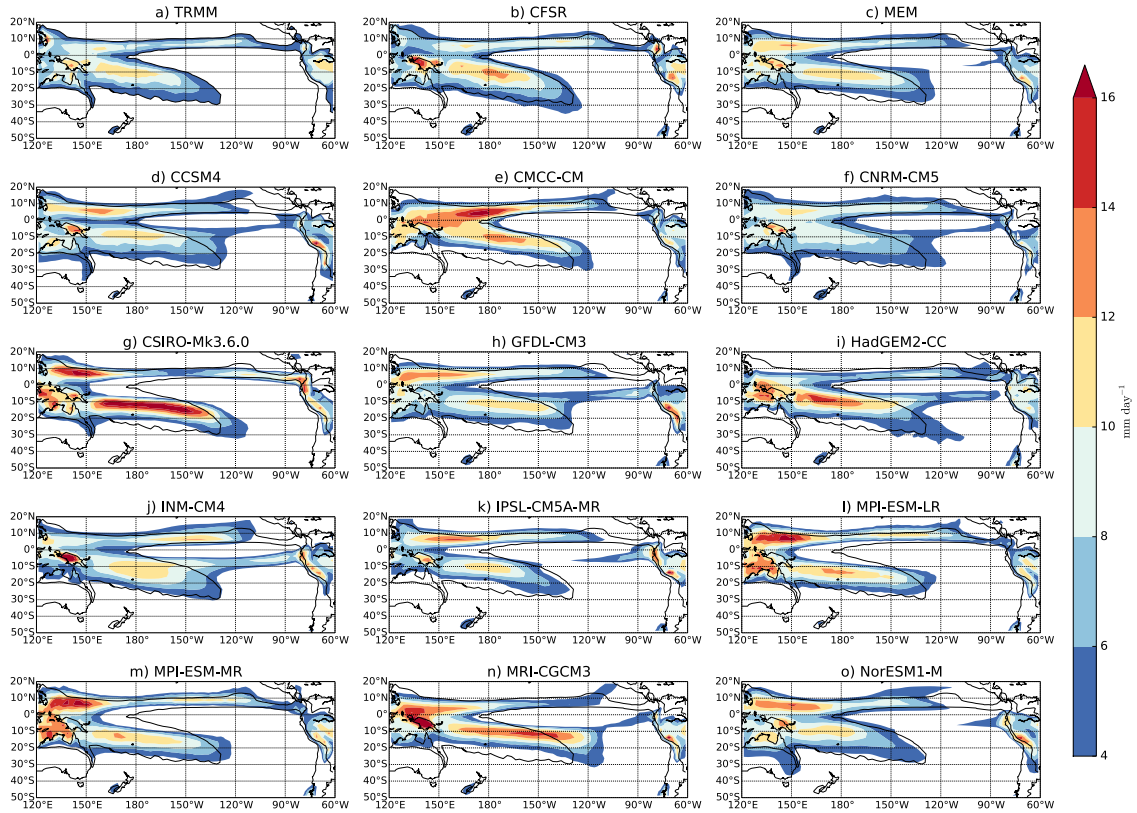


**Figure 3.1.** Climatological DJF precipitation (shading, mm day<sup>-1</sup>) over the Pacific for the (a) TRMM estimated data set, (b) Climate Forecast System Reanalysis (CFSR), (c) Coupled Model Intercomparison Project Phase 5 (CMIP5) coupled model ensemble mean (MEM), (d)-(o) individual CMIP5 coupled model means. The thick black line in all panels is the TRMM 4 mm day<sup>-1</sup> contour, for reference.

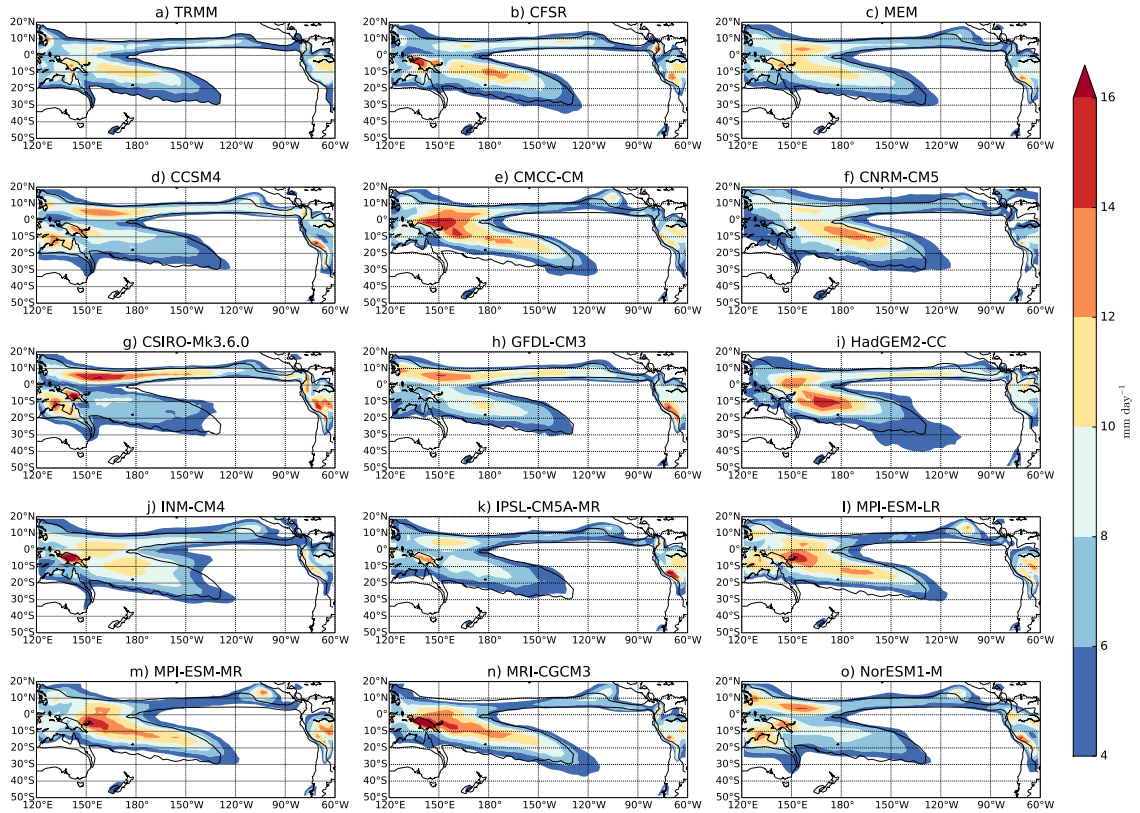


**Figure 3.2.** As Figure 3.1, but for the (c) model ensemble mean, and (d)-(o) individual means of the atmosphere-only models.

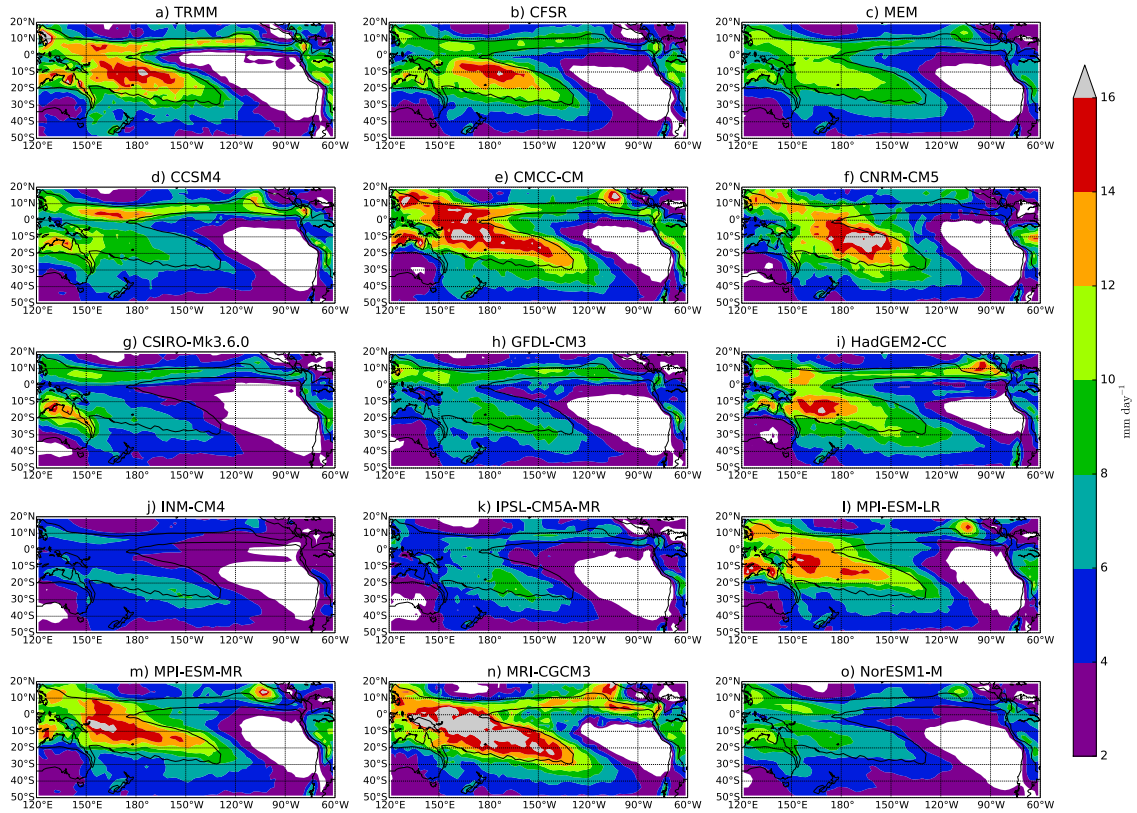


**Figure 3.3.** Climatological DJF precipitation standard deviation (shading,  $\text{mm day}^{-1}$ ) over the Pacific for the (a) TRMM estimated data set, (b) CFSR, (c) CMIP5 atmosphere-only model ensemble mean (MEM), (d)-(o) individual CMIP5 atmosphere-only model means. The thick black line in all panels is the TRMM  $4 \text{ mm day}^{-1}$  climatological precipitation contour, for reference.

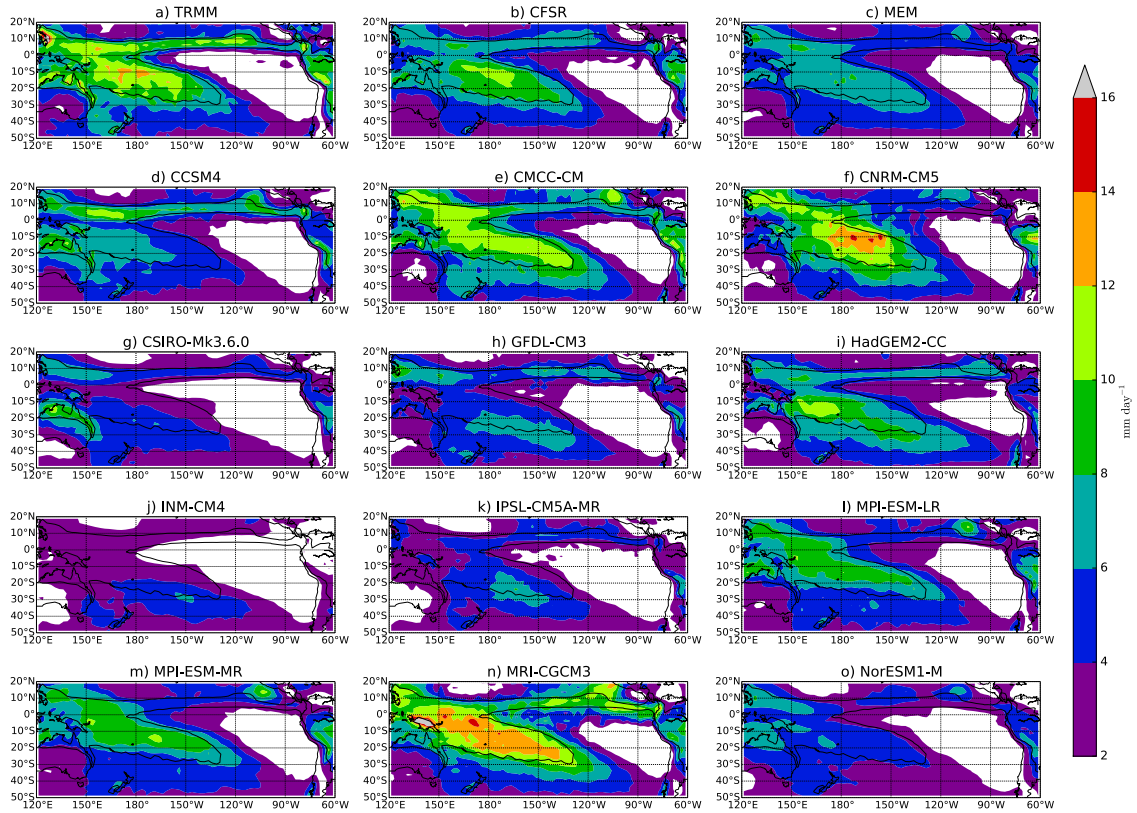


**Figure 3.4.** As Figure 3.3, but for standard deviation of 14-day high-pass filtered precipitation.

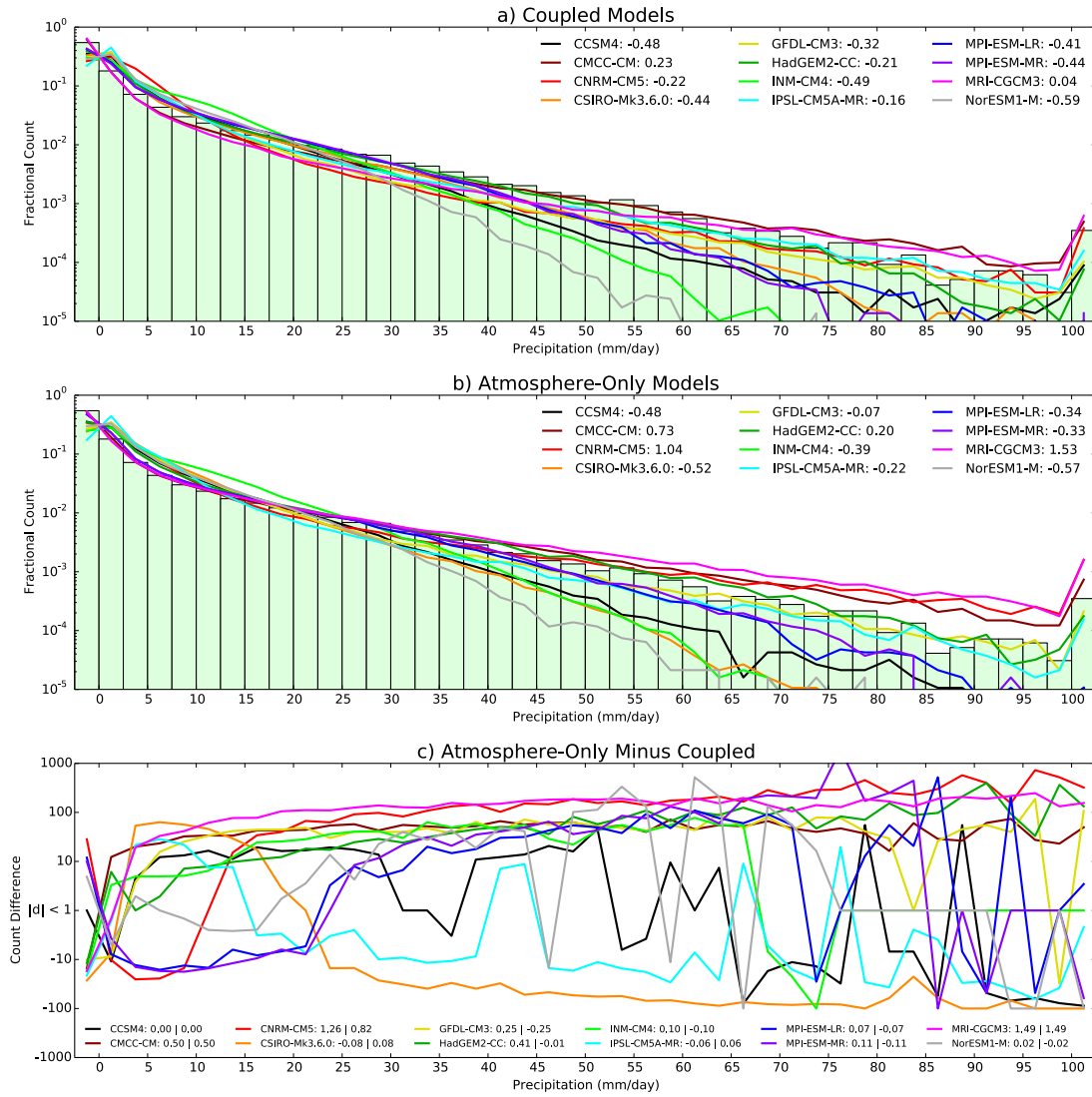


**Figure 3.5.** Normalized, logarithmic DJF precipitation histograms in the region 165°W–135°W, 20°S–35°S from (a) coupled and (b) atmosphere-only models as well as their differences. The first bin measures 0–0.5 mm day<sup>-1</sup> counts, followed by 0.5–2.5 mm day<sup>-1</sup>, with each subsequent bin having size 2.5 mm day<sup>-1</sup> (e.g. 2.5–5.0 mm day<sup>-1</sup>). The final bin measures precipitation values exceeding 100 mm day<sup>-1</sup>. (a) TRMM (green boxes) and coupled models (lines); error (see Section 3.2 for details) shown in the legend for each model. (b) TRMM (green boxes) and atmosphere-only models (lines); error from TRMM shown in the legend for each model. (c) Difference between atmosphere-only and

coupled model histograms for each model (lines); difference and increase/decrease in error, respectively, between atmosphere-only and coupled histograms shown in the legend for each model.



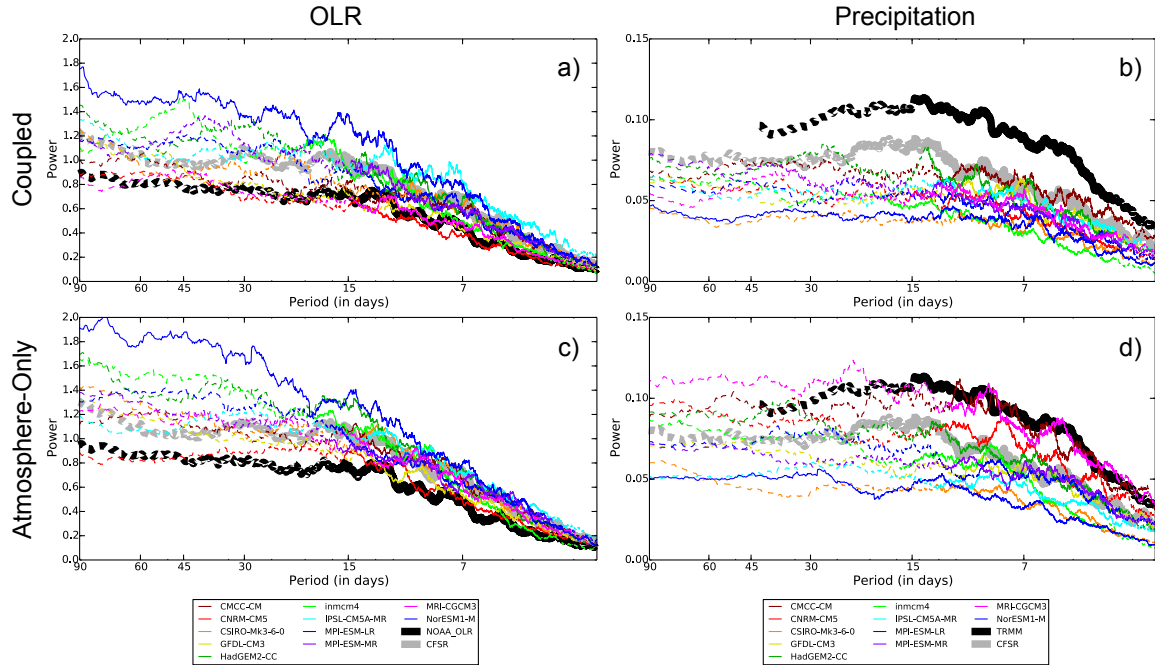


**Figure 3.6.** Normalized power spectra in coupled (top row) and atmosphere-only (bottom row) models. For OLR spectra (left column), models are compared to CFSR and a NOAA OLR observational dataset. For precipitation spectra (right column), models are compared to CFSR and TRMM precipitation estimates. Solid/dashed line indicates variability above/below the significance threshold (explained in Section 3.2).



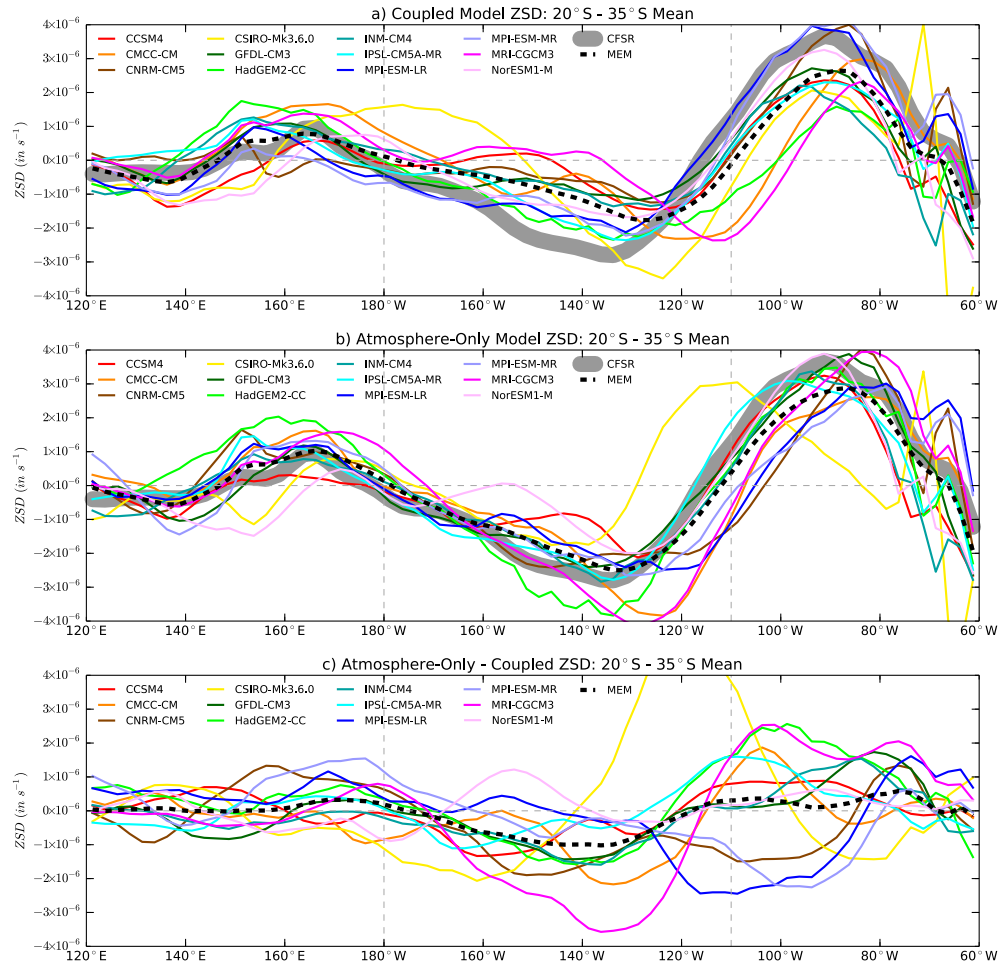


**Figure 3.7.** Meridional average (20°S–35°S) of zonal stretching deformation (ZSD) in CFSR and models across the South Pacific (120°E–60°W), for (a) coupled, (b) atmosphere-only, and (c) difference between atmosphere-only and coupled models. MEM denotes the model ensemble mean in each panel.

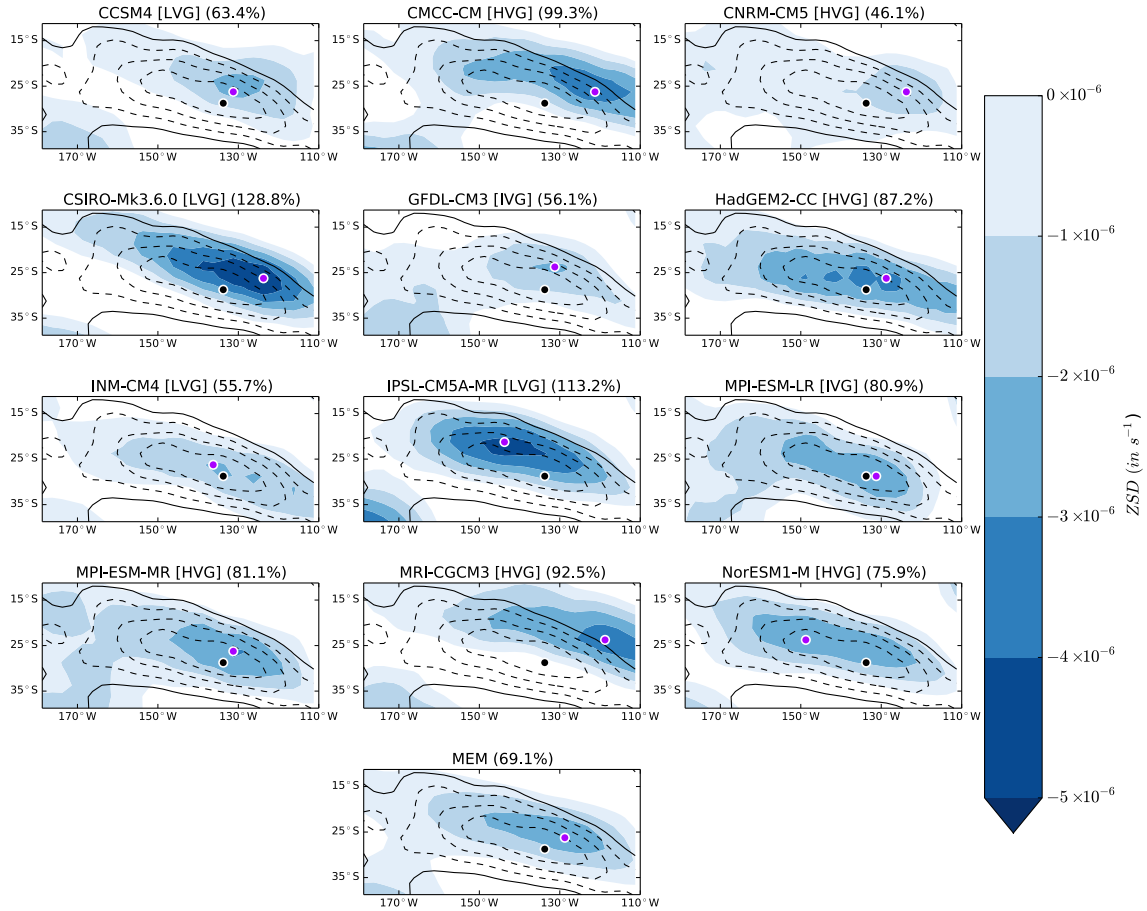


**Figure 3.8.** Coupled model negative zonal stretching deformation (ZSD) at 250 hPa (blue shading,  $s^{-1}$ ) as compared to CFSR negative ZSD (black contours) at the same level in the storm graveyard region, as well as the coupled model ensemble mean (MEM). The location of the CFSR (black dot) and individual model or MEM (purple dot) ZSD minimum are shown for reference. The relative strength of the minimum value of ZSD in each model compared to CFSR is shown in parentheses after each model name.

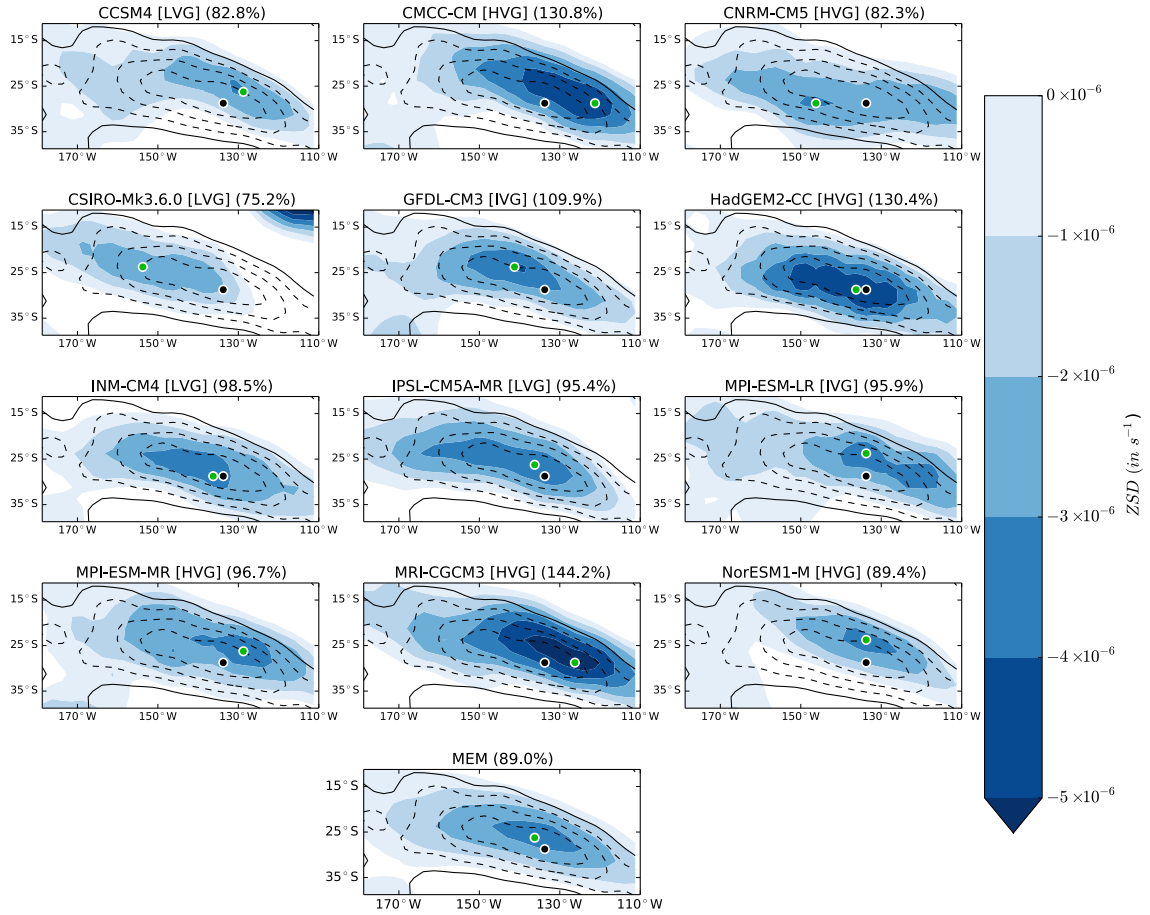


**Figure 3.9.** As Figure 3.8, but using data from the atmosphere-only models and their MEM. The locations of the individual model or MEM ZSD minima are now denoted by a green dot.

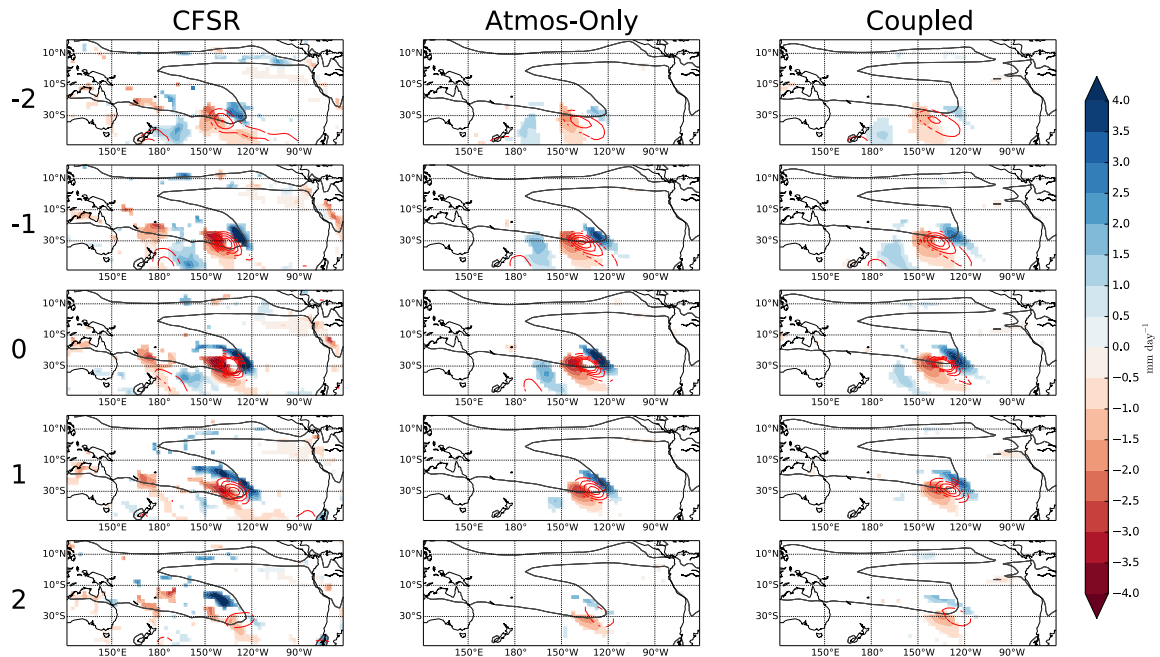


**Figure 3.10.** Composite analysis using 250 hPa vorticity in the region 140°W–127.5°W, 27.5°S–30°S CFSR (left column), atmosphere-only MEM (middle column), and coupled MEM (right column). Each row denotes the days before/after the low vorticity event (i.e. -2 is 2 days before, etc.). Shown in each panel are precipitation anomalies (shading, mm day<sup>-1</sup>), negative vorticity anomalies (red contours, starting at 0 s<sup>-1</sup>; each subsequent contour is  $-1 \times 10^{-5}$  s<sup>-1</sup>), and the data source's climatological 4 mm day<sup>-1</sup> precipitation (black contour). For CFSR, anomalies are only shown if they are greater than 99% of randomly generated composite differences. For the coupled and atmosphere-only MEMs, anomalies are shown if 8 or more of the models agree on both the sign and significance (same as for CFSR) of the anomaly at any given location.

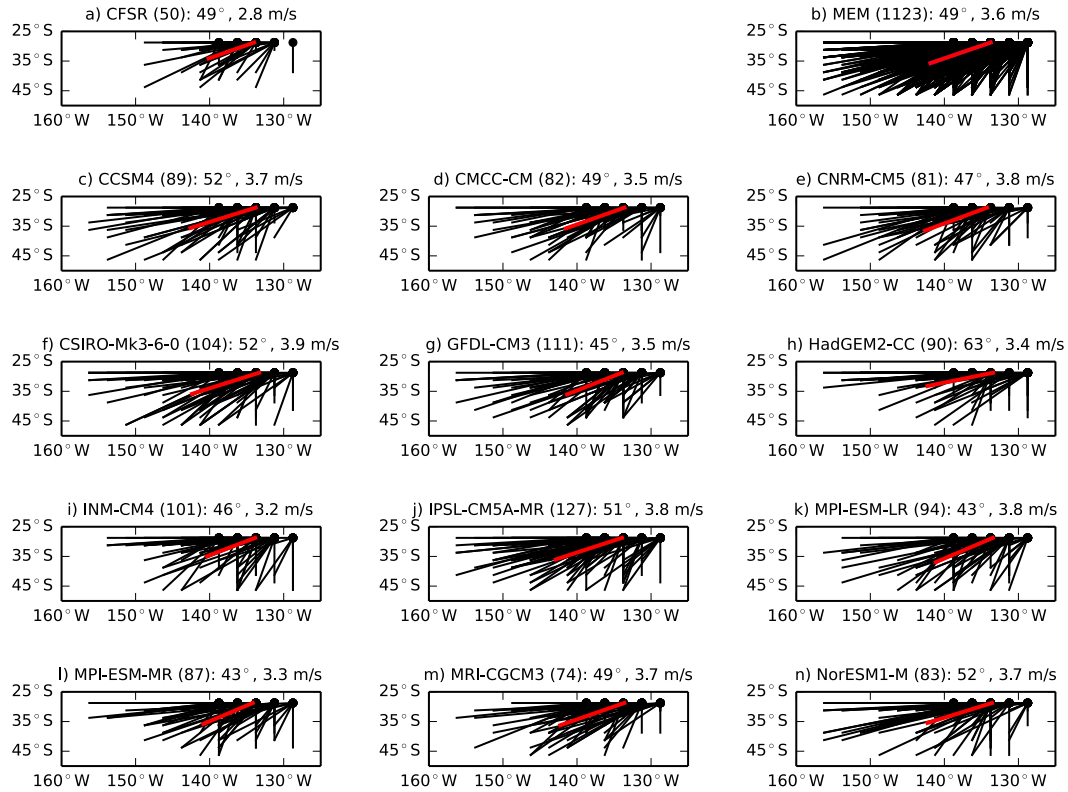


**Figure 3.11.** Linear trajectories of storms entering the SPCZ included in the composites shown in Figure 10 for (a) CFSR, (b) coupled model ensemble mean, (c)-(n) individual coupled models. Listed after the data sources name are the number of storms plotted (in parentheses) as well as the angle and speed of the red trajectory, which connects the mean starting and ending position for each data source. For angles,  $0^\circ$  is toward due north,  $90^\circ$  is toward due east, etc.

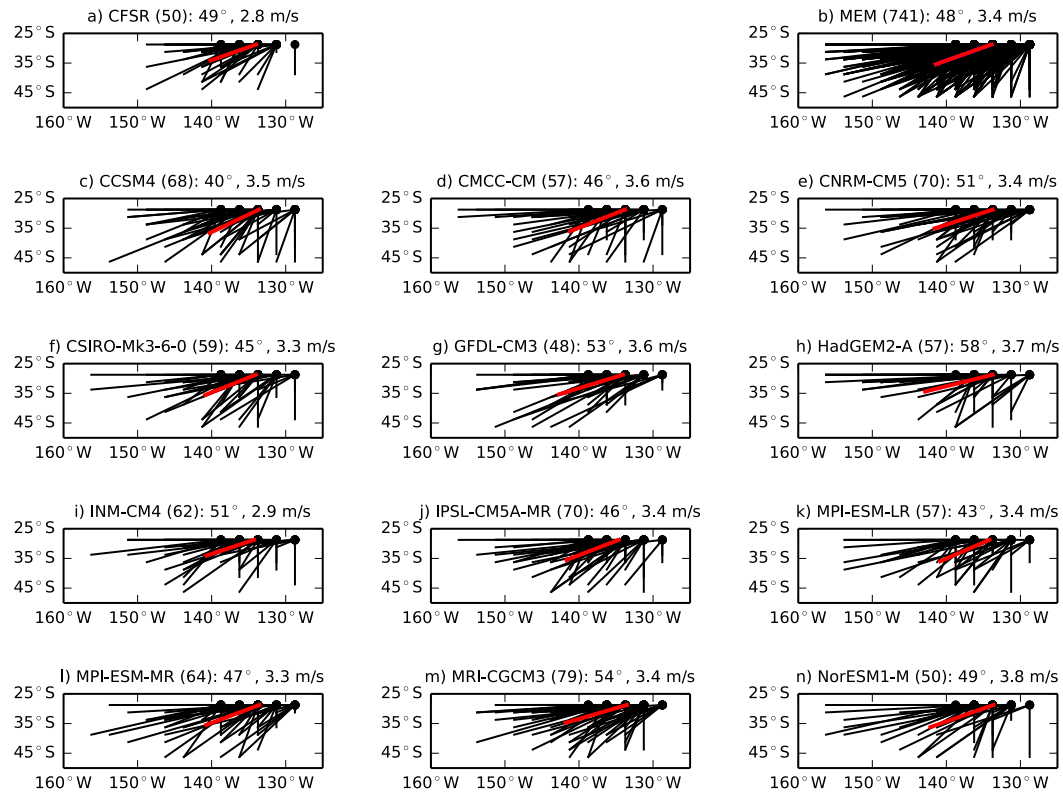


**Figure 3.12.** As Figure 3.11, but for atmosphere-only models.

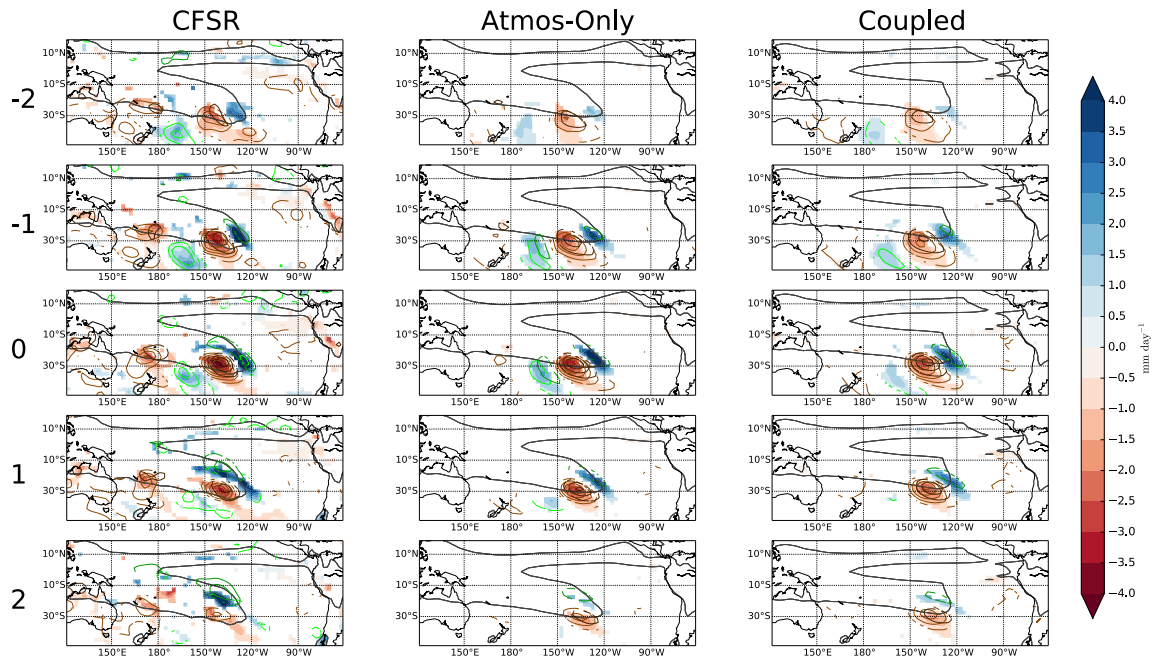


**Figure 3.13.** As Figure 3.10, but replacing vorticity anomalies with moisture anomalies at two levels. Positive moisture anomalies are contoured at 850 hPa (light green) and 500 hPa (dark green) every  $0.25 \text{ g kg}^{-1}$ ; similarly, negative moisture anomalies are contoured at 850 hPa (light brown) and 500 hPa (dark brown) every  $0.25 \text{ g kg}^{-1}$ . The same significance criteria are used for moisture that were used for precipitation and vorticity in Figure 3.10.

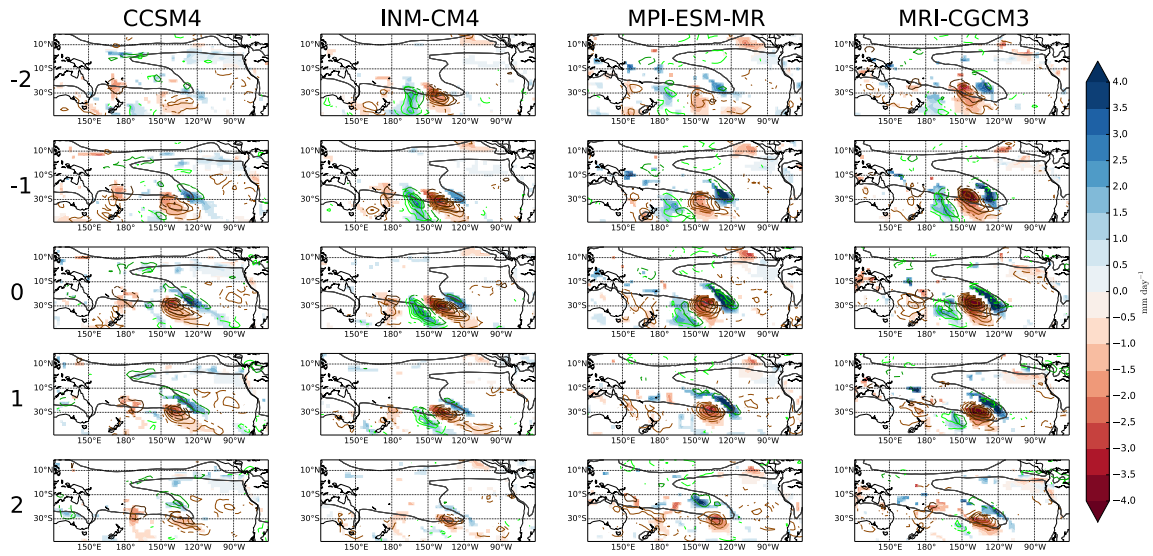


**Figure 3.14.** As Figure 3.13, but showing four individual atmosphere-only models. Significance criteria for showing precipitation/moisture anomalies is the same that was used for CFSR in Figures 3.10 and 3.13.



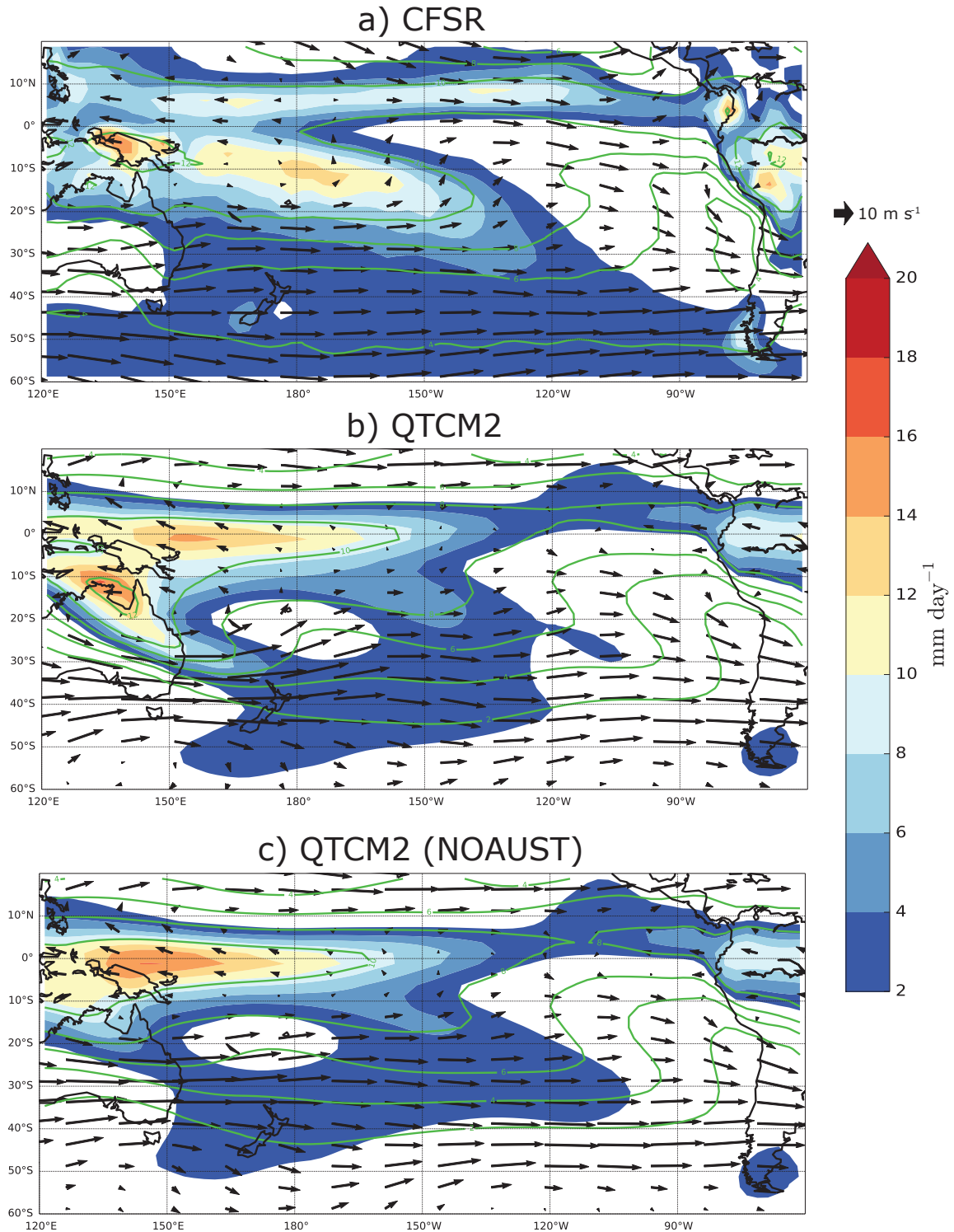


**Figure 4.1.** Climatological DJF 250 hPa wind (vectors, in  $\text{m s}^{-1}$ ), 850 hPa specific humidity (green contours, every  $2 \text{ g kg}^{-1}$ ), and precipitation (shading, in  $\text{mm day}^{-1}$ ) in a) CFSR, b) QTCM2 (CON32 experiment), and c) QTCM2 (CON32\_NOAUST

experiment).

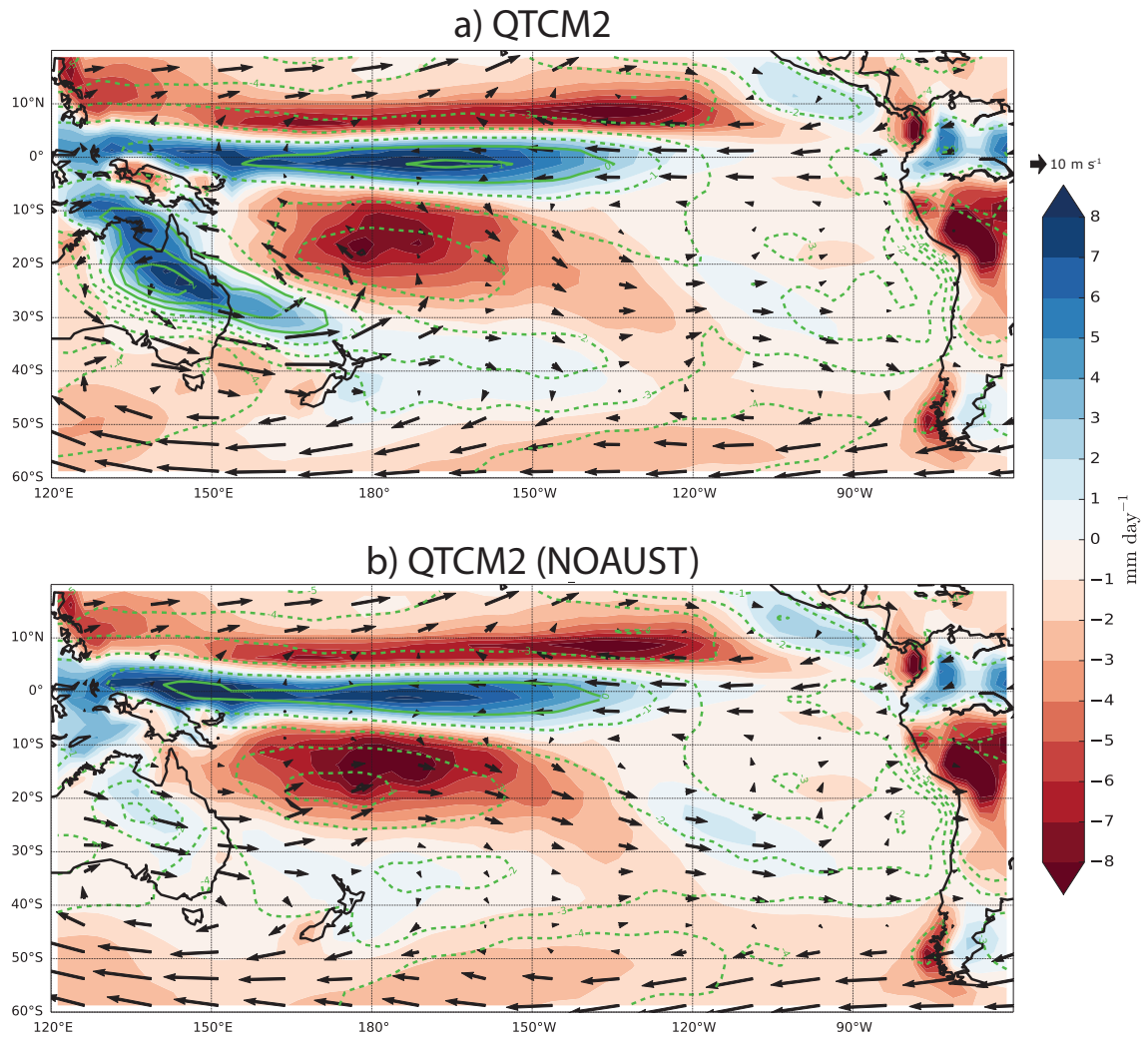


**Figure 4.2.** DJF biases in 250 hPa wind (vectors, in  $\text{m s}^{-1}$ ), 850 hPa specific humidity (green contours, every  $1 \text{ g kg}^{-1}$ ), and precipitation (shading, in  $\text{mm day}^{-1}$ ) compared to CFSR for a) QTCM2 (CON32 experiment) and b) QTCM2 (CON32\_NOAUST experiment).

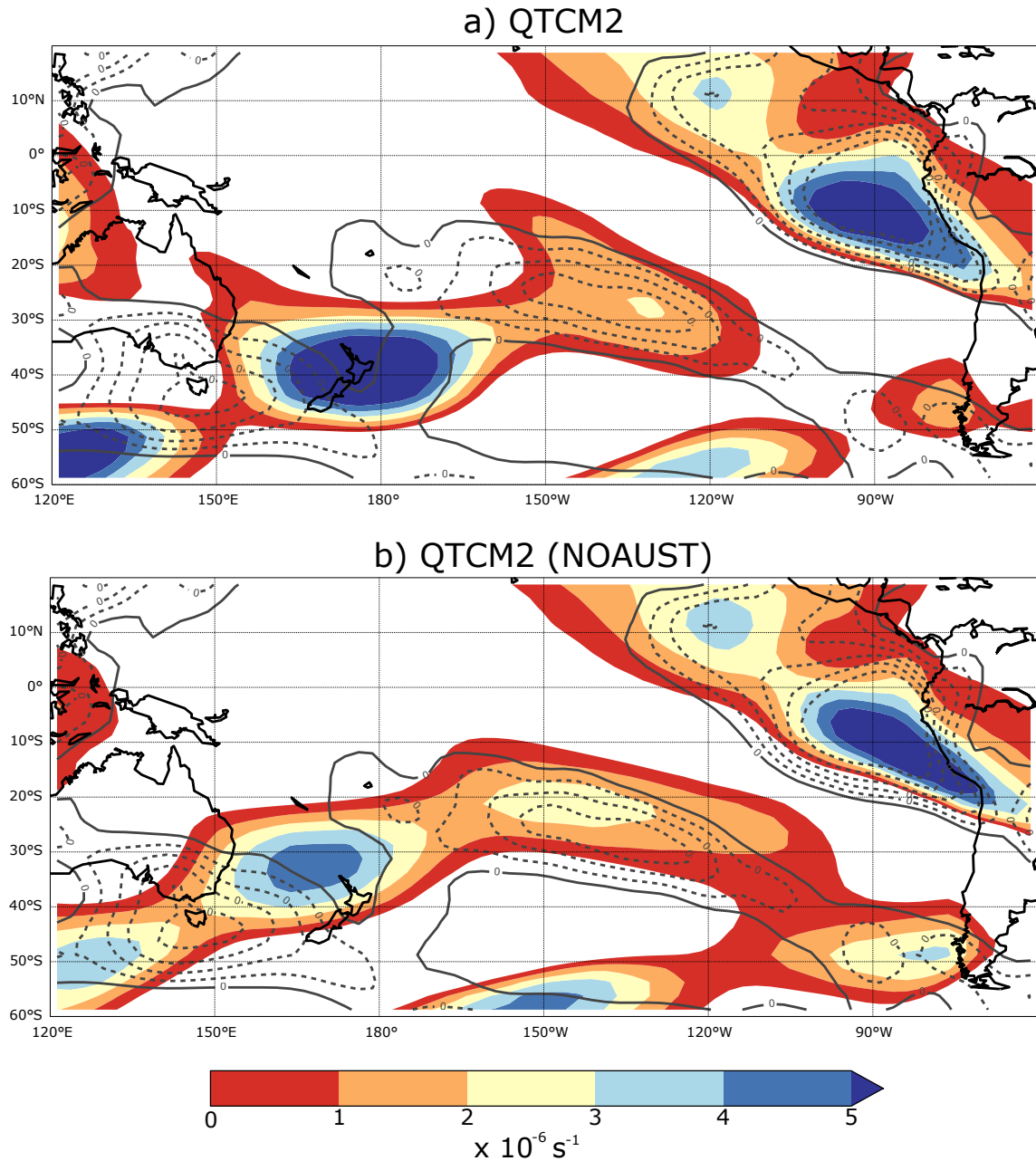


**Figure 4.3.** Climatological DJF negative zonal stretching deformation (shaded, in  $\text{s}^{-1}$ ) in a) QTCM2 (CON32 experiment) and b) QTCM2 (CON32\_NOAUST experiment). CFSR DJF negative zonal stretching deformation (grey contours, every  $1 \times 10^{-6} \text{ s}^{-1}$ ) included in each plot for comparison.

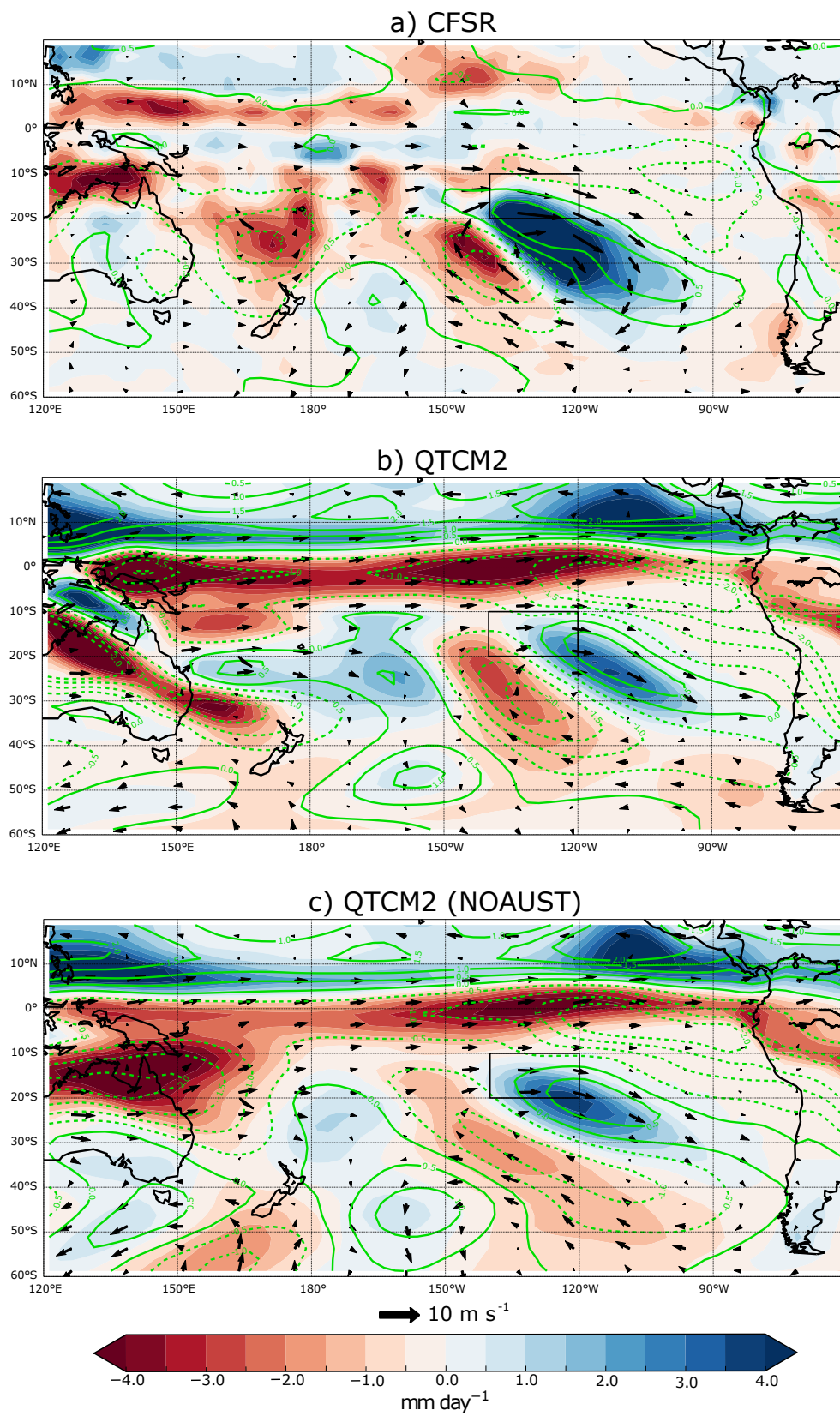


**Figure 4.4.** Composite difference (weak-inflow minus strong-inflow phase) of wind (vectors, in  $\text{m s}^{-1}$ ), specific humidity (green contours, every  $0.5 \text{ g kg}^{-1}$ ), and precipitation (shading, in  $\text{mm day}^{-1}$ ) in a) CFSR, b) QTCM2 (CON32 experiment), and c) QTCM2 (CON32\_NOAUST experiment). Composite analysis based on anomalous 850 hPa zonal wind in the box  $140^{\circ}\text{W}$ – $120^{\circ}\text{W}$ ,  $10^{\circ}\text{S}$ – $20^{\circ}\text{S}$ , with the monthly mean subtracted from each value.



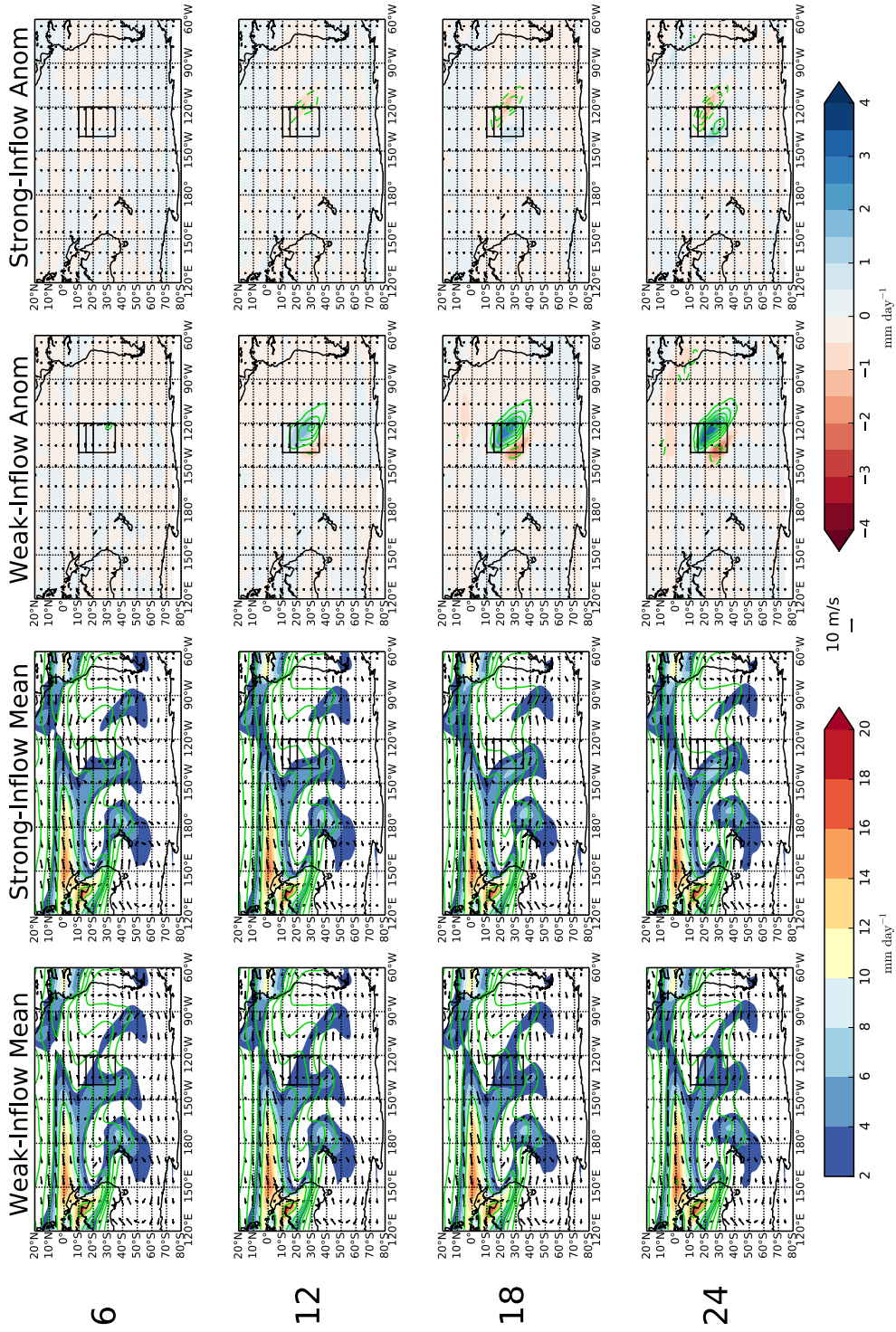


**Figure 4.5.** Results from the W100 and S100 experiments. Each row shows a 2-hour mean (x-2 through x hours after imposed anomaly) from W100 (mean values in leftmost column, anomalies in right-center column) and S100 (mean values in left-center column, anomalies in rightmost column). Fields shown are derived 850 hPa wind (vectors, in  $\text{m s}^{-1}$ ), derived 850 hPa specific humidity (green contours, in  $\text{g kg}^{-1}$ ; every  $2 \text{ g kg}^{-1}$  for mean values, every  $0.25 \text{ g kg}^{-1}$  for anomalies), and precipitation (shaded, in  $\text{mm day}^{-1}$ ).



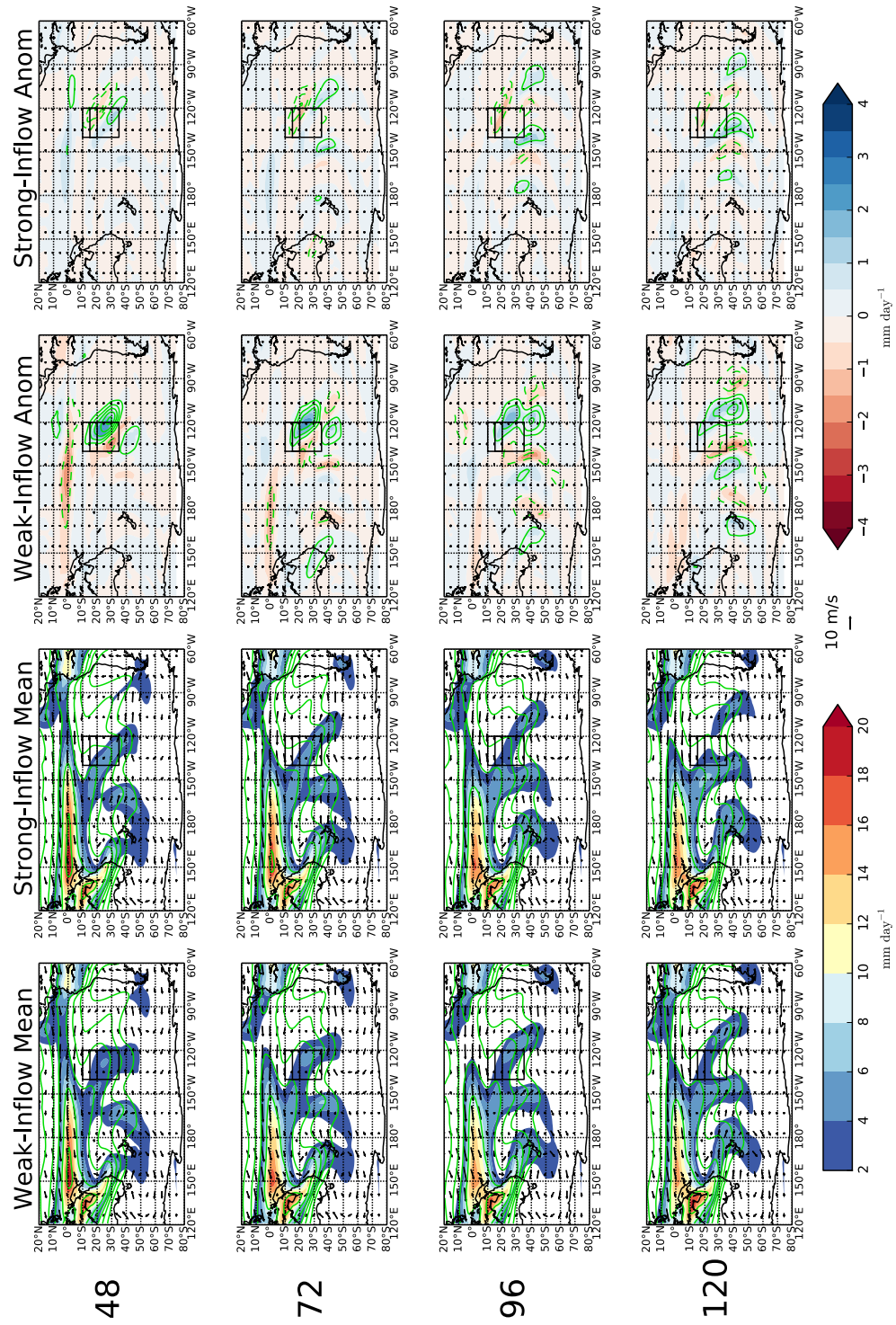


**Figure 4.6.** As Figure 4.5, but with different times (48-120 hours).

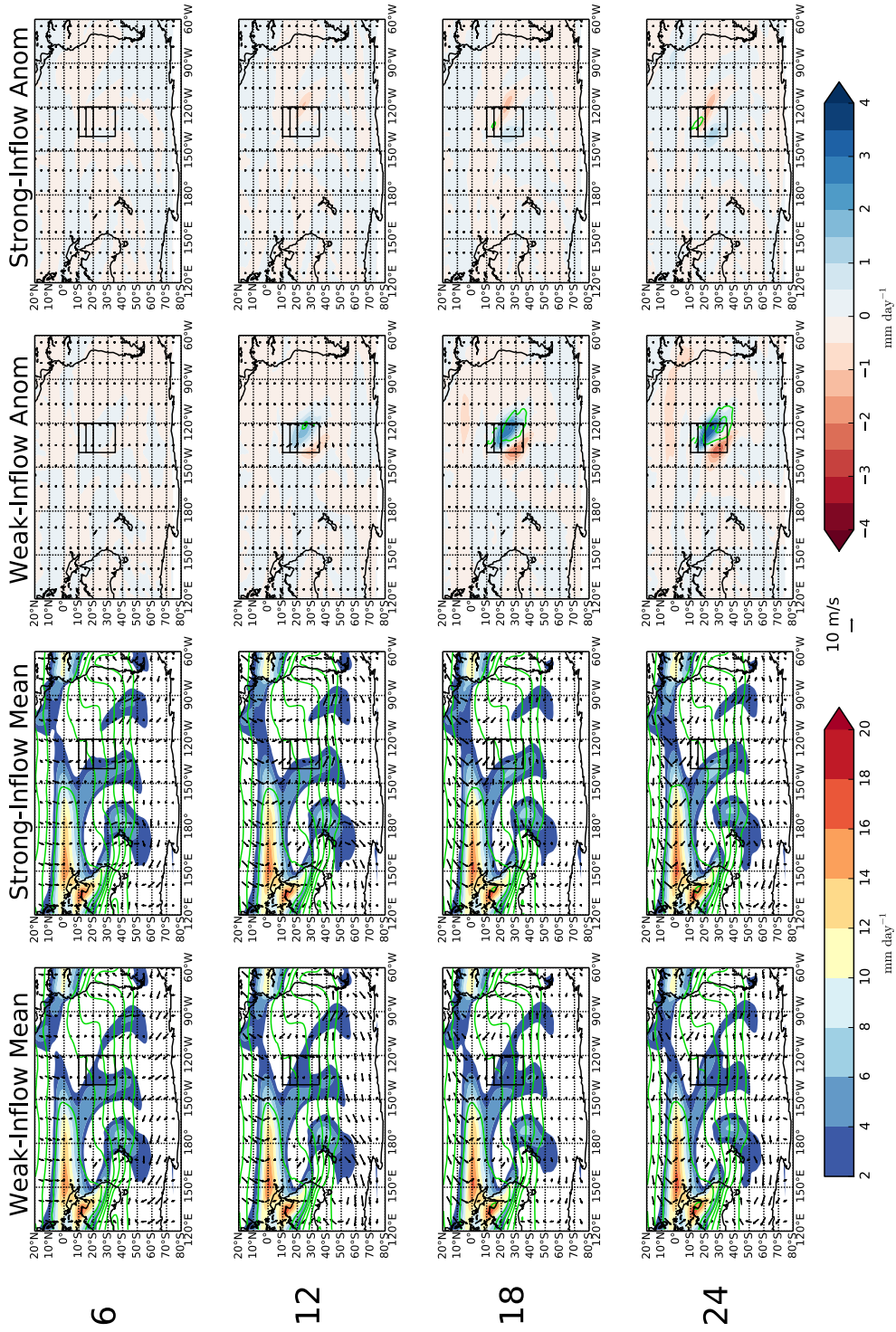


**Figure 4.7.** As Figure 4.5, but showing results from the boundary layer instead of at 850 hPa for both wind and moisture.

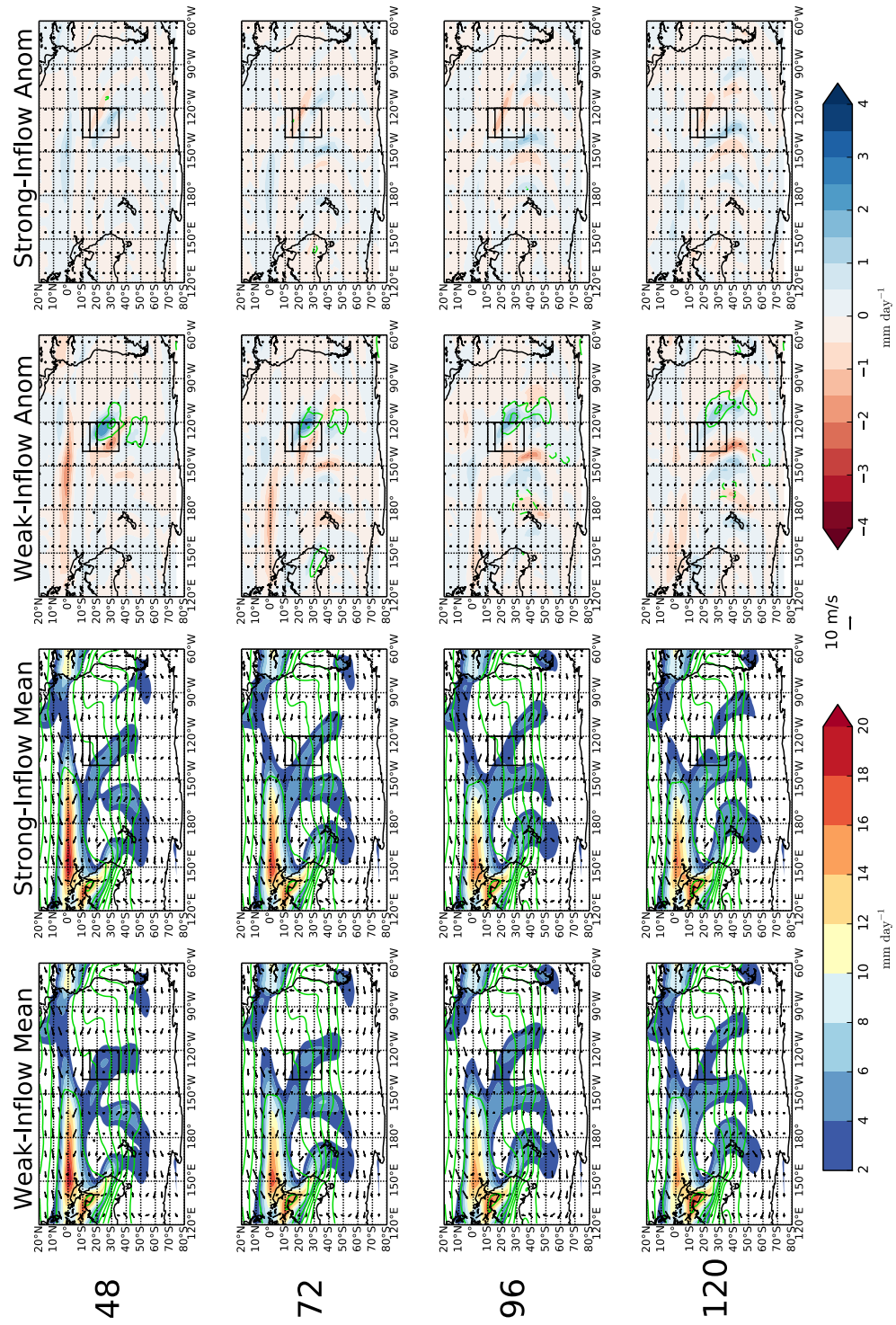


**Figure 4.8.** As Figure 4.6, but showing results from the boundary layer instead of at 850 hPa for both wind and moisture.



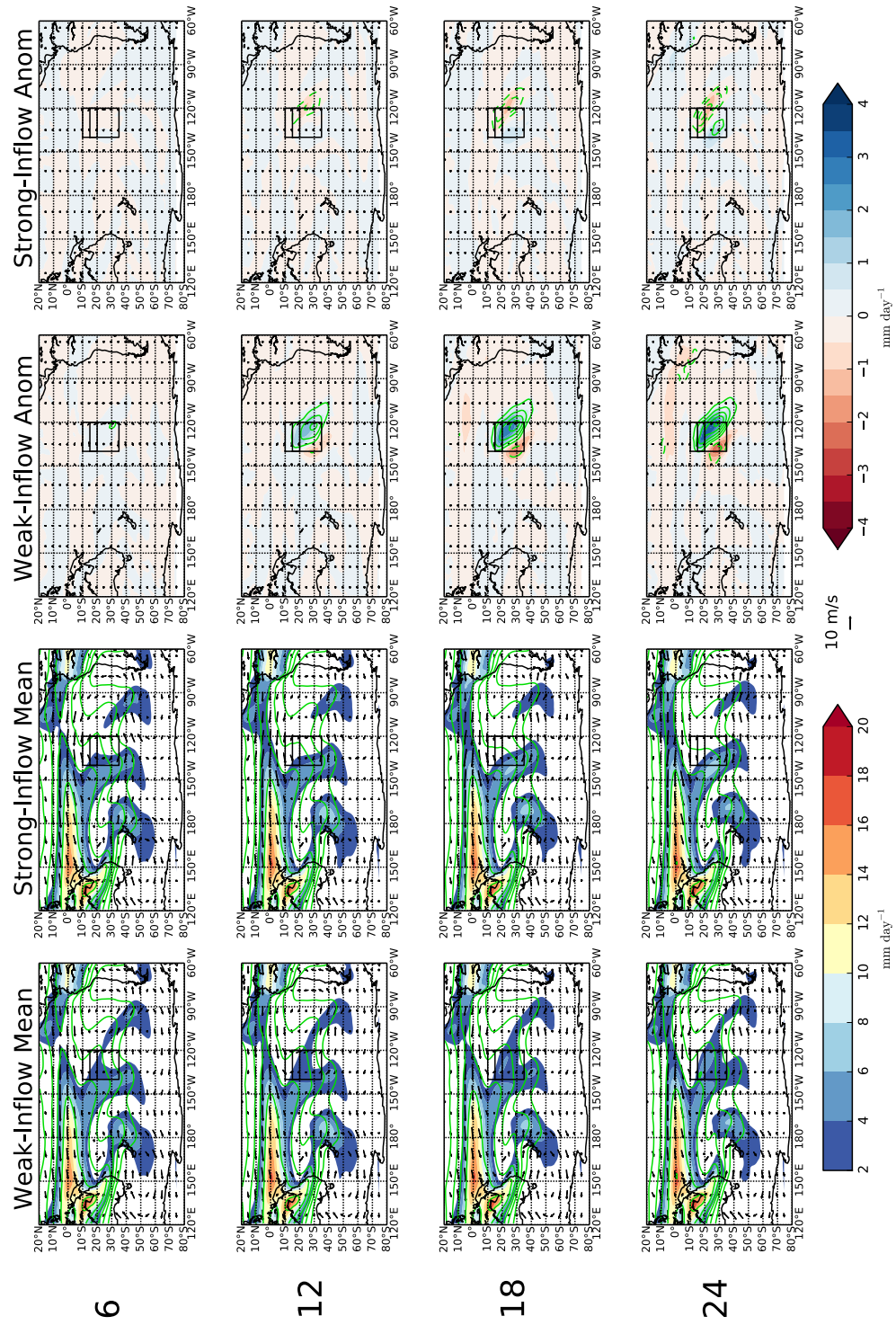


**Figure 4.9.** As Figure 4.5, but showing results from W150/S150 instead of W100/S100.



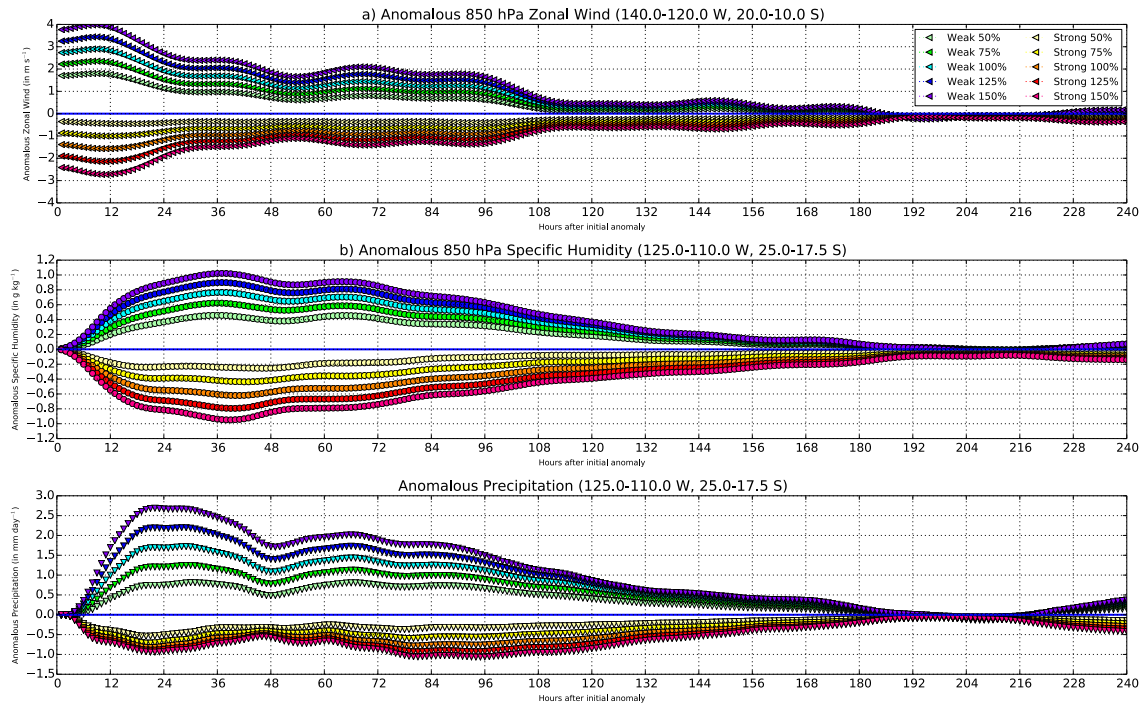


**Figure 4.10.** Anomalous 850 hPa zonal wind (in  $\text{m s}^{-1}$ ), 850 hPa specific humidity (in  $\text{g kg}^{-1}$ ), and precipitation (in  $\text{mm day}^{-1}$ ) averaged in the indicated regions for each of the Wy and Sy experiments throughout the 240 hours following the imposed vorticity anomalies.

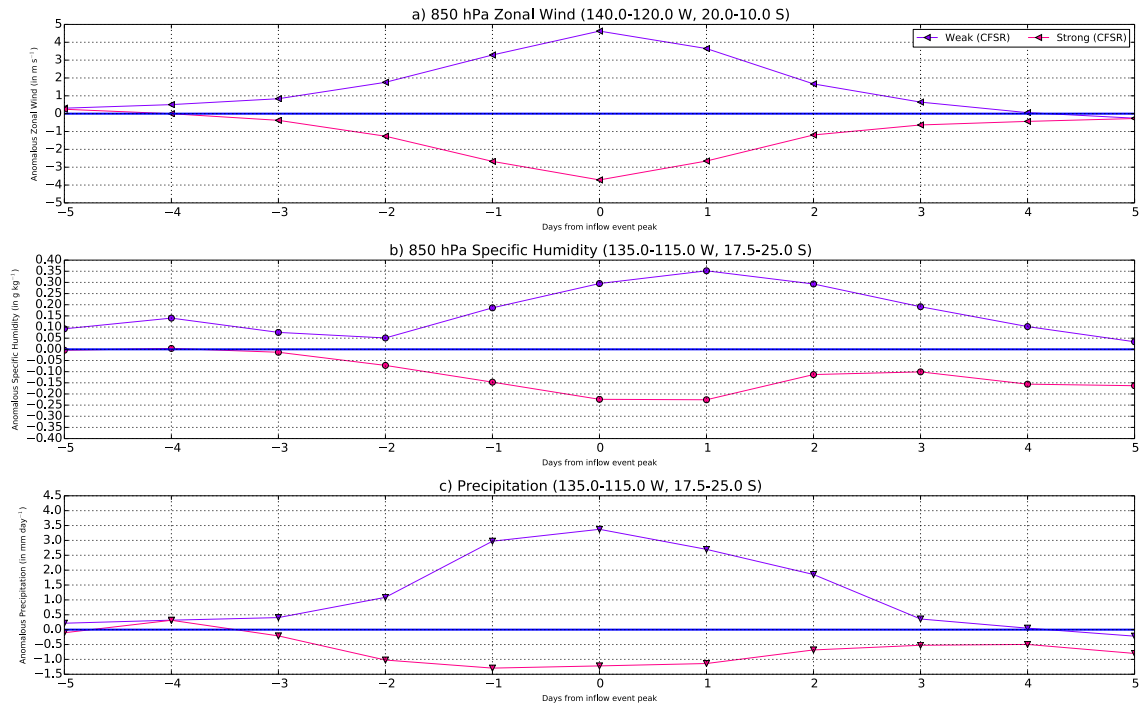


**Figure 4.11.** Anomalous 850 hPa zonal wind (in  $\text{m s}^{-1}$ ), 850 hPa specific humidity (in  $\text{g kg}^{-1}$ ), and precipitation (in  $\text{mm day}^{-1}$ ) averaged in the indicated regions using results from the composite analysis of Niznik and Lintner (2013) throughout their lead-lag analysis (5 days before a weak- or strong-inflow event through 5 days after a weak- or strong-inflow event).

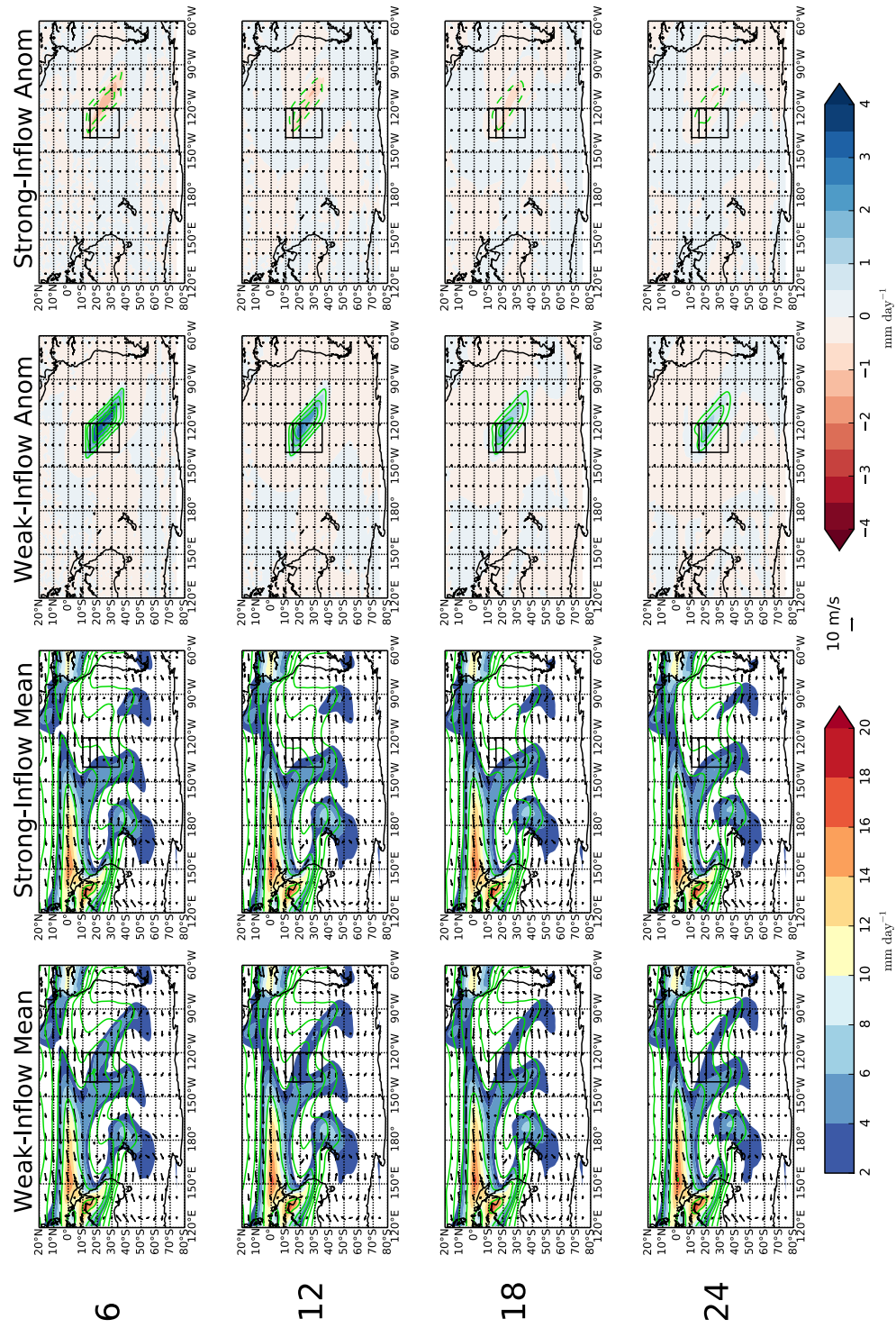


**Figure 4.12.** As Figure 4.5, except using the results of W100Q/S100Q instead of W100/S100.

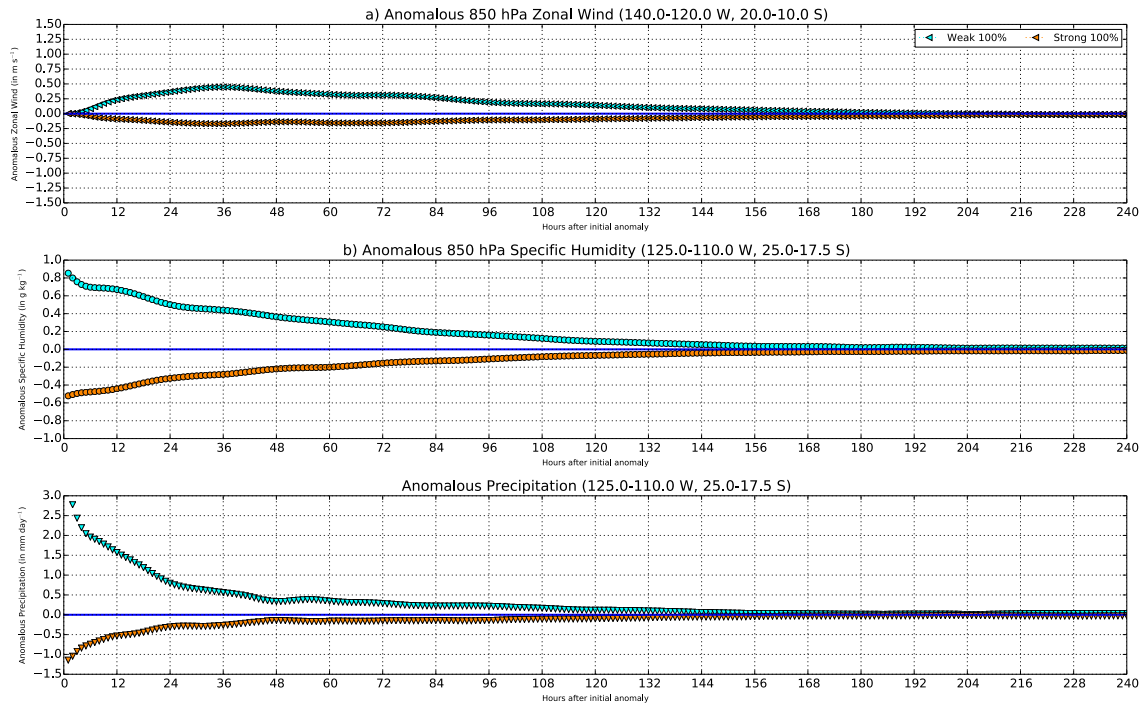


**Figure 4.13.** As Figure 4.10, but showing the results of W100Q/S100Q instead of all Wy/Sy experiments.

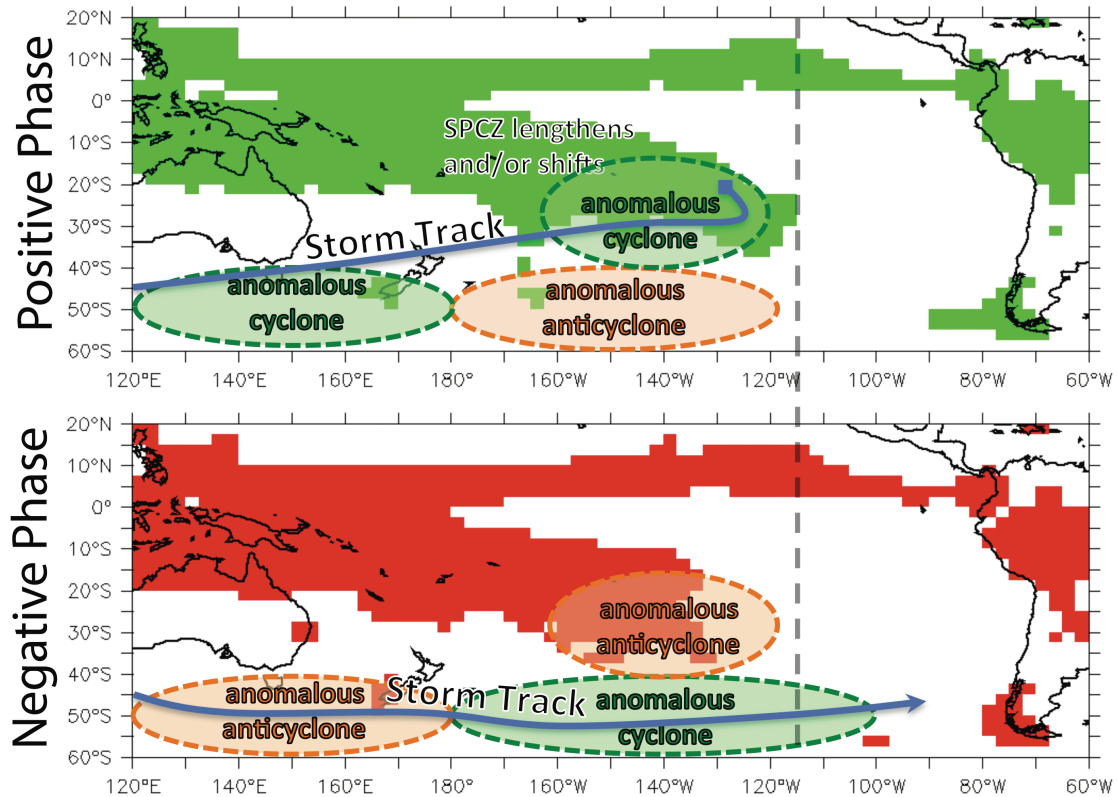


**Figure 5.1.** A schematic showing the key features associated with the weak-inflow (top) and strong-inflow (bottom) phases of the composite index. The weak-inflow phase is characterized by anomalous cyclonic circulation in the southeastern SPCZ and an associated increase in precipitation, anomalous cyclonic circulation south of Australia, and anomalous anticyclonic circulation south of the SPCZ. The strong-inflow phase is characterized by anomalous anticyclonic circulation in the southeastern SPCZ and an associated slight decrease in precipitation, anomalous anticyclonic circulation south of Australia, and anomalous cyclonic circulation south of the SPCZ. There is evidence to suggest that the storm track during the weak-inflow phase is further north than during the strong-inflow phase.

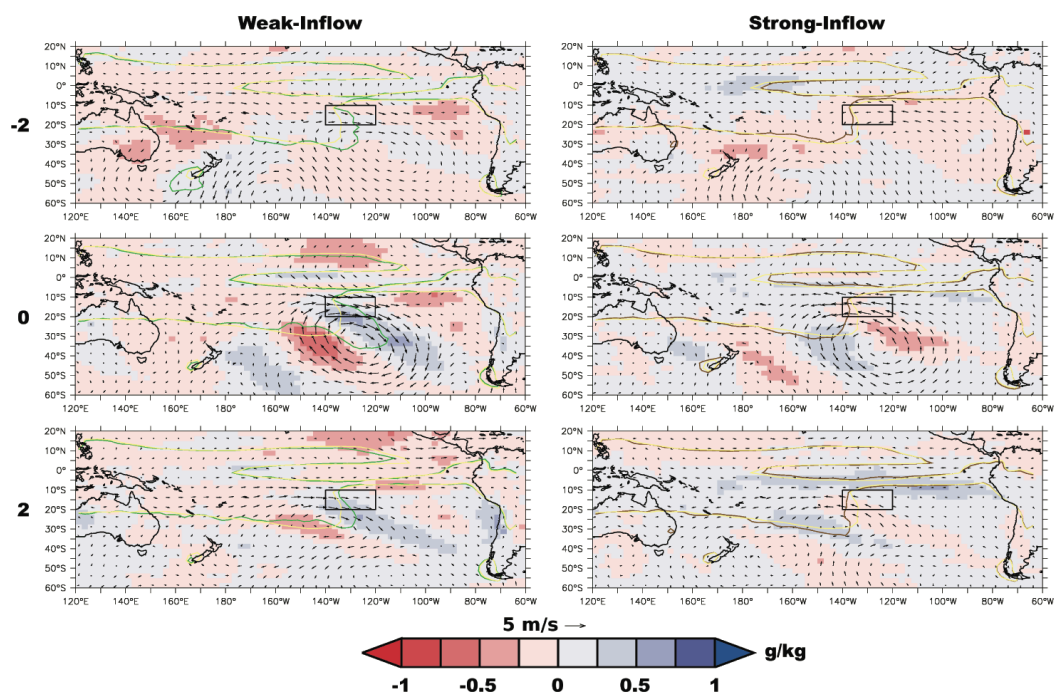


**Figure 5.2.** Same as Figure 2.10, but using data from the RCP8.5 experiment.

## References

- Anderson, B. T., B. R. Lintner, B. Langenbruner, J. D. Neelin, E. Hawkins, and J. Sykus, 2014: Sensitivity of terrestrial precipitation to the structural evolution of sea surface temperature trends. *Geophys. Res. Lett.*, submitted.
- Ashfaq, M., C. B. Skinner, and N. S. Diffenbaugh, 2010: Influence of SST biases on future climate change projections. *Climate Dyn.*, **36**, 1303–1319, doi:10.1007/s00382-010-0875-2.
- Australian Bureau of Meteorology and CSIRO, 2011a: Regional Overview. Vol. 1. *Climate Change in the Pacific: Scientific Assessment and New Research*, BOM–CSIRO, 257 pp.
- , 2011b: Regional Overview. Vol. 2. *Climate Change in the Pacific: Scientific Assessment and New Research*, BOM–CSIRO, 273 pp.
- Bellucci, A., S. Gualdi, and A. Navarra, 2010: The double-ITCZ syndrome in coupled general circulation models: The role of large-scale vertical circulation regimes. *J. Climate*, **23**, 1127–1145.
- Bergeron, T., 1930: Richtlinien einer dynamischen Klimatologie. *Meteor. Z.*, **47**, 246–262.
- Berry, G., M. J. Reeder, and C. Jakob, 2011: A global climatology of atmospheric fronts. *Geophys. Res. Lett.*, **38**, L04809, doi:10.1029/2010GL046451.
- Borlace, S., A. Santoso, W. Cai, and M. Collins, 2014: Extreme swings of the South Pacific Convergence Zone and the different types of El Niño events. *Geophys. Res. Lett.*, doi:10.1002/2014GL060551.
- Brown, J. N., and Coauthors, 2013a: Implications of CMIP3 model biases and uncertainties for climate projections in the western tropical Pacific. *Climatic Change*, **119**, 147–161, doi:10.1007/s10584-012-0603-5.
- Brown, J. R., A. F. Moise, and F. P. Delage, 2011a: Changes in the South Pacific convergence zone in IPCC AR4 future climate projections. *Climate Dyn.*, **39**, 1–19, doi:10.1007/s00382-011-1192-0.
- , S. B. Power, F. P. Delage, R. A. Colman, A. F. Moise, and B. F. Murphy, 2011b: Evaluation of the South Pacific convergence zone in IPCC AR4 climate model simulations of the twentieth century. *J. Climate*, **24**, 1565–1582.
- , A. F. Moise, and R. A. Colman, 2013b: The South Pacific convergence zone in CMIP5 simulations of historical and future climate. *Climate Dyn.*, **41**, 2179–2197, doi:10.1007/s00382-012-1591-x.
- Cai, W., and Coauthors, 2012: More extreme swings of the South Pacific convergence zone due to greenhouse warming. *Nature*, **488**, 365–369, doi:10.1038/nature11358.
- de Szoeke, S. P., and S. P. Xie, 2008: The tropical eastern Pacific seasonal cycle: Assessment of errors and mechanisms in IPCC AR4 coupled ocean–atmosphere general circulation models. *J. Climate*, **21**, 2573–2590.
- DeAngelis, A. M., A. J. Broccoli, and S. G. Decker, 2013: A Comparison of CMIP3 Simulations of Precipitation over North America with Observations: Daily Statistics and Circulation Features Accompanying Extreme Events. *J. Climate*, **26**, 3209–3230, doi: 10.1175/JCLI-D-12-00374.1.



- Folland, C. K., J. A. Renwick, M. J. Salinger, and A. B. Mullan, 2002: Relative influences of the Interdecadal Pacific Oscillation and ENSO on the South Pacific convergence zone. *Geophys. Res. Lett.*, **29**, 1643, doi:10.1029/2001GL014201.
- Ganachaud, A., and Coauthors, 2007: Southwest Pacific Ocean Circulation and Climate Experiment (SPICE)—Part I. Scientific background. International CLIVAR Publ. Series, No. 111, NOAA/OAR Special Rep., NOAA/OAR/PMEL, Seattle, WA, 37 pp.
- , and Coauthors, 2014: The Southwest Pacific Ocean Circulation and Climate Experiment (SPICE). *J. Geophys. Res. Ocean*, **119**, 7660–7686, doi:10.1002/2013JC009678.
- Haffke, C. and G. Magnusdottir, 2013: The South Pacific Convergence Zone in three decades of satellite images. *J. Geophys. Res. Atmos.*, **118**, 10839–1049, doi:10.1002/jgrd.50838.
- Holloway, C. E., and J. D. Neelin, 2009: Moisture vertical structure, column water vapor, and tropical deep convection. *J. Atmos. Sci.*, **66**, 1665–1683.
- Hoskins, B. J., M. E. McIntyre, and A. W. Robertson, 1985: On the use and significance of isentropic potential vorticity. *Quart. J. R. Met. Soc.*, **111**, 877–946.
- , and T. Ambrizzi, 1993: Rossby-wave propagation on a realistic longitudinally varying flow. *J. Atmos. Sci.*, **50**, 1661–1671.
- Hubert, L. F., 1961: A subtropical convergence line of the South Pacific: A case study using meteorological satellite data. *J. Geophys. Res.*, **66**, 797–812.
- Hung, M.-P., J.-L. Lin, W. Wang, D. Kim, T. Shinoda, and S. J. Weaver, 2013: MJO and Convectively Coupled Equatorial Waves Simulated by CMIP5 Climate Models. *Journal of Climate*, **26**, 6185–6214, doi:10.1175/JCLI-D-12-00541.1.
- Kalnay, E., and Coauthors, 1996: The NCEP/NCAR 40-Year Reanalysis Project. *Bull. Amer. Meteor. Soc.*, **77**, 437–471.
- Kiladis, G. N., H. von Storch, and H. van Loon, 1989: Origin of the South Pacific convergence zone. *J. Climate*, **2**, 1185–1195.
- and K. M. Weickmann, 1997: Horizontal structure and seasonality of large-scale circulations associated with submonthly tropical convection. *Mon. Weath. Rev.*, **125**, 1997–2013.
- Kummerow, C., and Coauthors, 2000: The status of the Tropical Rainfall Measuring Mission (TRMM) after two years in orbit. *J. Appl. Meteor.*, **39**, 1965–1982.
- Liebmann, B. and C. A. Smith, 1996: Description of a complete (interpolated) OLR dataset. *Bull. Amer. Meteor. Soc.*, **77**, 1275–1277.
- Li, J.-L. F., W.-L. Lee, D. E. Waliser, J. D. Neelin, J. P. Stachnik, and T. Lee, 2014: Cloud-precipitation-radiation-dynamics interaction in global climate models: A snow and radiation interaction sensitivity experiment. *J. Geophys. Res. Atmos.*, **119**, 3809–3824, doi: 10.1002/2013JD021038.
- Lin, J.-L., and Coauthors, 2006: Tropical intraseasonal variability in 14 IPCC AR4 climate models. Part I: Convective signals. *J. Climate*, **19**, 2665–2690, doi:10.1175/JCLI3735.1.
- , 2007: The double-ITCZ problem in IPCC AR4 coupled GCMs: Ocean–atmosphere feedback analysis. *J. Climate*, **20**, 4497–4525.
- Linsley, B. K., P. Zhang, A. Kaplan, S. S. Howe, and G. M. Wellington, 2008: Interdecadal–decadal climate variability from multi- coral oxygen isotope records

- in the South Pacific convergence zone region since 1650 A.D. *Paleoceanography*, **23**, PA2219, doi:10.1029/2007PA001539.
- Lintner, B. R., and J. D. Neelin, 2008: Eastern margin variability of the South Pacific convergence zone. *Geophys. Res. Lett.*, **35**, L16701, doi:10.1029/2008GL034298.
- , C. E. Holloway, and J. D. Neelin, 2011: Column water vapor statistics and their relationship to deep convection, vertical and horizontal circulation, and moisture structure at Nauru. *J. Climate*, **24**, 5454–5466.
- , G. Bellon, A. H. Sobel, D. Kim, and J. D. Neelin, 2012: Implementation of the Quasi-equilibrium Tropical Circulation Model 2 (QTCM2): Global simulations and convection sensitivity to free tropospheric moisture. *J. Adv. Model. Earth Syst.*, **4**, M12002, doi: 10.1029/2012MS000174.
- Mantsis, D. F., B. R. Lintner, A. J. Broccoli, and M. Khodri, 2013: Mechanisms of mid-Holocene precipitation change in the South Pacific convergence zone. *J. Climate*, **26**, 6937–6953.
- Matthews, A. J., B. J. Hoskins, J. M. Slingo, and M. Blackburn, 1996: Development of convection along the SPCZ within a Madden-Julian oscillation. *Q. J. Roy. Meteor. Soc.*, **122**, 669–688.
- , and G. N. Kiladis, 1999a: The tropical-extratropical interaction between high-frequency transients and the Madden-Julian Oscillation. *Mon. Wea. Rev.*, **127**: 661–677.
- , and G. N. Kiladis, 1999b: Interactions between ENSO, transient circulation and tropical convection over the Pacific. *J. Climate*, **12**, 3062–3086.
- , 2012: A multiscale framework for the origin and variability of the South Pacific convergence zone. *Quart. J. Roy. Meteor. Soc.*, **138**, 1165–1178, doi:10.1002/qj.1870.
- Meehl, G. A., 1987: The annual cycle and interannual variability in the tropical Pacific and Indian Ocean regions. *Mon. Wea. Rev.*, **101**, 486–495.
- , C. Covey, T. Delworth, M. Latif, B. McAvaney, J. F. B. Mitchell, R. J. Stouffer, and K. E. Taylor, 2007: The WCRP CMIP3 multimodel dataset: A new era in climate change re- search. *Bull. Amer. Meteor. Soc.*, **88**, 1383–1394.
- Murphy, B. F., S. B. Power, and S. McGree, 2014: The Varied Impacts of El Niño–Southern Oscillation on Pacific Island Climates. *J. Climate*, **27**, 4015–4036.
- Nakamura, H., and A. Shimpo, 2004: Seasonal variations in the Southern Hemisphere storm tracks and jet streams as revealed in a reanalysis dataset. *J. Climate*, **17**, 1828–1844.
- Niznik, M. J. and B. R. Lintner, 2013: Circulation, Moisture, and Precipitation Relationships along the South Pacific Convergence Zone in Reanalyses and CMIP5 Models. *J. Climate*, **26**, 10174–10192, doi:10.1175/JCLI-D-13-00263.1.
- , B. R. Lintner, A. J. Matthews, and M. J. Widlansky, 2015: The Role of Tropical-Extratropical Interaction and Synoptic Variability in Maintaining the South Pacific Convergence Zone in CMIP5 Models. *J. Climate*, in press.
- Power, S., 2011: Understanding the South Pacific convergence zone and its impacts: International Workshop on the South Pacific Convergence Zone, Apia, Samoa, 24–26 August 2010. *Eos, Trans. Amer. Geophys. Union*, **92**, 55–56.

- Reynolds, R. W., T. M. Smith, C. Liu, D. B. Chelton, K. S. Casey, and M. G. Schlax, 2007: Daily high-resolution blended analyses for sea surface temperature. *J. Climate*, **7**, 929–948.
- Robertson, A. W., and C. R. Mechoso, 2000: Interannual and interdecadal variability of the South Atlantic convergence zone. *Mon. Wea. Rev.*, **128**, 2947–2957.
- Saha, S., and Coauthors, 2010: The NCEP Climate Forecast System Reanalysis. *Bull. Amer. Meteor. Soc.*, **91**, 1015–1057.
- Sillmann, J., V. V. Kharin, F. W. Zwiers, X. Zhang, and D. Bronaugh, 2013a: Climate extreme indices in the CMIP5 multimodel ensemble: Part 1. Model evaluation in the present climate. *J. Geophys. Res. Atmos.*, **118**, 1716–1733.
- Slingo, J.M., and CoAuthors, 1996: Intraseasonal oscillations in 15 atmospheric general circulation models: results from an AMIP diagnostic subproject. *Climate Dyn.*, **12**, 325–358.
- Streten, N. A., 1973: Some characteristics of satellite-observed bands of persistent cloudiness over the Southern Hemisphere. *Mon. Wea. Rev.*, **101**, 486–495.
- Takahashi, K., and D. S. Battisti, 2007: Processes controlling the mean tropical Pacific precipitation pattern. Part II: The SPCZ and the southeast Pacific dry zone. *J. Climate*, **20**, 5696–5706.
- Taylor, K. E., R. J. Stouffer, and G. A. Meehl, 2012: An overview of CMIP5 and the experiment design. *Bull. Amer. Meteor. Soc.*, **93**, 485–498.
- Trenberth, K. E., 1976: Spatial and temporal variations of the Southern Oscillation. *Quart. J. Roy. Meteor. Soc.*, **102**, 639–653.
- , 1991: Storm Tracks in the Southern Hemisphere. *J. Atmos. Sci.*, **48**, 2159–2178.
- van der Waal, K., A. J. Matthews, D. P. Stevens, and M. M. Joshi, 2015: A dynamical framework for the origin of the South Pacific and South Atlantic Convergence Zones. *Q. J. Roy. Meteor. Soc.*, in press, doi: 10.1002/qj.2508.
- Vannière, B., E. Guilyardi, T. Toniazzo, G. Madec, and S. Woolnough, 2014: A systematic approach to identify the sources of tropical SST errors in coupled models using the adjustment of initialized experiments. *Climate Dyn.*, in press, doi:10.1007/s00382-014-2051-6.
- Vecchi, G. A., and B. J. Soden, 2007: Global warming and the weakening of the tropical circulation. *J. Climate*, **20**, 4316–4340.
- Vincent, D. G., 1994: The South Pacific convergence zone (SPCZ): A review. *Mon. Wea. Rev.*, **122**, 1949–1970.
- Vincent, E. M., M. Lengaigne, C. E. Menkes, N. C. Jourdain, P. Marchesiello, and G. Madec, 2011: Interannual variability of the South Pacific convergence zone and implications for tropical cyclone genesis. *Climate Dyn.*, **36**, 1881–1896, doi:10.1007/s00382-009-0716-3.
- Wang, B. and H. Rui, 1990: Synoptic climatology of transient tropical intraseasonal convection anomalies: 1975–1985. *Meteor. Atmos. Phys.*, **44**, 43–61.
- Webster, P. J., and J. R. Holton, 1982: Cross-equatorial response to middle-latitude forcing in a zonally varying basic state. *J. Atmos. Sci.*, **39**, 722–733.
- and H.-R. Chang, 1997: Atmospheric wave propagation in heterogeneous flow: basic controls on tropical-extratropical interaction and equatorial wave modification. *Dyn. Atmos. Oceans*, **27**, 91–134.

- Widlansky, M. J., P. J. Webster, and C. D. Hoyos, 2011: On the location and orientation of the South Pacific convergence zone. *Climate Dyn.*, **36**, 561–578, doi:10.1007/s00382-010-0871-6.
- , A. Timmermann, K. Stein, S. McGregor, N. Schneider, M. H. England, M. Lengaigne, and W. Cai, 2013: Changes in South Pacific rainfall bands in a warming climate. *Nat. Climate Change*, **3**, 417–423, doi:10.1038/NCLIMATE1726.
- , A. Timmermann, S. McGregor, M. F. Stuecker, and W. Cai, 2014: An Interhemispheric Tropical Sea Level Seesaw due to El Niño Taimasa. *J. Climate*, **27**, 1070–1081.
- Xie, P. and P. A. Arkin, 1997: Global precipitation: A 17-year monthly analysis based on gauge observations, satellite estimates, and numerical model outputs. *Bull. Amer. Meteor. Soc.*, **78**, 2539–2558.
- Zhang, C., 2001: Double ITCZs. *J. Geophys. Res.*, **106**, 11785–11792.